

NORTHWESTERN UNIVERSITY

Synchrotron X-ray Studies of
Epitaxial 2D Material Interfaces

A DISSERTATION

SUBMITTED TO THE GRADUATE SCHOOL
IN PARTIAL FULFILLMENT OF THE REQUIREMENTS

for the degree

DOCTOR OF PHILOSOPHY

Field of Materials Science and Engineering

By

Gavin Paul Campbell

EVANSTON, ILLINOIS

May 2018

© Copyright by Gavin Paul Campbell 2018
All Rights Reserved

Abstract

Sparked by the isolation of graphene in 2004, the research community has developed a family of 2D materials with distinct functionalities, enabling rapid demonstrations of entirely 2D devices with applications in energy, electronics, sensors and medicine. The desire to capitalize on the fantastic properties of 2D materials motivates ongoing efforts to synthesize high-quality 2D materials on large-scales. Epitaxial deposition of 2D materials on single-crystal substrates yields large-scale production of 2D materials without compromising crystal quality. However, 2D material properties are altered depending on the strength of the interactions with the substrate. The strength of these interactions, from weak van der Waals attractions to strong covalent bonds, are further revealed by local perturbations to the vertical atomic structure of the interface. For my dissertation research, I have employed high-resolution synchrotron X-ray characterization techniques to probe the interface between 2D materials and their growth substrate with atomic precision on wafer-scales. My dissertation primarily focuses on the interface of elemental 2D materials and single-crystal substrates, specifically 2D boron (borophene) on Ag(111) and graphene on Ge(110). The primary objective of these measurements is to resolve outstanding questions about the strength of interactions and resulting structure of these interfaces. Specifically, employing X-ray standing wave-enhanced photoelectron spectroscopy, I reveal borophene to be a highly planar atomic layer of B atoms by constructing a chemically-resolved vertical structure of borophene with sub-Å precision. Next, I show that epitaxial graphene (EG) atop Ge(110), upon annealing in ultra-high vacuum (UHV), induces a novel reconstruction of the underlying Ge(110) surface. I perform a detailed documentation of this structure using a combination of high-resolution X-ray reflectivity and grazing-incident X-ray diffraction. Finally, I probe the registry of

van der Waals epitaxial materials using a combination of grazing-incident X-ray scattering measurements. Overall, the work presented herein reveals how distinct X-ray surface science techniques can be employed to resolve outstanding questions about new 2D material interfaces.

Acknowledgements

First, I would like to thank my advisor, Prof. Michael Bedzyk, for his fantastic support and flexibility throughout my time at Northwestern. Mike has an exceptional enthusiasm towards and mastery of X-ray physics, I am privileged for his mentorship. I want to also thank my committee members for their time and expertise; Dr. Sang-Soo Lee sharing his X-ray knowledge and Profs. Lincoln Lauhon and Mark Hersam for their collaboration and leadership within the MRSEC and valuable insights over the years.

I am grateful to my many collaborators for their contributions and support, without whom this work would not have been possible. I would like to thank Jade Balla, Xiaolong Lu, Haddalia Bergeron, Brian Kiraly, and Andrew Mannix for providing samples and challenging me to think more deeply. Each of them their work is represented in this dissertation. I extend special thanks to Andrew Mannix for bringing borophene to the United Kingdom. I would also like to thank Robert Jacobberger and Prof. Michael Arnold for providing samples and my coworkers in the MRSEC Leadership council for providing feedback.

My colleagues in the Bedzyk group have supported me throughout my time here. Early on, I benefited from the UHV and X-ray knowledge of Martin McBriarty and Sven Stolz. From the beginning, Jon Emery provided a foundation for me to build upon and has provided continuous support throughout my time and Sumit Kewalramani has been an excellent mentor throughout the years. My contemporaries in the Bedzyk group: Boris Harutyunyan, Xiao Chen, Liane Moreau, Changrui Gao, and Kurinji Krishnamoorthy have been a constant source of support and friendship, further enriched by Katherine Harmon, for insights into interface science; Stephanie Moffitt, for her writing expertise; Bor-Rong Chen, for getting me started in the X-ray lab; and Li Zeng for our

meaningful conversations during beamtime. I am also grateful for my interactions with Guennadi Evmenenko, Achari Kondapalli, Bo-Hong Liu, Jeffery Chen, Elise Goldfine, Anusheela Das, Curtis Leung, I-Cheng Tung, Janak Thapa, Bruce Buchholz, and Jerry Carsello.

I have also greatly benefited from facilities and staff support at Argonne National Lab and Diamond National Lab. Several beamline staff members were instrumental in this work, Zhan Zhang and Christian Schlepütz of Sector 33 and Joe Strzalka of Sector 8. Special thanks go to the staffs of Sector 5 and I09, specifically Denis Keane of Sector 5 and Tien-Lin Lee of I09, who both showed extraordinary commitment to the success of the users at their beamlines. Lastly, I thank Jörg Zegenhagen for his guidance and Paul Fenter and his group for teaching me the fundamentals of X-ray data analysis.

Of course, I would like to acknowledge my family and friends for their support. I am grateful to my parents, Scot and Melanie, for nurturing my curiosity and providing an academically enriching environment. I am thankful to my brothers, Eric and Colin, and my sister, Caitlin, for all their support and for our adventures through Europe. I am grateful to Alex, Ross, and Bradley for their enduring friendship. Finally, I would like to thank Kathleen for her phenomenal support and enduring companionship.

I also acknowledge the financial support I received from the Northwestern Materials Science and Engineering Center and the National Science Foundation, particularly for supporting my many trips to Argonne and international trip to Diamond.

For Kathleen,
looking forward

List of Abbreviations

2D	Two Dimensional
AFM	Atomic Force Microscopy
BP	Black Phosphorus
CCD	Charge-Coupled Device
CTR	Crystal Truncation Rod
CVD	Chemical Vapor Deposition
DFT	Density Functional Theory
EAL	Effective Attenuation Length
EBE	E-Beam Evaporator
EG	Epitaxial Graphene
FCC	Face-Centered Cubic
FWHM	Full-Width Half-Maximum
GISAXS	Grazing incidence Small-Angle X-ray Scattering
GIWAXS	Grazing incidence Wide-Angle X-ray Scattering
GIXD	Grazing incidence X-ray Diffraction
GIXS	Grazing Incidence X-ray Scattering
hBN	hexagonal Boron Nitride
IMFP	Inelastic Mean Free Path
LEED	Low-Energy Electron Diffraction
MBE	Molecular Beam Evaporator
MMS	Metalized Molecular Stripes
NIXSW	Normal Incidence X-ray Standing Wave
OPA	Octadecylphosphonic Acid
PVD	Physical Vapor Deposition
QCM	Quartz Crystal Monitor
SAM	Self-Assembled Monolayer
SE2DM	Synthetic Elemental 2D Material

STM	Scanning Tunneling Microscopy
STS	Scanning Tunneling Spectroscopy
TMD	Transition Metal Dichalcogenide
TMFP	Transport Mean Free Path
UHV	Ultra-High Vacuum
vdW	van der Waals
XPS	X-ray Photoelectron Spectroscopy
XRF	X-ray Fluorescence
XRR	X-ray Reflectivity
XSW	X-ray Standing Wave

Table of Contents

Abstract.....	3
Acknowledgements.....	5
List of Abbreviations	8
Table of Contents	10
List of Figures	12
List of Tables	14
Chapter 1: Overview	15
1.1: Motivation: Material Interfaces in 2D.....	15
1.1: Outline.....	16
Chapter 2: Fundamentals of two dimensional materials.....	20
2.1: Materials Stable in Two Dimensions	20
2.2: 2D material synthesis	22
2.3: Properties of Graphene.....	24
2.4: Properties Elemental 2D Materials	26
Chapter 3: Structure of 2D Materials on Substrates	29
3.1: Interactions at interfaces	29
3.2: Epitaxial Graphene on Single-Crystals	30
3.3: Epitaxial Borophene.....	37
3.4: vdW Epitaxy.....	40
Chapter 4: X-ray Characterization Techniques.....	41
4.1: Introduction to X-ray physics.....	41
4.2: X-ray standing wave	51
4.3: Crystal Truncation Rod.....	57
4.4: Grazing incidence X-ray diffraction	60
4.5: X-ray Photoelectron Spectroscopy.....	63
4.6: Other Spectroscopy	67
Chapter 5: B/Ag(111) Interface	69
5.1: Abstract	69

	11
5.2: Introduction	69
5.3: Methods.....	72
5.4: Synthesis	76
5.5: Results	82
5.6: Conclusions	96
Chapter 6: EG/Ge(110) Reconstruction.....	97
6.1: Introduction	97
6.2: Methods.....	99
6.3: Results	102
6.4: Conclusions	111
Chapter 7: EG/SiC(0001) Heterostructures	112
7.1: Introduction	112
7.2: Methods.....	113
7.4: Results	116
7.5: Conclusions	130
Chapter 8: Future Work	131
8.1: Borophene on Au(111).....	131
8.2: Blue Phosphorus.....	131
References:.....	133
Appendix A: Ag(111) XPS-XSW.....	147
A.1: Type equation here.Oddities in Photoelectron Yields.....	147
Appendix B: Data sets	151
B.1: GIXD Data for “6×2” EG/Ge(110)	151

List of Figures

Figure 2.1: The crystal structure of graphene, defined by lattice vectors a_{EG} and b_{EG} .	24
Figure 2.2: Schematic of graphene	25
Figure 2.3: Predicted 2D phosphorus crystal structures	27
Figure 3.1: C 1s photoelectron spectra of graphene	34
Figure 3.2: The vertical electron density profile of EG on SiC(0001)	36
Figure 3.3: Borophene lattice and atomic structures	38
Figure 3.4: Proposed atomic models for borophene on Ag(111)	40
Figure 4.1: Simulated X-ray standing wave measurement of borophene	56
Figure 4.2: Schematic of crystal truncation rod	59
Figure 4.3: GIXS geometric setup	63
Figure 5.1: Borophene synthesis and atomic structures	71
Figure 5.2: Diagram of the I09 beamline at Diamond. Experimental was performed in the EH2 end-station using hard and soft X-rays from separate undulators. (From Ref. [169])	72
Figure 5.2: Fermi edge measurements	75
Figure 5.3: Reciprocal space analysis of in-plane borophene atomic structure	78
Figure 5.4: LEED patterns of 300 °C Borophene	81
Figure 5.5: High-resolution XPS of borophene	82
Figure 5.6: XPS survey, C 1s, and O 1s spectra of borophene	84
Figure 5.7: XPS of 20 °C deposited multilayer boron	85
Figure 5.8: Angular-resolved boron 1s XPS	86
Figure 5.9: XSW characterization of silver	88
Figure 5.10: XSW characterization of 20 °C deposited multilayer boron	89
Figure 5.11: XSW characterization of the borophene	90
Figure 5.12: XSW characterization of the in-plane borophene	92
Figure 5.13: In-plane atomic model structure	94
Figure 6.1: STM images of graphene on Ge(110)	98
Figure 6.2: STM data of annealed EG/Ge(110)	102
Figure 6.3: Spectra of as-grown and annealed EG/Ge(110) samples	103

Figure 6.4: XRR data of EG/Ge(111).....	105
Figure 6.5: Lattice of annealed EG/Ge(110).....	107
Figure 6.6: GIXD surface characterization of EG/Ge(110).....	109
Figure 7.1: CVD-grown MoS ₂ on EG.....	117
Figure 7.2: Rotationally commensurate van der Waals epitaxy of MoS ₂ on EG	119
Figure 7.3: Examination of the growth orientation of MoS ₂	120
Figure 7.4: XRR data	122
Figure 7.5: GIWAXS measurements	125
Figure 7.6: AFM of degraded MoS ₂ flakes on EG/SiC	127
Figure 7.7: AFM of MMS.....	127
Figure 7.8: Grazing incidence small and wide-angle X-ray scattering.....	130
Figure A.1: Flowchart describing the procedure to collect and analyze data at I09.....	147
Figure A.2: X-ray standing wave (XSW) characterization of silver	149
Figure A.3: X-ray photoelectron spectroscopy fitting parameters of Ag 3d spectra during X-ray standing wave characterization.....	150

List of Tables

Table 3.1: The closest separation in EG/M.....	31
Table 5.1: Energies and angles to access Ag Bragg conditions.....	74
Table 5.2: QCM measured B deposition rate.....	79
Table 5.3: XPS fitting parameters for Soft and Hard B 1s X-ray spectra.....	83
Table 5.4: XPS fitting parameters for Soft and Hard Ag 3d X-ray spectra.....	85
Table 5.5: For the two deposition temperatures, XPS determined boron percent	87
Table 5.6: Coherent fraction (f^H) and coherent Position (P^H) of B.....	93
Table 6.1: Results of model dependent fit to XRR data	104
Table A.1: Coherent fractions ($f_{300^\circ\text{C}}$), maximum normalized yields (Y_{max}), and corresponding maximum intensity (I_{max}) of Ag 3d _{5/2} photoelectron yields.....	148
Table B.1: Measured <i>Fhsks2</i> for Ge(110) “6×2” reconstruction.....	151

Chapter 1: Overview

1.1: Motivation: Material Interfaces in 2D

The successful isolation and characterization of graphene in 2004, revealed new materials physics (e.g. relativistic charge carriers [1]) and launched the now densely populated field of two-dimensional (2D) materials. The arena of 2D materials now includes elemental and compound planar and buckled structures, with an equally diverse set of electronic, mechanical, and optical properties. The onset of these new materials properties follows the vertical confinement of electrons, owing to the isolation of individual atomic layers, which are typically derived from weakly van der Waals (vdW) bonded sheets of a hexagonal bulk crystal (e.g. graphene from graphite). With range of exceptional electronic properties now accessible at the 2D limit, the desire to utilize these materials in large scale device applications has motivated the development of scalable growth methods of single-crystal high-quality 2D materials on technologically relevant substrates. Though the in-plane structure of these materials is robust, 2D materials nonetheless interact with their local environment, thereby imparting 2D materials with functions beyond their intrinsic properties [2,3]. Interestingly these interactions are, in some cases, strong enough to stabilize novel 2D structures, offering a means to dramatically expand the scope of 2D materials beyond those derived from bulk crystals [4]. This has driven the development of so-called synthetic 2D materials [e.g. 2D boron (borophene) [5,6] and 2D silicon (silicene) [7]] which lack direct bulk analogs.

The formation of these new 2D structures at single-crystal interfaces present a myriad of characterization challenges, owing to degeneracy in plausible planar-like surface structures. This problem is ubiquitous in the field of 2D materials owing to ambiguity in distinguishing free-

standing 2D materials from surface alloys [8,9], subsurface precipitates [10], or interfacial reconstructions, particularly when investigating systems where the atomic structure of the surface and interface are both unknown. Distinguishing a 2D material from other surface features is of paramount importance when interpreting materials characteristics, as the salient properties of the system can depend heavily on their position relative to the supporting substrate. Even for a vdW bonded 2D material, the interface structure influences strain, doping, and symmetry of the 2D overlayer [11-13]. Thus, understanding the interface between a 2D material and single-crystal substrate necessitates the use of chemically sensitive structural characterization with sub-Å resolution [14]. This challenge bodes well for study through X-ray interface science, in particular by using X-ray spectroscopy to impart chemical specificity to Ångström-resolution X-ray diffraction measurements. This dissertation demonstrates the use of synchrotron-based X-ray tools, primarily X-ray standing wave (XSW), crystal truncation rod (CTR), and grazing incidence X-ray diffraction (GIXD), to solve the physics and chemistry of new surface structures, with an emphasis on determining the interface structure of 2D structures on a given substrate.

1.1: Outline

In this document, I explore the structure of interfaces between epitaxial 2D materials and their substrate. My work primarily focuses on elemental 2D materials, therefore in chapter 2, I describe the origin of the characteristic properties of these materials and how a common set of bonding configurations which lead to a diverse array of elemental 2D structures. I focus on graphene and black phosphorus as prototypical elemental 2D materials with a planar and buckled bonding configuration, respective. I discuss how these structures inform our understanding of new 2D materials which lack corresponding bulk allotropes.

The discussion of 2D materials is further expanding upon in chapter 3 by introducing interactions of epitaxial 2D materials with their growth substrate. I review graphene on metal substrates to demonstrate how the C-Metal interaction strength generates perturbations in the vertical structure of the overlaying graphene accompanied by changes to the electronic properties of graphene. I describe how rigidly bound covalent substrates, such as graphene on Ge and graphene on SiC, circumvent these interactions to yield pristine monolayer graphene. Finally, I introduce van der Waals epitaxy which has the potential to yield high-quality graphene with minimal substrate interactions.

In chapter 4, I establish the principles of X-ray interface science techniques which I used in my dissertation research to deduce the vertical structure of 2D materials and their interface. Initially, I introduce the kinematic and dynamic theory of X-rays interaction with matter, which I then expand upon to the theory of X-ray standing wave-enhanced photoelectron spectroscopy (XSW-XPS), crystal truncation rod (CTR), and grazing-incidence X-ray diffraction (GIXD).

Chapter 5 describes my collaborative efforts with Andrew Mannix to resolve the interface structure of two distinct phases of borophene on Ag(111). Using XSW-XPS, we resolve the positions of boron in multiple chemical states with sub-Ångström spatial resolution, revealing that the borophene forms a single planar layer that is 2.4 Å above the unreconstructed Ag surface. Moreover, our results reveal that multiple borophene phases exhibit these characteristics, denoting a unique form of polymorphism consistent with recent predictions.

In chapter 6, I probe the interface between epitaxial graphene and Ge(110) employing scanning tunneling microscopy (STM), GIXD, and high-resolution X-ray reflectivity (XRR) experiments. We present a thorough study of epitaxial graphene (EG)/Ge(110) and report a

Ge(110) “6×2” reconstruction stabilized by the presence of epitaxial graphene unseen in group-IV semiconductor surfaces. Our X-ray studies reveal that graphene resides atop the surface reconstruction with a 0.34 nm van der Waals (vdW) gap and provides protection from ambient degradation.

In chapter 7, I explore the interface and in-plane structure of multi-dimensional vdW epitaxy on EG on SiC(0001). First, we examine here the thickness-controlled vdW epitaxial growth of MoS₂ on EG *via* chemical vapor deposition, which gives rise to transfer-free synthesis of a 2D heterostructure with registry between its constituent materials. The rotational commensurability observed between the MoS₂ and EG is driven by the energetically favorable alignment of their respective lattices and results in nearly strain-free MoS₂, as evidenced by synchrotron X-ray scattering. We proceed to investigate the structure of metal deposited on octadecylphosphonic acid (OPA), which forms a 1D heterostructure in registry with the underlying graphene. We examine the orientational registry and long-range structure of the OPA molecules using GIXD techniques and confirm the molecules are well align and could act as a catalytic template for further chemistry.

Finally, in chapter 8, I review 2D materials systems reported in the literature that bode well for study using X-ray interface techniques. I discuss theoretical results of borophene polymorphs grown on Au(111), which are predicated to have a distinct vertical and in-plane structure from borophene atop Ag(111) owing to weaker interactions with the substrate. I also discuss a recent report of 2D blue phosphorus stabilized by Au(111), which appears to deviate in structure from theoretical predications and bulk measurements.

Appendices are included to supplement discussion in the main chapters. Appendix A describes unresolved sources of error seen in the XPS analyser at I09. Appendix B includes a complete dataset for the GIXD analysis performed in chapter 6.

Chapter 2: Fundamentals of two dimensional materials

2D materials are discrete planar layers defined by strong in-plane bonding that imparts stability to atomically thin layers, and weak out-of-plane interactions which make them distinct from their supporting substrate [15]. Crystallographically, a 2D material can be defined using two lattice parameters, which should be non-degenerate when compared to a bulk lattice. The exact in-plane bonding structure of the 2D material often leads to emergent properties distinct from bulk counterparts.

2.1: Materials Stable in Two Dimensions

2.1.1: Thermodynamically unstable materials

2D materials, theoretically formed from reducing bulk crystals to single atomic planes, have introduced a new engineering approach to materials. Despite early demonstrations of covalently bonded atomic layers on metals [16-18] or SiC [19], the notion of free-standing 2D materials were suggested to be unstable owing to thermal fluctuations which would ultimately destabilize the material [20]. At the time, it was believed that the thermal fluctuations in atomically thin crystals were greater than interatomic interaction strength, thereby requiring a 3D bulk crystal to stabilize 2D structures. These assertions were challenged by the successful isolation of graphene (a single atomic layer of graphite) in 2004 [21], and even more so with the demonstration of suspended membranes [15]. The strong in-plane C-C covalent bonds were critical for stabilizing graphene and other 2D materials, making them robust to thermal fluctuations.

2.1.2: Bonding in 2D materials

2D materials are discrete atomic layers, distinct from other surface structures (i.e. surface reconstructions and compounds), owing to both strong intramolecular bonding and weak interactions with their surroundings which enables the formation of discrete structures of purely surface. These purely surface structures exhibit properties distinct from the bulk surface, owing to unbound orbital interactions across the 2D material and the confinement of the electronic structure down to a single atomic layer. Even at the few-layer limit, these unbound orbitals interact across the layers, adding new electronic states to the system. In fewer than ten atomic layers, 2D materials achieve bulk-like properties, so the successful isolation of the material at the single layer limit is crucial.

In-plane covalent bonding not only stabilizes 2D materials, it also dictates the exact structure of the material and it need not be entirely planar. Planar structures such as graphene and hexagonal boron nitride (hBN), are mechanically robust covalent planar hexagonal networks formed from a single layer of sp^2 -hybridized atoms. Whereas mixed sp^3 - and sp^2 -hybridization leads to the formation of partially buckled structures nonetheless isolated from their surroundings. Compound structures, such as the covalently bonded of Transition metal dichalcogenides (TMDs), have unbound sp^3 orbitals oriented normal to the surface by the pyramid network of covalent bonds. Thus, the challenge in the ongoing effort to develop new 2D materials is two-fold: synthesize structures stabilized by strong intraplanar bonding and isolate these structure from their surroundings.

2.2: 2D material synthesis

Initially, isolation of 2D materials was achieved through mechanical exfoliation (i.e. the scotch tape method) of bulk material, yielding micron-sized sheets of single atomic layers. Novoselov and Geim's scotch-tape method [21] has been widely adopted by the research community for its simplicity to produce well-isolated pristine samples. This approach exclusively produces flakes of 2D material from bulk 3D allotropes and cannot be used to generate new 2D structure or reliably synthesize large-area sheets of 2D materials. Epitaxial growth [e.g. chemical vapor deposition (CVD) and physical vapor deposition (PVD)] [22] on single-crystal substrates has proven the most reliable approach towards producing pure large-area 2D materials [23]. In contrast to traditional monolayers, which rely critically on lattice matching between adatoms and the surface, the interfacial interactions of 2D materials are superseded by the formation of the strong in-plane covalent bonding characteristic of 2D materials. Thus, even when the substrate interactions relatively strong, it is possible to produce an atomic layer of a single-crystal 2D structure across large-areas with an unperturbed in-plane structure.

2.2.1: Chemical Vapor Deposition

Chemical vapor deposition (CVD) employs high-purity molecular precursors (e.g. methane) on a catalytically active substrate to which combine to form solid layers on the surface [24]. The precursors, though most commonly gaseous, also include liquids and solids vapor, flown in an inert gas to the substrate target. Heating of the substrate during or after deposition is often necessary to both decompose the precursors and allow diffusion of species on the surface to form uniform films. Synthesis conditions vary, reflected by a myriad of classifications used to reflect the parameters of the CVD process.

2.2.2: Physical Vapor Deposition

Physical vapor deposition (PVD) typically involves deposition of atomic species via molecular beam evaporator (MBE) using an e-beam evaporator (EBE), Knudsen cell, or other solid phase deposition source under ultra-high vacuum (UHV). The atomic sources used are typically high-purity with well calibrated deposition rates, enabling growth of desired fractions of 2D monolayers achieved by adjusting the deposition time. Introduction of reactive gaseous molecules in series with atomic deposition expands the capabilities of PVD. Layer-by-layer growth of binary alloys is possible, but typically requires specialized systems equipped with sub monolayer *in situ* monitoring analysis, meant to grow a specific class of materials. Apart from *in situ* growth rate monitoring, UHV enables measurements of the pristine material using techniques only suitable in vacuum.

2.2.3: Growth from bulk Material

Selective etching and isolation in solution-based systems is among the most common approaches to isolate 2D materials from bulk [25,26]. Though the strengths of this approach are the production large quantity of multilayer, rather than the growth of high-quality films. Isolation of 2D materials from the bulk can also be achieved through the selective diffusion of a specific bulk species, such as Si from SiC. Once the C-rich SiC(0001) $6\sqrt{3} \times 6\sqrt{3}$ buffer layer achieves a sufficiently high C concentrations, the excess C condenses into a graphitic layer, separated from Si-dangling bonds. This separation can occur also by passivation the surface with gaseous species, which has also been shown to stabilize films grown by other methods [27].

2.3: Properties of Graphene

The atomically thin honeycomb lattice endows graphene with tremendous mechanical strength [28], optical transparency (97.7% for visible light) [29], and relativistic charge transport [21]. For more information on fundamentals of graphene, which are only briefly discussed herein, the reader is referred to the progress article by Geim and Novoselov [30].

2.3.1: Graphene honeycomb structure

Graphene is a single atomic layer of the sp^2 -bonded hexagonal form of bulk carbon (i.e. graphite). The 2D honeycomb lattice can be **crystallographically** described by a 2D hexagonal lattice (crystallographic plane group: $P6mm$). Though the edges of the honeycombs are $d = 1.42 \text{ \AA}$, the primitive unit cell needed to describe the lattice is given by $a = b = 2.459 \text{ \AA}$ and $\gamma = 120^\circ$ with a 2-atom basis positioned at $2/3, 1/3$ and $1/3, 2/3$. Graphene therefore has an in-plane density of 38.20 C/nm^2 .

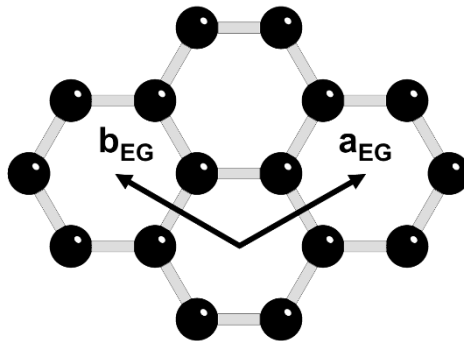


Figure 2.1: The crystal structure of graphene, defined by lattice vectors \mathbf{a}_{EG} and \mathbf{b}_{EG} .

This beautifully simple crystal structure embodies the characteristics of an ideal 2D material. The sp^2 -bonded character of carbon within graphene results in strong in-plane bonding (7 eV per

C atom) from localized σ -bonding formed with the three nearest neighbor carbon atoms. The unbound $2p_z$ orbital, orthogonal to the atomic plane, forms weak π -bonds (40 meV per C atom [31]) which interact with neighboring $2p_z$ orbitals to form delocalized states across the top and bottom surfaces of graphene. The success of graphene follows that of other low-dimensional forms of carbon, 0D fullerenes [32] or 1D nanotubes [33], all of which are derivatives of the 2D honeycomb basis.

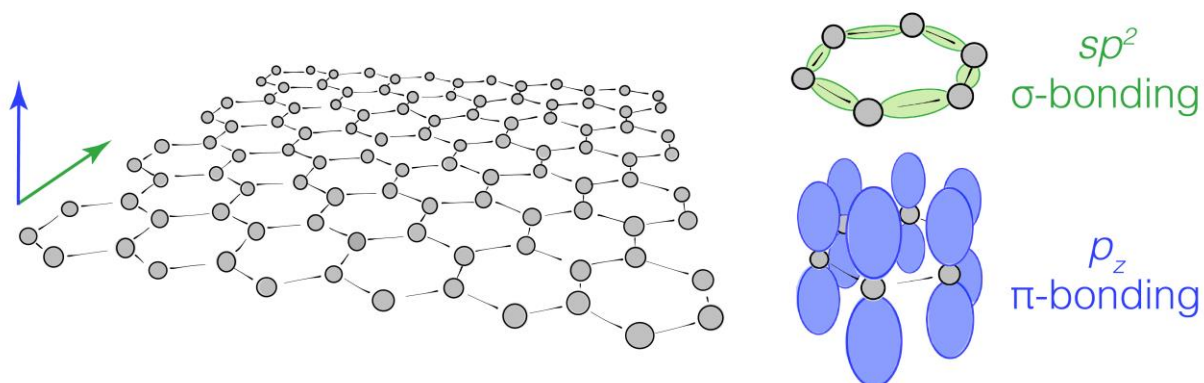


Figure 2.2: Schematic of graphene, with carbon atoms indicated by grey circles. (Left) The 2D honeycomb structure of graphene with the orientation of the (Right) σ -bonded sp^2 and π -bonded $2p_z$ orbitals indicated by green and blue arrows respectively. (Source: from Ref. [34]).

2.3.2: Graphene electron structure

The weakly interacting π -bonding of the $2p_z$ orbitals in graphene enable charge carriers to transition seamlessly between electrons and holes. These delocalized states across graphene give rise to an ambipolar electric field effect, with carrier mobilities (μ) exceeding $15,000 \text{ cm}^2 \cdot \text{V}^{-1} \cdot \text{s}^{-1}$ under ambient conditions [21,35]. Though such high mobilities have been seen in other materials, the charge carriers in those materials are described well with the Schrödinger equation. Whereas the charge carriers in graphene exhibit relativistic character best described with the Dirac equation from quantum electrodynamics. The relativistic movement of charge particles provides a new

means to explore predictions of (2+1)-dimensional quantum electrodynamics [36-38]. The interaction between these charge carriers and the graphene lattice gives rise to Dirac fermions, where electrons with no effective mass (m_e) give rise to a linear dispersion relation and ballistic transport of charge carriers near with drift velocities (v_d) = 10^6 m·s⁻¹.

2.4: Properties of Elemental 2D Materials

The collection of elemental 2D materials capable of forming strongly covalently bonded networks are referred to as Xenos. Of the Xenos, only two elements, C and P, have known layered bulk allotropes [i.e. graphite and black phosphorus (BP)]. The remaining Xenos (Si, B, Ge, and Sn) are so-called synthetic elemental 2D materials (SE2DMs), and have no corresponding bulk allotropes. SE2DMs are synthesized through appropriate choice of substrate, which suppresses the energy cost of planar configurations of atoms below otherwise thermodynamically favorable bulk nanoclusters. Although several stable SE2DM structures have been proposed by theory [39,40], experimental verification of these proposed structures, particularly when isolated from their supporting substrate, are relatively sparse owing to rapid degradation under ambient conditions [6]. Thus, it remains unclear if SE2DMs would remain intact as freestanding 2D layers when isolated from their support substrate.

2.4.1: Buckled 2D structures

Aside from graphene, no Xene is known to form a purely sp^2 -bonding planar structure, instead they are hypothesized to exhibit mixed sp^2 - sp^3 covalently buckled networks [39,40]. The proposed buckled structures of several Xene polymorphs can be understood by examining single atomic layers of P from its buckled bulk allotropes, BP and its α -As variant [41]. The multiple geometries of P-P bonding in BP lend additional degrees of freedom from which many plausible

buckled 2D allotropes have been derived. Four 2D phosphorus (α -P, β -P, γ -P, and δ -P) allotropes [42] have been computationally predicted by geometrical manipulations of P-P bonding in monolayer BP with blue phosphorus (β -P; a single atomic layer of α -As BP [43]) recently synthesized experimentally [44]. Nine others predicted P allotropes have been predicted through more aggressive alterations [45] of BP.

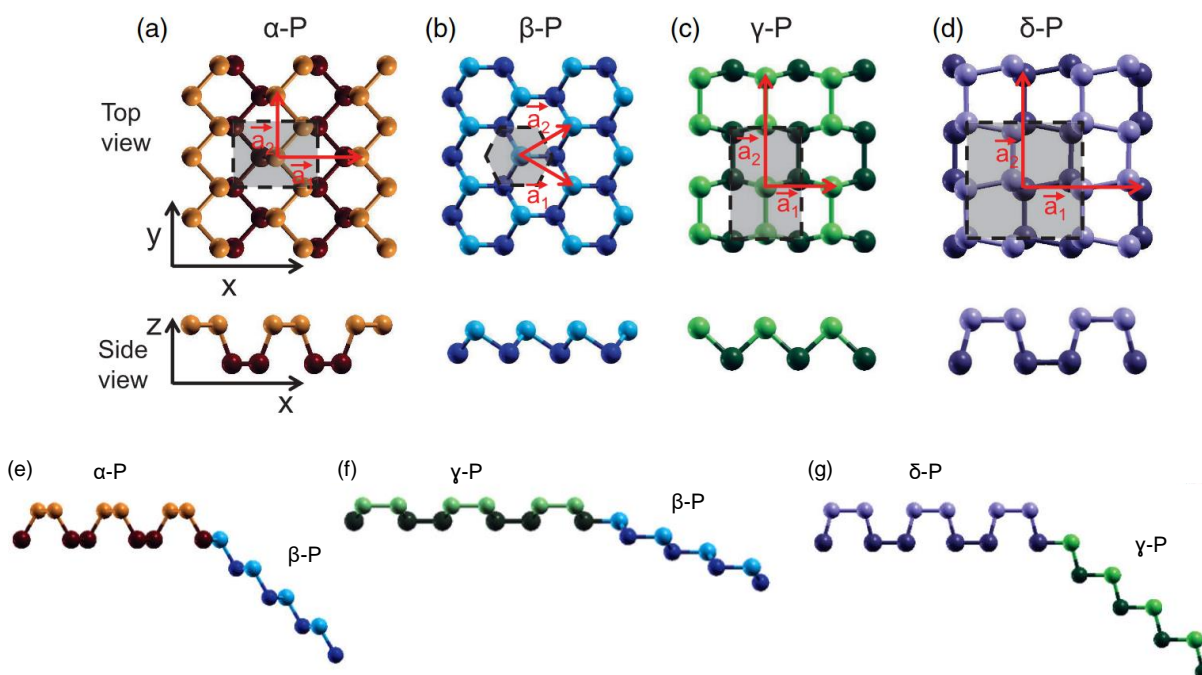


Figure 2.3: Predicted 2D phosphorus crystal structures of (a) α -P (BP; black phosphorus), (b) β -P (blue phosphorus), (c) γ -P, and (d) δ -P with the unit cell shown by a grey box outlined with a black dotted line and basis vectors \mathbf{a}_1 and \mathbf{a}_2 shown in red. The modifications to the lattice to construct these phases is shown for (e) β -P from α -P, (f) β -P from γ -P, and (g) γ -P from δ -P (Source: adapted from Ref. [42])

While 2D phosphorus and 2D carbon have layered bulk allotropes, which provide a basis for structure determination, the structure of SE2DMs requires more advanced surface characterization techniques, the interpretation of which are further hampered by substrate influence. Like BP, multiple 2D buckled allotropes of silicene (3×3 [7], $\sqrt{13} \times \sqrt{13}$, $\sqrt{7} \times \sqrt{7}$, and $\sqrt{3} \times \sqrt{3}$ [8,46]) have been proposed. The challenges in determining the structure of SE2DMs are

evident from ongoing efforts to characterize the $\sqrt{3} \times \sqrt{3}$ phase of silicene on Ag(111). Initially, this phase was attributed to a free-standing buckled honeycomb silicene structure [40], similar to β -P. A $\sqrt{3} \times \sqrt{3}$ phase of Si deposited on Ag(111) observed by scanning tunneling microscopy (STM) [46] was attributed to the formation of a honeycomb silicene structure, which was further validated by first-principles calculations [47]. Further structural analysis of the $\sqrt{3} \times \sqrt{3}$ phase of silicene revealed it to share striking similarities to an Ag-Si reconstruction atop bulk Si layers [8], which match rigorous structural analysis of an Ag-induced $(\sqrt{3} \times \sqrt{3})R30^\circ$ reconstruction of Si(111) [48]. Likewise, recent theoretical work of Si on Ag(111) reveals the formation of Si-Ag alloys to be energetically favorable to freestanding Si [10].

2D Boron (borophene), like silicene, shows multiple structures when synthesized on Ag(111). Like other SE2DMs, STM analysis of borophene matches simulated STM images from theoretically predicted buckled structures [6]. The same structure seen in STM also match a vacancy mediated [49] structure. These phases are discussed in greater detail in chapter 3, and in chapter 5 we report the results of our investigation into the interface structure of borophene on Ag(111).

Chapter 3: Structure of 2D Materials on Substrates

3.1: Interactions at interfaces

2D materials, being atomically flat structures, bode well to epitaxial growth on single-crystal substrates. The interfaces between 2D materials and substrates differ from other monolayer materials owing to the formation of strong in-plane covalent bonds, which supersede substrate interactions by an order of magnitude that would otherwise lead to adlayer formation. Nonetheless, the interaction strength between growth substrates and 2D materials often exceed the forces in bulk vdW solids, ranging from physisorption [50] to strong hybridization of atomic sites in the 2D material [51]. By breaking the quantum confinement with a reactive substrate, 2D materials can develop strain, doping, and structural changes in response [11-13]. Controlling the degree of interaction at this interface is therefore critical to retain the desired properties of 2D materials.

Substrate choice is often restricted to materials with sufficient catalytic interactions, which are vital for bottom-up synthesis of 2D materials via CVD and PVD. The precise interaction strength of the synthesized 2D material and the substrate is revealed by the vertical distances between them, revealing the types of bonding present in the system. Covalently bonded substrates and surface compounds, show a maximum vertical separation equal to the covalent bond length (e.g. 1.54 Å for diamond), which is further reduced when the covalent bond is off-normal with respect to the substrate surface. While weakly interacting substrates via vdW epitaxy [52] show a gap similar to a vdW bonded bulk solid (e.g. 3.36 Å for graphene). Therefore, directly measuring the interface structure elucidates the bonding present at the interface. For 2D materials with bulk

allotropes, epitaxy is primarily a means to produce high-quality 2D crystals, and any interactions with the substrate are inferred from changes to the electronic structure in the 2D material. Whereas for SE2DMs, substrate interactions are a critical component of stabilizing otherwise thermodynamically unfavorable structure [53]. Deconvoluting substrate interactions from the measured properties of SE2DMs is exceptionally challenging without pristine SE2DM properties as a basis for comparison. Thus, the degree of interaction between substrate and SE2DMs cannot be easily inferred and instead must be measured directly.

3.2: Epitaxial Graphene on Single-Crystals

Local fluctuations in amorphous and polycrystalline substrates, on the length scale of the hexagonal honeycomb structure of graphene, introduce periodic impurities in the graphene [54]. The desire to produce grain-boundary free 2D crystals motivated the growth of graphene on single-crystal surfaces with well-defined terraces [55]. Even when the graphene in-plane structure is unperturbed, interface scattering of the π - π coupled $2p_z$ orbitals from the substrate can hinder charge transport [13], which is reflected in the precise interface structure of the epitaxial graphene.

Initial demonstrations of CVD graphene yielded polycrystalline graphene films. The weakest substrate interactions are unable to impose rotational registry, leading to polycrystalline graphene, which shows reduced conductivity owing to scattering at the in-plane grain boundaries [56]. On the other hand, strongly interacting substrates, like Ni, can lead to chemical bonding and reduced electronic performance [57,58]. Herein, we review the precise interface structure dependence of epitaxial graphene on metal, Ge, and SiC single-crystals. For a summary of the growth and characterization of epitaxial graphene, the reader is directed to review articles by

Tetlow and Kantorovich [59] and Batzill [60] for graphene on metals, Riedl and Starke [61] and more recently Norimatsu and Kusunoki [62] for graphene on SiC.

3.2.1: Epitaxial Graphene on Metals

Single-crystal metal substrates were among the first to produce large-area epitaxial graphene, largely owing to their ability to catalyze carbon CVD precursors. The metal-carbon interactions which enable graphene epitaxy, leave the in-plane structure of graphene preserved, owing to extremely ridged in-plane C-C bonding. Biaxial strain is also energetically unfavorable, as graphene cannot realistically achieve commensuration with a substrate using in-plane strain more than $\sim 1\%$, leading to other relaxation mechanisms. Most commonly, the interface structure between graphene and lattice-mismatched hexagonal array of metal substrate surface atoms is a vertically corrugated moiré superstructure, where $(m \times m)$ graphene unit cells are matched to $(n \times n)$ substrate unit cells, often rotated either 0° or 30° relative to each other from the hexagonal symmetry of graphene. The large 2D lattice, formed by the shared lattice points of the epitaxial graphene (EG) and underlying metal substrate surface atoms, is referred to as the EG/M superlattice. The distance between carbon and substrate atoms vary considerably across the EG/M lattice vectors, so too does the interaction strength between the atoms, as is evident from changes to the C1s photoelectron spectra [63].

Table 3.1: The closest separation in EG/M, measured between parallel planes defined by the innermost carbon atoms in EG and metal substrate atoms directly underneath them. (Source: adapted from Ref. [60])

Substrate	Closest Separation (Å)
Ni(111)	2.1 [57,58]
Co(0001)	2.1 [64]
Ru(0001)	2.1 [65,66]
Rh(111)	2.2 [67]

Re(0001)	2.1 [68]
Pd(111)	2.5 [69]
Cu(111)	3.3 [70]
Pt(111)	3.3 [69-73]
Ag(111)	3.3 [70,72,73]
Au(111)	3.3 [70,72,73]
Ir(111)	3.4 [72,74]
Fe(110)	2.1 [75]

The structure of epitaxial graphene on metals can range from covalent-like to vdW-like with the corresponding gap between 2.1 Å and 3.4 Å, listed in Table 3.1. The interaction between EG and the substrate shows a correlation with d-orbital to π -bond interaction [76]. For the weakly interacting EG/M with a vdW-like vertical separation, the electronic structure reflects pristine graphene aside from a shift in the graphene Dirac point owing to charging from the work function difference between metal and graphene. Whereas strongly interacting substrates induce sp^3 bonding character in the overlaying graphene, revealed by a binding energy shift in the carbon 1s photoelectron spectra and a vertical buckling of the graphene, showing in Figure 3.1.

EG on face-centered cubic (FCC) Ni(111) [57,58] and EG on Hexagonal Co(0001) [64] show among the strongest EG/M interactions and best lattice matching (lattice mismatch < 2%), with band hybridization occurring between the metal d-electrons and the graphene π -orbitals. The (111) surface of Ni and (0001) surface of Co are in (1×1) registry with graphene, and therefore does not form a moiré superstructure. The EG interacts strongly with the underlying substrate, buckling slightly and sitting 2.11 Å and 2.16 Å atop the Ni(111) surface [57]. Similar values are achieved for EG atop Co(0001) [64]. The graphene-Ni interactions are strong enough to form carbide compounds at low temperatures [77,78]. Nonetheless, the absorption energy of graphene

on Ni(111) is comparable to physisorption (70 meV per C atom) [79], making it a useful substrate for subsequent transfer.

EG on Ru(0001) [65] [66], Rh(111) [67], and Re(0001) [68] also show strong EG/S interactions, showing a minimum surface separation of 2.1 Å. These metals are highly lattice mismatched with graphene, a corrugated moiré structure forms to accommodate the mismatch. The (23x23) Ru(0001), (11x11) Rh(111), and (9x9) Re(0001) moiré patterns showing areas buckled outward 0.6 – 1.6 Å, 1.5 Å, and 1.6 Å, respectively.

Graphene shows weaker interfacial interactions with the noble metals, Cu(111), Pt(111), Ag(111), Au(111) and Ir(111) [70,72,73]. These interactions are not fully vdW, as is evident by the formation of moiré patterns to accommodate the lattice mismatch between EG and these metals. The EG/Ir(111) moiré pattern shows a 3.41 Å vertical gap, but with undulations of no more than 1.0 Å [74]. This ~1.0 Å has been attributed to graphene physisorption and chemisorption across the Ir(111) surface. These weakly interacting systems also allow the formation of multiple orientations of EG, even when in epitaxial registry, as was the case for graphene on Cu(111) [80].

EG on Fe(110) [75] is distinct from other metals as there is no symmetry matching between substrate and EG, which is typically needed for epitaxy. The graphene is strongly electronically coupled to the underlying Fe(110) substrate and stabilized by the formation of long-range corrugations with a ~4 nm period. The stability of these corrugations is compromised at elevated temperatures (630 °C), resulting in carbide formation.

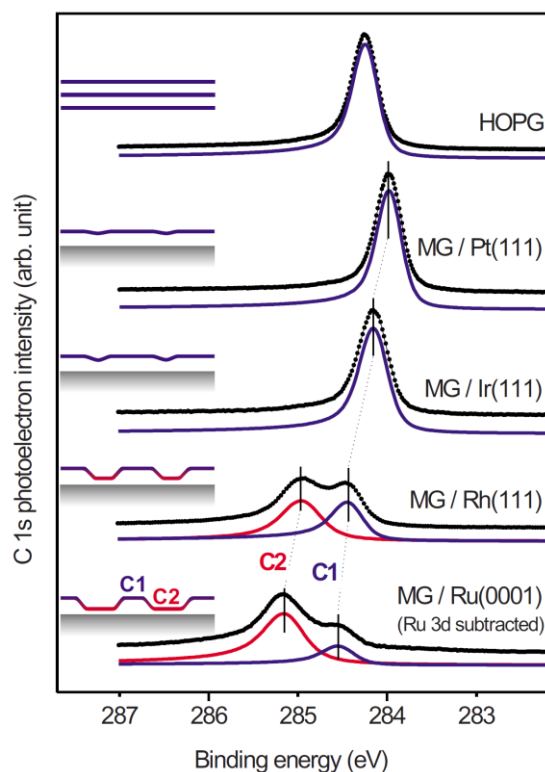


Figure 3.1: C 1s photoelectron spectra of graphene taken using a 400 eV X-ray source. Spectra are from monolayer graphene on metal substrates, with highly ordered pyrolytic graphite given as a reference standard. (Source: from Ref. [63])

3.2.2: Epitaxial Graphene on Ge

Epitaxially aligned graphene on the (110) face of single-crystal Ge offer a means to produce high-quality graphene without the fermi-energy shifting associated with metal substrates [81]. The zig-zag and armchair directions of graphene lie parallel to the [001] and $[\bar{1}10]$ directions of the Ge(110) face, making a perfect large-area single-crystal with superior electronic properties (mobility $\sim 10,000 \text{ cm}^2 \cdot \text{V}^{-1} \cdot \text{s}^{-1}$) compared to other Ge faces. Much weaker alignment was seen between graphene and Ge(111) face, leading to polycrystalline graphene. This has been verified by Raman and X-ray photoelectron spectroscopy (XPS), which show significant doping effects on the (111) surface, while minimal doping are seen on the (110) surface [82]. The weak bonding

between the EG and Ge(110) surface is also clear from the successful transfer of graphene off of Ge(110) via mechanical exfoliation.

The superior quality of Ge(110) has been attributed to the anisotropic C-Ge bonding during nucleation. This bonding, accompanied by the nucleation of graphene islands, appears to be most prominent at Ge(110) step edges. This is hypothesized to occur from in-plane lattice matching of the graphene and Ge(110) step edges, allowing the formation of periodic C-Ge bonds, but leaving a vdW gap underneath the graphene sheets [83]. The Ge(110) surface is believed to be pristine and protected from oxidation by the graphene overlayer [84]. This interface also appears free of C-Ge compounds, as the solubility is extremely low in Ge, and C-Ge phase diagram is free of compounds near the Ge melting temperature [85]. In contrast to graphene corrugations typically associated with moiré patterns, the corrugations seen in EG on Ge(110) appear to be due to the rearrangement of Ge.

3.2.3: Epitaxial Graphene on SiC

Epitaxial graphene can be produced directly from a SiC wafer, without the use of carbon precursors, using the preferential sublimation of Si from SiC single-crystal in an inert environment (such as UHV). At high temperatures, Si sublimates more readily than C, leading to a buildup of excess carbon at the surface, which rearranges to form graphene. Formation of additional graphene layers occurs continuously at the EG/SiC interface with the further sublimation of Si. Following this demonstration, epitaxial graphene has also been grown on SiC by CVD [86] and PVD [87], boasting weaker substrate interactions and lower growth temperatures.

The most commonly used SiC allotropes for graphene synthesis are 4H-SiC and 6H-SiC, which have a layered unit cell with 4 and 6 layers of SiC respectively. Using the (0001) Si-

terminated cleaved surface orients the surface normal along the stacking direction of Si and C, ideal for graphene growth. Initially, the carbon-rich surface forms a SiC(0001) $(6\sqrt{3} \times 6\sqrt{3})R30^\circ$ surface reconstruction, where $R30^\circ$ indicates the orientation relative to the underlying SiC. This C-rich reconstruction is partially covalently bonded to the underlying SiC (Figure 3.2), exhibits an in-plane structure distinct from the graphene honeycomb, and readily scatters charge carriers. The C-terminated $(000\bar{1})$ direction will also produce graphene, but without the consistent epitaxial registry seen on the Si-terminated side.

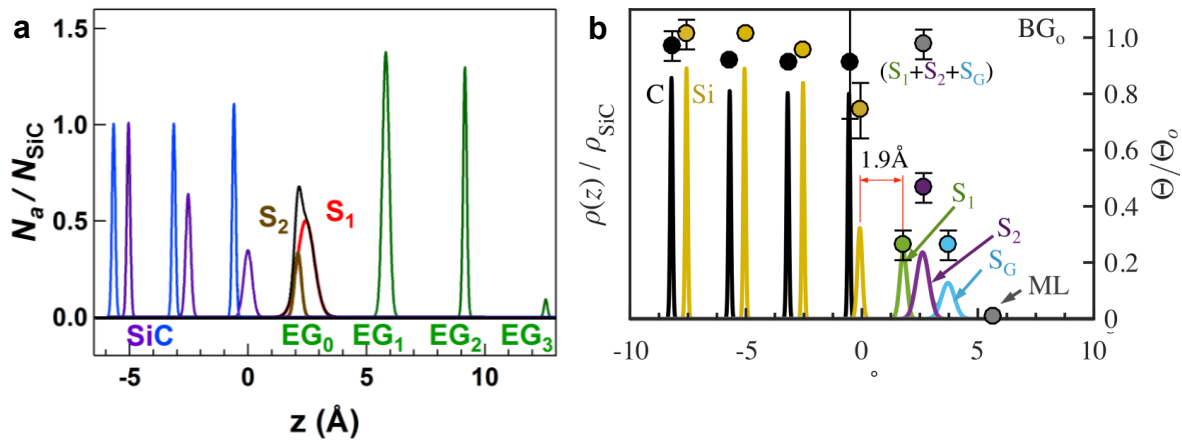


Figure 3.2: The vertical electron density profile of EG on SiC(0001) interface derived from X-ray standing wave constrained X-ray reflectivity. (a) 1.3 ML of graphene on SiC (b) 0 ML of graphene on SiC. (Source: (a) adapted from Ref. [14] and (b) adapted from Ref. [88])

Through atomically thin layers of graphite were demonstrated using this approach as early as 1998 [19]. These layers were not of sufficient quality to reproduce the charge transport properties of graphene, when this approach was first demonstrated in UHV heating at 1600 K [19]. The obstacles to producing monolayer graphene primarily stemmed from the 3 layers of C in SiC needed to produce the SiC(0001) $(6\sqrt{3} \times 6\sqrt{3})R30^\circ$ reconstruction and each subsequent layer of monolayer graphene. Quality of films has increased dramatically with reduced rates of Si

sublimation under Si-rich atmosphere [89] or buffer gas such as Ar [90-92] at 1900 K. Both approaches allow higher mobility of the C atoms at the surface, leading to the demonstration of near continuous monolayers of EG on SiC.

3.3: Epitaxial Borophene

Recently, atomically thin sheets of boron (i.e., borophene) have been grown on silver surfaces with structures distinct from known bulk boron allotropes [5,6]. Theory predicts the in-plane B-B bonding (3 eV per B atom) to greatly exceed interactions with the substrate (100 meV per B atom) and form a stable free-standing structure [49,93]. These sheets are evidently the lightest known 2D metals [93-95], exhibiting anisotropic Dirac fermions and predictions of relatively high T_c superconductivity which may elucidate the fundamental origins of metallicity and correlated electron phenomena (e.g., superconductivity) in light elements [96,97]. Though the interface between the borophene and the underlying silver has been predicted to play a role in stabilizing borophene over more energetically favorable bulk structures [49,98], experimental measurements of chemically resolved interface structure remain elusive.

3.3.1: Borophene R and D phases

Borophene deposited on silver shows at least 2 distinct lattice structures, one phase shows a rectangular (R) 2D lattice structure, the other a diamond (D) (a.k.a. rhombic or face-centered rectangular) 2D lattice structure, both are in registry with the underlying Ag(111) substrate [5,6]. Since initial experimental demonstrations of borophene, additional borophene structures have also been reported, believed to be reconstructions of the Ag surface [99,100]. The STM derived lattice shows the R phase can be described with lattice vectors $|\mathbf{a}| = 5.0 \text{ \AA}$ and $|\mathbf{b}| = 2.9 \text{ \AA}$. Likewise the

D phase can be described with $|\mathbf{a}| = |\mathbf{b}| = 4.6 \text{ \AA}$ and $\gamma = 142^\circ$ [101], verified by low-energy electron diffraction (LEED).

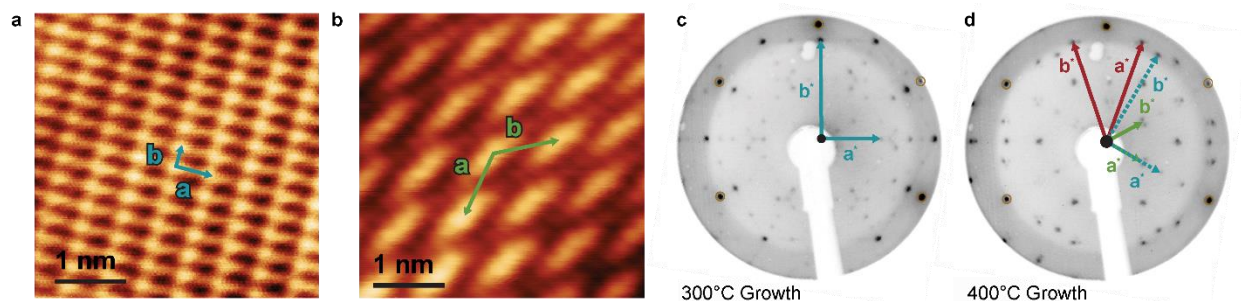


Figure 3.3: Borophene lattice and atomic structures. (a,b) STM topography images showing the atomic-scale structures corresponding to the R and D phases. (f,g,h) LEED patterns acquired at 70 eV, corresponding to (c) borophene growth at 300 °C (predominantly R phase), and (h) borophene growth at 400 °C (predominantly D phase). (STM images in a and b provided by A.J. Mannix)

STM imaging further reveals the R phase and D phase coexist on Ag(111) terraces, but as distinct domains of borophene. Different ratios and relative orientations of these phases can be achieved by modifying deposition temperature and atomic boron deposition rate {site unpublished LEED paper}. These phases appear to exist only as monolayers, with the formation of bulk boron clusters forming at high atomic boron surface coverage [6].

3.3.2: Atomic Models of Borophene

The atomic basis of borophene (i.e. the arrangement of boron atoms within the unit cell) has not been measured directly. Density functional theory (DFT) calculations predict a large degree of polymorphism in 2D boron structures [93], with at least two distinct models matching the experimental STM data for the R phase of borophene. The first R phase model, called the α -sheet [94,102] is a buckled triangular lattice, akin to graphene with the hexagonal honeycombs completely filled. The vertically displaced atoms sitting one sitting 2.5 \AA above the Ag(111) surface and the other buckled an addition 0.8 \AA outward to sit 3.3 \AA above the Ag(111) surface

[6]. The second R phase model, called β_{12} , features a highly-planar sheet of B atoms with a vacancy concentration $\nu = 1/6$ of the triangular lattice sites. Alternatively, this can be thought of as a graphene lattice, with $1/2$ of the honeycombs filled with additional boron atoms. The D phase of borophene is predicted from a slight modification to the β_{12} model, by using $\nu = 1/5$ to generate the χ_3 model, which achieves a diamond vacancy configuration [49]. Calculated STM data (Figure 3.4) from the α -phase, β_{12} , and χ_3 models closely match experiment, and both phases are reasonably lattice matched to the Ag(111) substrate $\sim 3.1\%$ for α -phase and $\sim 1\%$ for β_{12} [100]. Recent review articles by Zhang [103] and Mannix [104] acknowledge that current experimental results are insufficient to unambiguously resolve the structure of borophene. To break the degeneracy of proposed structure requires orthogonal structural descriptions as well as chemical specificity, ideally with *in situ* measurements. To this end, XSW-XPS was employed as a chemically sensitive vertical probe to resolve this structure, discussed in chapter 5.

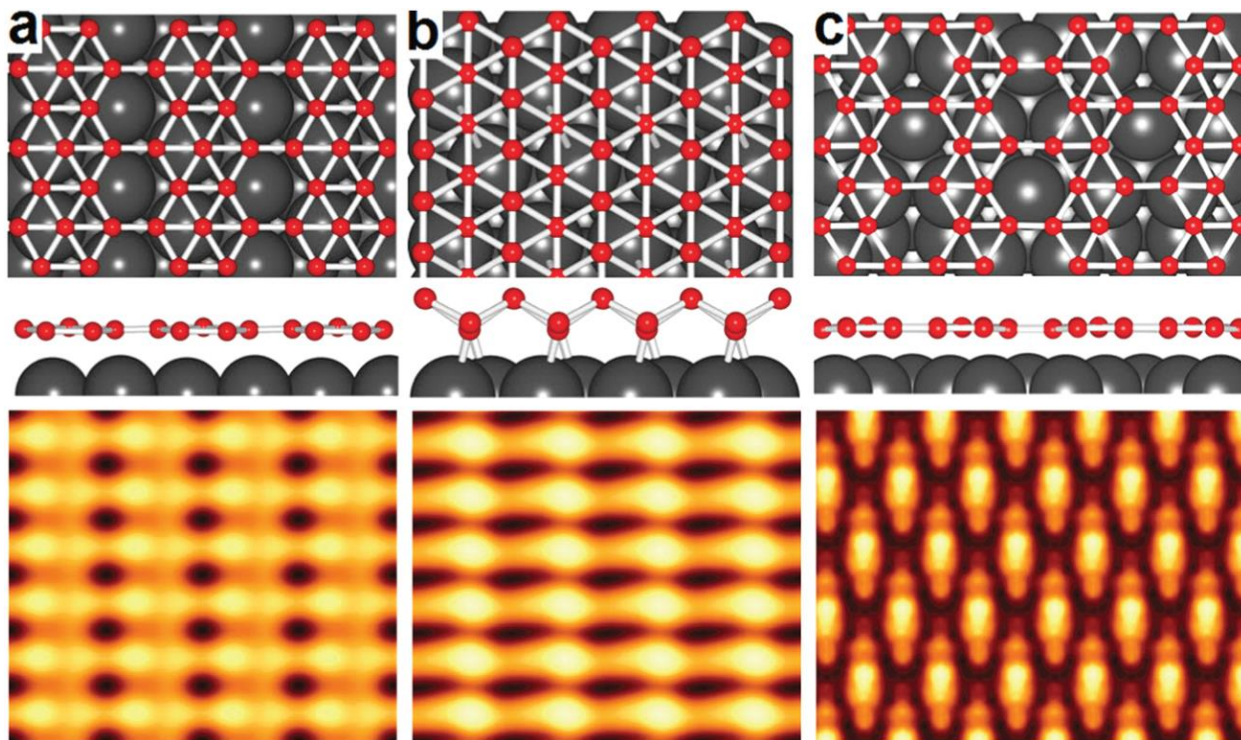


Figure 3.4: Proposed atomic models for borophene on Ag(111), namely (a) β_{12} phase (b) α -phase (c) χ_3 phase. (Top) top-view, (Middle) side-view, (Bottom) simulated STM topography images showing the atomic-scale structures. (Source: from Ref. [103])

3.4: vdW Epitaxy

The desire to produce pristine layers of 2D materials without a reactive substrate and ongoing efforts to make vertical 2D heterostructure devices [105] has driven investigation into using pure vdW interactions to drive epitaxy. Van der Waals epitaxy was proposed in 1992 [52], well before the demonstration of 2D materials in 2004 [21], as a means to achieve registry between highly mismatched substrate lattices. Van der Waals epitaxy is a careful balance of substrate-overlayer interactions strong enough to enable single-crystal 2D material growth, but weak enough where the in-plane 2D material structure is preserved. For the case of 2D materials, unbound orbitals between two materials interact through vdW attractions to drive orientational registry without disrupting the electronic or lattice structure of either material [106,107].

Graphene, with its orthogonally arranged $2p_z$ orbitals, can drive orientational registry without compromising the structure of graphene, and maintain a graphite-like gap (0.33 nm) in 2D heterostructures. Graphene can also be used as a barrier layer to screen interactions between highly reactive substrates, enabling vdW epitaxy to occur through graphene between a substrate and overlayer [50].

Chapter 4: X-ray Characterization

Techniques

The challenge of deducing the chemically resolved vertical structure of 2D materials and their interface bodes well for study through X-ray interface science. X-rays have already been used extensively to study the structure of thin films and surface reconstructions. 2D materials represent the ultimately limit of these structures, being single-atomic layer films. X-ray based techniques (XSW, CTR, GIXS) are among the most precise vertical structure probes, allotting sub-Å sensitivity. Owing to weak interactions with matter that enable the study of buried interface. This dissertation demonstrates the use of synchrotron-based X-ray tools to solve the physics and chemistry of new surface structures, with an emphasis on determining the interaction strength of 2D structures with a given substrate. Herein are the brief derivations of X-ray interactions with matter relevant to understanding the work discussed in this document. Textbook descriptions of the interactions of X-ray with matter are given in Warren [108] or Als-Nielsen and McMorrow [109], and the specific case of hard X-ray photoelectron spectroscopy has been written by Woicik [110].

4.1: Introduction to X-ray physics

4.1.1: X-ray interactions with matter

X-rays have been used to probe materials since their discovery by Wilhelm Conrad Röntgen 1895. Röntgen's X-ray tube produced a small dose of X-rays over large-areas, which could effectively distinguish between materials with vastly different adsorption coefficients (e.g. skin and bone). High-intensity monochromatic X-rays enabled the determination of highly periodic

structures through X-ray scattering, including the celebrated discover of DNA helix structure [111]. The development of highly brilliant monochromatic X-rays using third generation synchrotrons enabled more exact chemical and structural information to be extracted from materials, such as those presented in this work.

X-rays are electromagnetic waves with Ångström (10^{-10} m) wavelength and photon energies in the keV. The relation between wavelength and energy is given by $E_\gamma = \frac{hc}{\lambda}$. The X-ray electric field traveling wave \mathbf{E} propagates with a wavelength λ along the wavevector $\mathbf{k} = \hat{\mathbf{u}} \frac{2\pi}{\lambda}$, where $\hat{\mathbf{u}}$ is the propagation direction unit vector. For linearly polarized X-rays which oscillate temporally with frequency ω over time t and spatially over \mathbf{r} , the X-rays are described by an electromagnetic planewave,

$$\mathbf{E}(\mathbf{r}, t) = \hat{\mathbf{e}} E_0 e^{i(\mathbf{k}\cdot\mathbf{r} - \omega t)} . \quad (4.1)$$

with amplitude E_0 and polarization unit vector $\hat{\mathbf{e}}$ of the electric field. Here we neglect the magnetic field of the electromagnetic wave, which has orders of magnitude weaker interactions with matter. When incident on matter, an X-ray photon interacts through scattering or absorption.

The elastic scattering of electromagnetic radiation by a single electron is described classically by Thomson scattering [108]. The electric field of the incident beam \mathbf{E}_i propagating along wavevector \mathbf{k}_i has intensity proportional to $|\mathbf{E}_i|^2$. The incident X-ray oscillates the electron which radiates a spherical wave \mathbf{E}_f inversely proportional to distance R from the electron with classical radius r_e . The acceleration of the electron oscillation observed from a wavevector \mathbf{k}_f is given by the relative polarization of the incident and radiated fields, $|\hat{\mathbf{e}}_i \cdot \hat{\mathbf{e}}_f|$. The relative radiated field is given by

$$\frac{\mathbf{E}_r}{\mathbf{E}_i} = -\frac{r_e}{R} e^{i(\mathbf{k}_f - \mathbf{k}_i) \cdot \mathbf{r}} |\hat{\mathbf{e}}_i \cdot \hat{\mathbf{e}}_f|. \quad (4.2)$$

For simplicity $\mathbf{k}_f - \mathbf{k}_i$ is defined as the momentum transfer vector \mathbf{q} and $|\hat{\mathbf{e}}_i \cdot \hat{\mathbf{e}}_f|$ as the polarizability p . The polarization factor, $P = |\hat{\mathbf{e}}_i \cdot \hat{\mathbf{e}}_f|^2$, depends on the geometry; for synchrotron experiments with linearly polarized incident X-rays $P = 1$ in the vertical scattering plane (σ -polarized) and $P = \cos^2(2\theta)$ in the horizontal scattering plane (π -polarized), while for an unpolarized lab source $P = \frac{1 + \cos^2 2\theta}{2}$. Where 2θ is the angle between \mathbf{k}_f and \mathbf{k}_i . The scattered intensity from a single electron measured in X-ray experiments is therefore

$$I = |\mathbf{E}_r|^2 = |\mathbf{E}_i|^2 \frac{r_e^2}{R^2} P. \quad (4.3)$$

Note that the phase information is lost when taking the complex conjugate $|\mathbf{E}_i|^2$, this is the phase problem in X-ray crystallography.

Now consider the atom made up of Z electrons described classically with a charge distribution $\rho(\mathbf{r})$. When considering X-ray scattering from atoms, only electrons need to be considered because X-ray interactions with electron is $\sim 10^7$ greater than nuclei. The scattered field is a superposition of the all scattering from all volume elements $d\mathbf{r}$ at positions \mathbf{r} within $\rho(\mathbf{r})$, described by the atomic form factor,

$$f^0(\mathbf{q}) = \int \rho(\mathbf{r}) e^{i\mathbf{q} \cdot \mathbf{r}} d\mathbf{r}, \quad (4.4)$$

where two points separated by \mathbf{r} have a $\mathbf{q} \cdot \mathbf{r}$ phase difference. The atomic form factor is a Fourier transform of the charge distribution. When all scattering elements are in phase $f(\mathbf{q} = 0) = Z$. With increasing \mathbf{q} , volume elements scatter out of phase and $f(\mathbf{q} \rightarrow \infty) = 0$.

Being bound to a nucleus, electrons in atoms cannot freely oscillate in response to an electric field. This delayed response relative to the driving field is described by reduced scattering length f' and phase lag by if'' ,

$$f(\mathbf{q}, \lambda) = f^0(\mathbf{q}) + f'(\lambda) + if''(\lambda), \quad (4.5)$$

known as the dispersion correction. This representation of the atomic form factor correctly accounts for the binding between electrons and the atomic nucleus and will be used when calculating X-ray interactions with a crystal in kinematical and ultimately dynamical diffraction theory.

4.1.2: Kinematical scattering from a crystal

The scattering of a single atoms is not sufficient to be detected experimentally, considering the interaction between the X-ray planewave and an ensemble of atoms enables Thomson scattering theory to be extended to real materials. Solid crystalline materials can be modeled by repeating a unit cell over set of lattice points to define 3D, 2D, or 1D structures. A crystal can be defined mathematically as the convolution of the unit cell with the set of lattice points.

The interaction between X-rays and a set of lattice points is described by the weak-scattering limit or kinematical approximation. Here, the influence of multiple scattering effects are neglected. In general, scattering from a collection of atoms can be described by the form factor,

$$F(\mathbf{q}, \lambda) = \sum_j f_j(\mathbf{q}, \lambda) e^{i\mathbf{q} \cdot \mathbf{r}_j}, \quad (4.6)$$

which is simply a sum over the atomic form factors $f_j(\mathbf{q}, \lambda)$ over j atoms at positions \mathbf{r}_j . For the case of crystal, the unit cell with vectors \mathbf{a} , \mathbf{b} , and \mathbf{c} is repeated in a set of lattice points defined by the vector $\mathbf{R}_n = n_1\mathbf{a} + n_2\mathbf{b} + n_3\mathbf{c}$. The form factor for a crystal can therefore be described by the product of unit cell structure factor with the lattice sum,

$$F(\mathbf{q}, \lambda) = F^{\text{u.c.}}(\mathbf{q}, \lambda) \sum_{\mathbf{n}} e^{i\mathbf{q} \cdot \mathbf{R}_{\mathbf{n}}} = \sum_{\mathbf{j}} f_{\mathbf{j}}(\mathbf{q}, \lambda) e^{i\mathbf{q} \cdot \mathbf{r}_{\mathbf{j}}} \sum_{\mathbf{n}} e^{i\mathbf{q} \cdot \mathbf{R}_{\mathbf{n}}}, \quad (4.7)$$

for a unit cell with j atoms and n lattice points. Taking the geometric expansion of each component of the lattice sum,

$$\sum_{n=0}^{N-1} e^{inx} = \frac{1 - e^{iNx}}{1 - e^{ix}}, \quad (4.8)$$

it is apparent that for large values of N , typical of crystalline solids, the lattice sum will be near unity unless $\mathbf{q} \cdot \mathbf{R}_{\mathbf{n}} = 2\pi$. This condition is fulfilled for a so-called reciprocal lattice set of vectors $\mathbf{G}_{hkl} = h\mathbf{a}^* + k\mathbf{b}^* + l\mathbf{c}^*$ where $\mathbf{G}_{hkl} \cdot \mathbf{R}_{\mathbf{n}} = 2\pi(hn_1 + kn_2 + ln_3)$ and results in large values for the structure factor and reflected intensity. For the limit of $N \rightarrow \infty$, the reciprocal lattice defined by \mathbf{G}_{hkl} reduces to a set of δ -functions or so-called reciprocal lattice points. A reciprocal lattice point \mathbf{G}_{hkl} is the Fourier transform of the real space set of $H = hkl$ lattice planes with spacing d_{hkl} where $|\mathbf{G}_{hkl}| = \frac{2\pi}{d_{hkl}}$. The scalar geometry for the fulfillment of this condition is Bragg's Law,

$$|\mathbf{G}_H| = |\mathbf{q}| = \frac{4\pi}{\lambda} \sin\left(\frac{2\theta_B}{2}\right), \quad (4.9)$$

where the angle θ_B describes the angle of an incident and reflected plane wave relative the sample surface plane. The vector geometry is therefore described by

$$\mathbf{G}_H = \mathbf{q} = \mathbf{k}_H - \mathbf{k}_0. \quad (4.10)$$

Using the kinematical approximation developed thus far, the reflected $\mathbf{E}_r \propto F(\mathbf{q}, \lambda)$, thus the intensity at this condition is then given by $I(\mathbf{q}, \lambda) = |F(\mathbf{q}, \lambda)|^2$ when considering a perfectly rigid single-crystal. Real crystals experience lattice vibrations originating primarily from thermal vibrations of atoms. The instantaneous position of an atom is then given by $\mathbf{R}_{\mathbf{n}} + \mathbf{u}_{\mathbf{n}}$, where $\mathbf{u}_{\mathbf{n}}$ is

the displacement from the average atomic position. The time average the displacement, $\langle \mathbf{u}_n \rangle = 0$.

Evaluating the time-averaged structure factor with $\mathbf{R}_n + \mathbf{u}_n$ results in

$$I(\mathbf{q}, \lambda) = \langle |F(\mathbf{q}, \lambda)|^2 \rangle = |F(\mathbf{q}, \lambda)|^2 e^{-\frac{1}{2} \mathbf{q}^2 \cdot \langle \mathbf{u}_n^2 \rangle}, \quad (4.11)$$

where the exponential term is the Debye-Waller factor. The mean-squared amplitude $\langle |\mathbf{u}_n|^2 \rangle$

depends on the energy of the thermally excited phonons. For isotropic vibrations $\langle |\mathbf{u}_n|^2 \rangle = \langle u^2 \rangle$

and the temperature dependence is given by a B -factor,

$$B_T = \frac{8\pi^2}{3} \langle u^2 \rangle.$$

The B -factor is a function of the temperature and empirically determined Debye temperature Θ of the material [112,113].

4.1.3: Dynamical scattering from a perfect crystal

Dynamical diffraction theory is a more rigorous mathematical treatment of the interaction between X-rays and matter which takes multiple scattering events into account. Herein is a summary of Ewald-von Laue's approach to solving dynamical scattering and impact on the equations that govern X-ray interactions with matter, the details of the solution are described initially in Batterman and Cole [114]. To reproduce the fine details of X-ray interaction with a perfect crystal, Ewald-von Laue solved Maxwell's equations for continuous electromagnetic waves propagating in medium with a triply periodic complex relative permittivity. Using appropriate boundary conditions, the solutions are wave fields that can be represented as Bloch waves.

The crystal through which the X-rays are propagating can be thought of as a periodic potential. This potential is described with a relative permittivity ϵ_r , which is a complex quantity

which describes how the polarization density \mathbf{P} is influenced by an electric field \mathbf{E} within the material. The polarization density $\mathbf{P} = \rho(\mathbf{r})\mathbf{d}$ describes how the charge density $\rho(\mathbf{r})$ is displaced by a distance \mathbf{d} . The permittivity is a measure of how resistance the material is to charge displacement described by $\mathbf{P} = \epsilon_0(\epsilon_r - 1)\mathbf{E}$, where ϵ_0 is the permittivity of free space and $\epsilon_r - 1 = \chi_e$ the electric susceptibility. For the case of X-rays interacting with matter, this susceptibility can be represented as

$$\chi_e(\mathbf{r}) = \frac{\rho(\mathbf{r})\mathbf{d}}{\epsilon_0\mathbf{E}} = -\frac{\rho(\mathbf{r})r_e\lambda^2}{\pi}, \quad (4.12)$$

considering a sinusoidal field of amplitude E_0 [114]. An inverse Fourier transform of the structure factor results in the charge density $\rho(\mathbf{r})$ represented as a sum of structure factors in reciprocal space,

$$\rho(\mathbf{r}, \lambda) = \frac{1}{V_{\text{u.c.}}} \sum_{\mathbf{G}_H} F(\mathbf{G}_H, \lambda) e^{-i\mathbf{G}_H \cdot \mathbf{r}}, \quad (4.13)$$

thus allowing the medium to be also expressed as a sum of structure factors,

$$\epsilon_r(\mathbf{r}) = 1 - \Gamma \sum_{\mathbf{G}_H} F(\mathbf{G}_H, \lambda) e^{-i\mathbf{G}_H \cdot \mathbf{r}}, \quad (4.14)$$

with a scaling factor $\Gamma = r_e\lambda^2/\pi V_{\text{u.c.}}$, where $V_{\text{u.c.}}$ is the volume of the unit cell. The assumed solution to Maxwell's equations are planewaves described by Bloch functions with wavevector \mathbf{G}_H and amplitude as a Fourier series. Maxwell's equations,

$$\nabla \times \mathbf{E} = -\frac{\partial \mathbf{B}}{\partial t} \quad \nabla \times \mathbf{B} = \epsilon_0\epsilon_r \frac{\partial \mathbf{E}}{\partial t}, \quad (4.15)$$

can be solved using a choice of appropriate boundary conditions, the exact solution is described in detail elsewhere for a perfect crystal [114] and for slightly distorted crystals [115,116], both of which require appropriate choice of boundary conditions. Namely, the planewave solution must

be continuous inside and outside the crystal surface, this boundary condition is satisfied when for every point on the surface (\mathbf{r}_s), such that

$$\sum_i \mathbf{E}_i e^{-2\pi i \mathbf{k}_i \cdot \mathbf{r}_s} = \sum_f \mathbf{E}_f e^{-2\pi i \mathbf{k}_f \cdot \mathbf{r}_s} \quad (4.16)$$

for physically coupled waves at the Bragg condition, $\mathbf{G}_H = \mathbf{k}_H - \mathbf{k}_0$. When Maxwell's equations are solved with these constraints, the solution is a standing wave with energy dependent amplitude and phase. It is common to describe the response of the standing wave solution using the normalized parameter,

$$\eta = \frac{-2b \left(\frac{\Delta E}{E_\gamma} \right) \sin^2(\theta_B) + \frac{1}{2} \Gamma F_0 (1 - b)}{\Gamma |P| |b|^{\frac{1}{2}} \sqrt{F_H F_{\bar{H}}}}, \quad (4.17)$$

which contains an offset from the geometrical Bragg energy $\Delta E = E_\gamma - E_B$. The equation for η can be similarly defined for an angular offset $\Delta\theta = \theta - \theta_B$ from the Bragg angle [114]. For convenience, $F(\mathbf{G}_H, \lambda)$ has been separated into real $F'_H = f^0(\mathbf{G}_H) + f'(\lambda)$ and imaginary $F''_H = if''(\lambda)$ components such that $F_H = F'_H + iF''_H$. The imaginary component of the $H = 000$ term of the Fourier series $iF''_0(\lambda)$ is related to the linear absorption coefficient by $\mu_0 = 2\pi/\lambda \Gamma F''_0$. Simply put, η is a complex quantity $\eta' + i\eta''$ multiplied by ΔE . The amplitude of the solution can be understood as the ratio between incident and reflected beams,

$$\frac{E_H}{E_0} = -\frac{|P|}{P} |b|^{\frac{1}{2}} \left(\eta \pm \sqrt{\eta^2 - 1} \right) \sqrt{\frac{F_H}{F_{\bar{H}}}}, \quad (4.18)$$

where the asymmetry factor $b = \gamma_0/\gamma_H$ is the ratio of the direction cosines of the incident γ_0 and reflected γ_H beams relative to the sample surface normal. Note that in Bragg (i.e. reflection) geometry b is negative and for Laue (i.e. transmission) geometry b is positive. A useful substitution

for η is $\frac{1}{2}(e^{iv} + e^{-iv}) = \cosh v$ to such that $(\eta \pm \sqrt{\eta^2 - 1}) = \pm e^{\pm iv}$, which allows eq. 4.18 to be recast in terms of phase,

$$\frac{E_H}{E_0} = \mp |b|^{\frac{1}{2}} e^{\pm iv} \sqrt{\frac{F_H}{F_{\bar{H}}}}, \quad (4.19)$$

where the quantity v is proportional to the relative phase between of the total field generated at the Bragg condition. For a symmetric Bragg reflection crystal $b = -1$ and $F_H = F_{\bar{H}}$. The phase of \mathbf{E}_H versus \mathbf{E}_0 shifts by π -radians when going from $\eta' = 1$ (α branch) to $\eta' = -1$ (β branch), which mark the beginning and ending of the total Bragg reflection. The range of the total Bragg reflection can be calculated from the different in energy at the α branch and the β branch, known as the Darwin width ω_E of the reflection where

$$\omega_E = \Delta E_\alpha - \Delta E_\beta = \frac{E_\gamma \Gamma |P| \sqrt{F'_H F'_{\bar{H}} + F_0''^2 - F''_H F''_{\bar{H}}}}{\sqrt{|b|} \sin^2(\theta_B)}, \quad (4.20)$$

the center of the reflection at $\eta' = 0$ is offset from the kinematical approximation by

$$\Delta E_0 = \frac{\Gamma F_0 E_\gamma}{2 \sin^2(\theta_B)} \frac{1 + |b|}{2|b|}. \quad (4.21)$$

4.1.4: X-ray photoexcitation

The excitation probability of an electron from initial ground state $|i\rangle$ to the final unbound state $|f\rangle$ is expressed by the matrix element

$$M_{fi} = E_\gamma \langle f | (-i\hbar \nabla \cdot \hat{\boldsymbol{\epsilon}}) e^{-i\mathbf{k}\cdot\mathbf{r}} | i \rangle, \quad (4.22)$$

for the absorption of a photon plane wave with electric field $\hat{\boldsymbol{\epsilon}} E_\gamma$ and wavevector \mathbf{k} by an atom. The quantity $-i\hbar \nabla$ is the momentum operator. The differential absorption cross section of the ejected photoelectron with wavevector \mathbf{k}^p can be written as

$$\frac{d\sigma(\theta^P, \phi^P)}{d\Omega} \propto |M_{fi}|^2,$$

from which the total cross section is calculated by integrating over the whole spatial angle Ω , with spherical angles θ^P and ϕ^P relative to the incident beam polarization.

A multipole approximation of the matrix element M_{fi} is given by a Taylor series expansion of the retardation factor $e^{-i\mathbf{k}\cdot\mathbf{r}} = 1 - i\mathbf{k}\cdot\mathbf{r} - \frac{1}{2}(\mathbf{k}\cdot\mathbf{r})^2 + \dots$, each term adds higher order electromagnetic transitions. The first term (M_{fi}^I) gives the electric dipole; the second term (M_{fi}^{II}) gives the electric quadrupole and magnetic dipole. For the dipole-quadrupole 2nd approximation, the differential absorption is given by

$$\frac{d\sigma(\theta^P, \phi^P)}{d\Omega} \propto |M_{fi}^I|^2 - 2\Re[M_{fi}^I{}^* M_{fi}^{II}(\mathbf{k})]. \quad (4.23)$$

the components of the second term are small compared to the first, so the $|M_{fi}^{II}|^2$ terms are neglected. This approximation is valid when the X-ray wavelength is considerably larger than the electron-bound state orbital. For the case of a single X-ray beam with linearly polarized photons, the general expression for differential absorption can be parameterized as

$$\frac{d\sigma}{d\Omega} = \frac{\sigma}{4\pi} \left\{ 1 + \frac{\beta}{2} [3(\hat{\mathbf{e}} \cdot \hat{\mathbf{k}}^P)^2 - 1] + [\delta + \gamma(\hat{\mathbf{e}} \cdot \hat{\mathbf{k}}^P)^2] (\hat{\mathbf{k}} \cdot \hat{\mathbf{k}}^P) \right\}, \quad (4.24)$$

where β is the asymmetry factor from $|M_{fi}^I|^2$; γ and δ are asymmetry factors from $2\Re[M_{fi}^I{}^* M_{fi}^{II}(\mathbf{k})]$. These asymmetry factors depend on the atom, sub-shell, and photon energy and can be found from simulated tables. The $\hat{\mathbf{k}} \cdot \hat{\mathbf{k}}^P$ term introduces a forward and backward asymmetry of photoemission depending on the direction of the incident photon. This non-dipolar effect is significant at lower X-ray energies, particularly at the normal incidence reflection geometry [117-119].

4.2: X-ray standing wave

X-ray spectroscopy imparts chemical specificity to Ångström-scale X-ray diffraction measurements. Specifically, X-ray photoelectron spectroscopy (XPS) enhanced with X-ray standing waves (XSW) has been instrumental in resolving the interface structure of a myriad of 2D materials on single-crystal surfaces [14,120,121]. With this capability, it is possible to distinguish atoms on the surface from those in the bulk as well as the degree of bonding across a 2D material, owing to the unique chemical signatures of these species seen by XPS and the distinct vertical separation seen by XSW. For additional information, the reader is directed to reviews by Woodruff [122] and Zegenhagen [123].

The XSW technique uses two coherently coupled X-ray plane waves, in this case generated using Bragg diffraction, to produce specially resolved standing wave to periodically enhance X-ray spectroscopic signals. The technique is used to determine the position of native [124], dopant [125,126], and surface atoms [124,127] with chemical sensitivity in/on a perfect single-crystal. Critically XSW can be used to determine the precise spacing between chemical species, which in a 2D structure, is indicative of the strength of interactions between layers.

4.2.1: X-ray excited photoelectron yield

The standing wave field comes from the interference of the incident plane wave,

$$\mathbf{E}_0(\mathbf{r}, t) = \hat{\mathbf{e}}_0 E_0 e^{-i[\mathbf{k}_0 \cdot \mathbf{r} - \omega t]}, \quad (4.25)$$

and diffracted plane wave,

$$\mathbf{E}_H(\mathbf{r}, t) = \hat{\mathbf{e}}_H E_H e^{-i[\mathbf{k}_H \cdot \mathbf{r} - \omega t]}, \quad (4.26)$$

in a perfect single-crystal with the same time dependent frequency ωt . The standing wave field $\mathbf{E}^T(\mathbf{r}, t)$ is sum of these coherent plane waves with a periodicity given by $\mathbf{d}_H = 2\pi/\mathbf{k}_H - \mathbf{k}_0 = 2\pi/\mathbf{q}$. This sum of the complex e-field amplitudes is

$$\mathbf{E}^T = [\hat{\mathbf{e}}_0 E_0 e^{-i \mathbf{k}_0 \cdot \mathbf{r}} + \hat{\mathbf{e}}_H E_H e^{-i \mathbf{k}_H \cdot \mathbf{r}}] e^{i\omega t}, \quad (4.27)$$

which describes the total field of the standing wave. At the Bragg condition, $\mathbf{q} = \mathbf{G}_H$, the normalized intensity of the standing wave $I(\mathbf{r}, E) = |\mathbf{E}^T(\mathbf{r}, t)|^2/E_0^2$ is given by

$$\frac{|\mathbf{E}^T|^2}{E_0^2} = 1 + \left| \frac{E_H}{E_0} \right|^2 + 2P \left| \frac{E_H}{E_0} \right| \Re \left\{ e^{-i[\mathbf{G}_H \cdot \mathbf{r} - v_{E_\gamma}]} \right\}, \quad (4.28)$$

where the energy dependent standing wave phase v_{E_γ} is defined in eq. 4.19.

For standing wave excited photoemission, the position vector of the excited electron \mathbf{r} is given by the displacement of the excited electron \mathbf{r}^e plus the position of the center of the atom \mathbf{r}^a . The total photoexcitation matrix element is calculated using superposition of the incident and reflected planewave by substituting eq. 4.27 into eq. 4.22, from which the matrix element

$$M_{fi}^T(\mathbf{r}) = E_0 \langle f | (-i\hbar\nabla \cdot \hat{\mathbf{e}}_0) e^{-i\mathbf{k}_0 \cdot \mathbf{r}} | i \rangle + E_H \langle f | (-i\hbar\nabla \cdot \hat{\mathbf{e}}_H) e^{-i\mathbf{k}_H \cdot \mathbf{r}} | i \rangle, \quad (4.29)$$

can be expressed as

$$M_{fi}^T = E_0 e^{-i\mathbf{k}_0 \cdot \mathbf{r}^a} \left[M_{fi}(\mathbf{k}_0, \mathbf{r}^e) + \frac{E_H}{E_0} e^{-i\mathbf{G}_H \cdot \mathbf{r}^a} M_{fi}(\mathbf{k}_H, \mathbf{r}^e) \right], \quad (4.30)$$

by substituting $\mathbf{r} = \mathbf{r}^a + \mathbf{r}^e$. For a given polarization state, the normalized photoelectron cross section $d\sigma/d\Omega \propto |M_{fi}^T(\mathbf{r})|^2$ which has the form of the standing wave intensity (eq. 4.28) where

$$\frac{|M_{fi}^T|^2}{E_0^2} = S_{00} + S_{HH} \left| \frac{E_H}{E_0} \right|^2 + 2 \left| \frac{E_H}{E_0} \right| \Re \left\{ S_{0H} e^{-i[\mathbf{G}_H \cdot \mathbf{r}^a - v_{E_\gamma}]} \right\}, \quad (4.31)$$

but with the addition of a set of angular emission parameters $S_{00} = |M_{fi}(\mathbf{k}_0, \mathbf{r}^e)|^2$, $S_{HH} = |M_{fi}(\mathbf{k}_H, \mathbf{r}^e)|^2$, and $S_{0H} = M_{fi}(\mathbf{k}_0, \mathbf{r}^e)^* M_{fi}(\mathbf{k}_H, \mathbf{r}^e)$. These modifications to the photoelectron yield are from the photoelectron cross sections of the direct, scattered, and interfering X-ray plane waves. These terms add the dipolar and quadrupolar corrections to the photoemission process. The S_{00} and S_{HH} are generally real, while the S_{0H} is complex and results in a phase shift $\psi = |S_{0H}|e^\psi$. The generalize yield function $Y_H^T \propto |M_{fi}^T(\mathbf{r})|^2$ and is commonly written as

$$Y_H^T = 1 + S_R R + 2|S_I| \sqrt{R} f_H \cos \left[\psi - 2\pi P_H - \nu_{E_\gamma} \right] \quad (4.32)$$

by defining

$$R = \left| \frac{E_H}{E_0} \right|^2, \quad S_R = \frac{S_{HH}}{S_{00}}, \quad S_I = \frac{S_{0H}}{S_{00}}$$

and by introducing the coherent fraction f_H and coherent position P_H defined as

$$f_H e^{2\pi i P_H} = \int \rho(\mathbf{r}) e^{-i\mathbf{G}_H \cdot \mathbf{r}} d\mathbf{r} \quad (4.33)$$

which are the amplitude and phase of the hkl Fourier component of the normalized atomic distribution. The determination of the angular emission terms, have been calculated from the matrix elements under the dipole quadrupole approximation of the photoemission cross section [128]. The angular emission parameters become

$$\begin{aligned} S_{00} &= \frac{3\sigma_D}{4\pi} [\hat{\boldsymbol{\epsilon}}_0 \cdot \hat{\mathbf{k}}^p]^2 [1 + \gamma'(\hat{\mathbf{k}}_0 \cdot \hat{\mathbf{k}}^p)] \\ S_{HH} &= \frac{3\sigma_D}{4\pi} [\hat{\boldsymbol{\epsilon}}_H \cdot \hat{\mathbf{k}}^p]^2 [1 + \gamma'(\hat{\mathbf{k}}_H \cdot \hat{\mathbf{k}}^p)] \\ S_{0H} &= \frac{3\sigma_D}{4\pi} [\hat{\boldsymbol{\epsilon}}_0 \cdot \hat{\mathbf{k}}^p][\hat{\boldsymbol{\epsilon}}_H \cdot \hat{\mathbf{k}}^p] \left[1 + \frac{\gamma(\hat{\mathbf{k}}_0 \cdot \hat{\mathbf{k}}^p) + \gamma^*(\hat{\mathbf{k}}_H \cdot \hat{\mathbf{k}}^p)}{2} \right], \end{aligned} \quad (4.34)$$

where σ_D is the angularly integrated dipole cross section of photoelectron excitation, $\hat{\mathbf{k}}^p$ is the emitted photon electron wave, and the complex parameter $\gamma = \gamma' + i\gamma'' = \gamma_0 e^{i\Delta}$. The parameter $\Delta = \delta_d - \delta_p$ is the difference partial phase shifts of the p- and d-state of the photoelectron, δ_d and δ_p can be determined from relativistic *ab initio* calculations [129,130].

4.2.2: Normal incidence Geometry

XSW performed at typical hard X-ray energies (e.g. Cu K α , 8.03 keV) yield angular Darwin widths of typically 10 – 50 microradians. To reach this theoretical width requires single-crystal samples with mosaicity as a small fraction of Darwin width. At these energies, this restricts the XSW measurement to highly perfect single-crystals (e.g. Ge, Si, a-TiO₂,).

Using $2\theta = 180^\circ$ geometry minimizes the gradient of Bragg's law $d\lambda/d\theta$ and produces rocking curves with Darwin widths on the order of milliradians. This expanded Darwin width allows elemental metals and other more imperfect single-crystals to be used to generate standing waves. This geometry is referred to as both normal incidence XSW (NIXSW) and back-reflection XSW (BRXSW). As is evident from Bragg's law, achieving the normal incidence geometry requires calculating an energy for a given substrate and reflection. The rocking curve is scanned in energy rather than angle to maintain the $\hat{\mathbf{k}}_0 \approx -\hat{\mathbf{k}}_H$ condition. Maintaining this geometry allows considerable simplification of the angular emission parameters, eq. 4.34. For the case of an s \rightarrow p transition with σ -polarization and the spectrometer perpendicular to $\hat{\mathbf{k}}_0 + \hat{\mathbf{k}}_H$, the non-dipolar effects angular photoemission cross section terms, eq. 4.32, can be simplified to

$$S_R = \frac{1 + \gamma' \cos \theta^p \sin \theta}{1 - \gamma' \cos \theta^p \sin \theta}, \quad S_I = \frac{1 + i\gamma'' \cos \theta^p \sin \theta}{1 - \gamma' \cos \theta^p \sin \theta}, \quad (4.35)$$

where $\theta^p = \mathbf{G}_H \cdot \hat{\mathbf{k}}^p$. In the NIXSW geometry, $\sin \theta = 1$ and the equations further simplify to

$$S_R = \frac{1 + \gamma' \cos \theta^p}{1 - \gamma' \cos \theta^p}, \quad S_I = \frac{1}{1 - \gamma' \cos \theta^p}. \quad (4.36)$$

A similar simplification can be performed for a $p \rightarrow d$ transition in the same geometry [122].

For the case of a slight tilt angle $2\theta \neq 180^\circ$ the for NIXSW geometry, which is common practice at beamlines, specifically I09 at Diamond Light Source and ID32 at European Synchrotron Facility. Under these geometric conditions, the determination of S_R and S_I require a slight correction because of the deviation from σ -polarization and $\sin \theta \neq 1$, the procedure is fully described by Ref. [119].

4.2.3: Yield fitting procedure

Recall eq. 4.32, the angular emission parameters, S_R , S_I , and ψ are material dependent parameters. The spectroscopy yield Y_H^T and reflected X-ray intensity R are measured experimentally as a function of \mathcal{E} . Therefore, f_H and P_H are model independent fitting parameters which relate the measure photoelectron yield to the Darwin reflectivity. The amplitude f_H and phase P_H bounded between 0 and 1, describe fully every possible distribution of spectroscopic species $\rho(\mathbf{r})$ within the period of the standing wave.

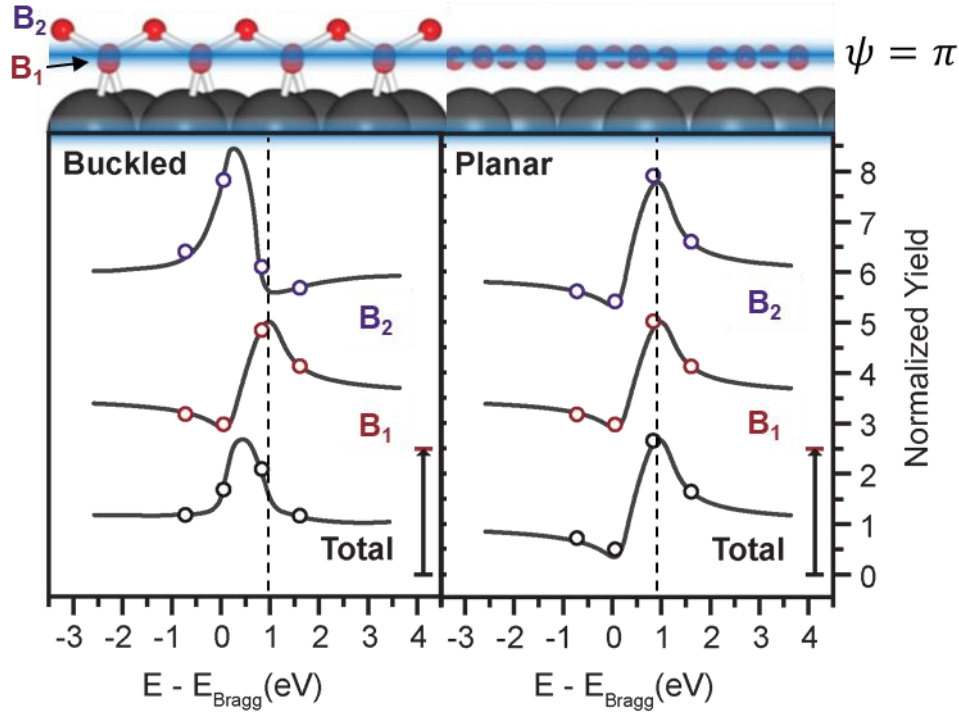


Figure 4.1: Simulated X-ray standing wave measurement of borophene (top) schematic showing position of boron atoms (red) relative to Ag(111) single-crystal (grey) and the standing wave (blue). (bottom) Simulated yield for coherent positions P_H of distinct boron atoms buckled (left) and planar (right) borophene assuming a coherent fraction $f_H = 1$ and where the plane defined by the center of Ag atoms gives $P_H = 0 = 1$. The dotted line indicates the energy where the phase of the standing wave, $\psi = \pi$. (Source: adapted from Ref. [103])

The coherent fraction is a measure of the distribution of $\rho(\mathbf{r})$, while the coherent position is a measure of the average position of the distribution. To more precisely interpret atomic structure from measured coherent fractions and positions, solve eq. 4.33 along the $H = hkl$ direction of the standing wave for atoms with distribution $\rho(\mathbf{r})$. For the simple case of a distribution of atomic species (s),

$$\mathcal{F}_H^s = f_H^N e^{2\pi i P_H^N} = \frac{1}{C^n} \sum_{n=1}^N c^n e^{2\pi i P_H^n}, \quad (4.37)$$

where the distribution is comprised of N sites with coherent positions P_H^n and a occupation fraction $c^n < 1$ of each site. The solution to eq. 4.37 can be found by summing complex vectors with magnitude f_H^n and phase angle $2\pi P_H^n$ in the complex plane. Simulated XSW yields for proposed atomic configurations of borophene on Ag(111) are shown in Figure 4.1.

XSW measurements taken at a set of at least three linearly independent $H = hkl$ can be used to determine the location of atoms relative to the 3D bulk single-crystal [131,132]. Where by Fourier reconstruction methods [133], each f_H and P_H contributed a Fourier component along which interfere to reveal the atomic positions of the measured atoms relative to the bulk single-crystal unit cell.

4.3: Crystal Truncation Rod

The crystal truncation technique uses interference between adlayers and a perfect single-crystal substrate to solve the structure of the interface. These interfaces often play a pivotal role in understanding the mechanisms behind epitaxial registry of monolayers on single-crystals. This measurement was the first direct structural measurement of covalent-like bonding present at the EG/SiC [134] interface and revealed the formation of a wetting $\text{Ag}_x\text{Si}_{1-x}$ alloy layer at the Ag/Si(111) interface which seeded Ag(111) epitaxy [135]. The CTR technique helps distinguish structures with many chemically similar layers of material.

4.3.1: Kinematical Scattering from a surface

Kinematical scattering for an infinite bulk crystal results in a structure factor F with scattering occurring at the $\mathbf{G}_H = \mathbf{q} = \mathbf{k}_H - \mathbf{k}_0$ Laue condition. The cleavage of the perfect crystal reduces the lattice to a finite size along the surface normal of the truncated crystal, which in reciprocal lattice stretches the points \mathbf{G}_H along the surface normal resulting in the crystal truncation

rods. The truncation of single-crystal surface is mathematically represented by the lattice sum along \mathbf{c} ,

$$F^{\text{CTR}}(\mathbf{q}) = F^{hk}(\mathbf{q}) \sum_{n=-\infty}^0 e^{i\mathbf{q}\cdot[n\mathbf{c}]} e^{-n\beta} = F^{hk}(\mathbf{q}) \frac{1}{1 - e^{i\mathbf{q}\cdot\mathbf{c} - \beta}}, \quad (4.38)$$

where the absorption parameter is given by $\beta = \mu/\sin\theta$ for one atomic plane along the surface normal. $F^{\text{CTR}}(\mathbf{q})$ depends on the precise truncation of the crystal surface, which then modulated by interference with surface adlayers. For an adlayer with in-plane structure factor $F^{hk}(\mathbf{q})$ and which deviates from bulk plane-spacing by a fraction z_0 ,

$$F^{\text{T}}(\mathbf{q}) = F^{\text{CTR}}(\mathbf{q}) + F^{hk}(\mathbf{q})e^{i\mathbf{q}\cdot[(1+z_0)\mathbf{c}] - \beta}. \quad (4.39)$$

Recalling the derivations of the kinematical approximation, the measured intensity of such a surface is

$$I(\mathbf{q}) = F^{\text{T}}(\mathbf{q})e^{-\frac{1}{2}\mathbf{q}^2\cdot\langle\mathbf{u}_n^2\rangle}. \quad (4.40)$$

4.3.2: Surface structure

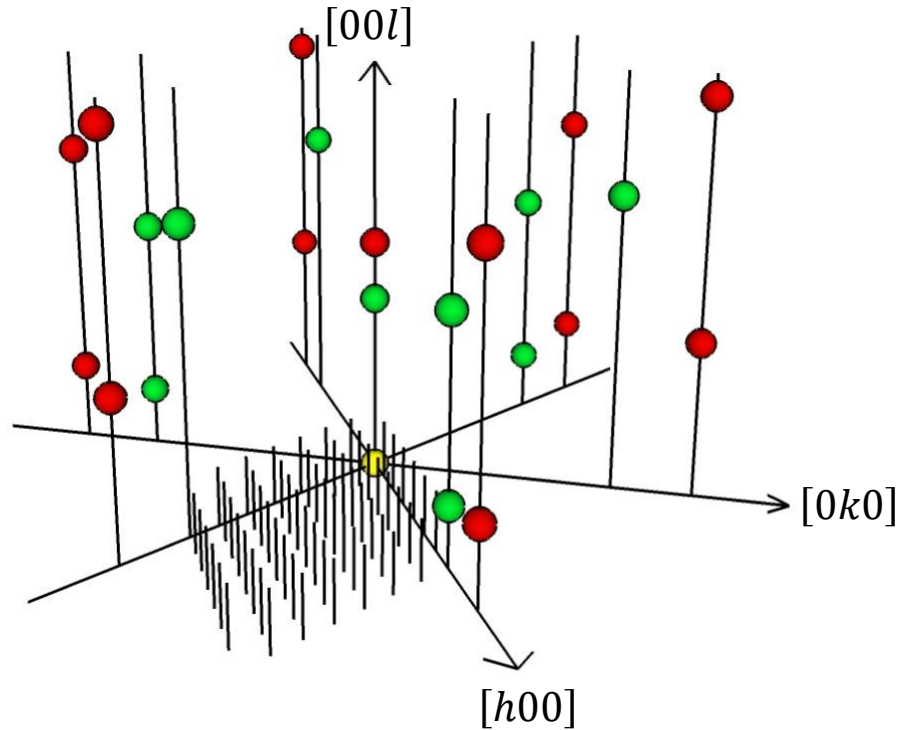


Figure 4.2: Schematic of crystal truncation rod of Ag/Si(111) 7×7 reconstruction with bulk. Bragg peaks of Ag(111) and Si(111) indicated by red and green circles respectively. Truncation rods for indicated by black lines with long lines for bulk Bragg peaks of Ag and Si and short lines for 7×7 reconstruction. (Source: adapted from Ref. [135])

When performing the crystal truncation rod measurement in Bragg geometry normal to the surface planes, the vector quantities \mathbf{c} and \mathbf{q} are projected onto the surface normal vector and given by the scalar values c and q_z . The normalized intensity is then

$$R(q_z) = \frac{I(q_z)}{I_0} = \left(\frac{4\pi r_e}{q_z a_{\text{u.c.}}} \right)^2 |F^T(q_z)|^2 |B(q_z)|^2, \quad (4.41)$$

where the classical electron radius (r_e) and unit cell area ($a_{\text{u.c.}}$) are constant, with the dependent parameter being the momentum transfer vector (q_z). The Robinson roughness factor [136],

$$|B(q_z)|^2 = \frac{1 - \beta_R}{1 + \beta_R^2 - 2\beta_R \cos(q_z c)}, \quad 0 \leq \beta_R \leq 1 \quad (4.42)$$

accounts for the impact of inhomogeneity on the surface (e.g. step edges) on the measured specular reflectivity. This measured reflectivity can be rewritten using a piecewise function to describe F^T ,

$$R(q_z) = \left(\frac{4\pi r_e}{q_z a_{u.c.}} \right)^2 |F^{u.c.}(q_z)F^{CTR}(q_z) + F^s(q_z) + F^v(q_z)|^2 |B(q_z)|^2, \quad (4.43)$$

where contributions from the bulk crystal substrate, the topmost bulk-like crystal planes, and overlayers are given by $F^{u.c.}$, F^s , and F^v , respectively. These are each described with a discrete or infinite sum of m lattice planes,

$$F(q_z) = \sum_m \Theta_m f_m^a(q_z) e^{iq_z z_m} e^{-\frac{1}{2}(q_z u_m)^2} \quad (4.44)$$

measured normal to the crystal surface, where each lattice plane is calculated from the average height relative to the surface, z_m , fractional monolayer occupancy, Θ_m , and distribution width, u_m . The maximum achievable real-space resolution of the Fourier transform is described by the Nyquist-Shannon Theorem. This value, given by $1/q_{max}$, was added in quadrature to u .

The methodology to collect CTR reflectivity data using a hybrid photon-counting (HPC) has been written by Fenter [137,138]. Using model-dependent statistical analysis, the terms z , Θ , and u are refined until the calculated reflectivity matches the experimentally measured reflectivity. The modeling tool used for this thesis work is least-squares analysis by implementing the Fienup algorithm [139] to generate electron density profiles.

4.4: Grazing incidence X-ray diffraction

Grazing incidence X-ray diffraction (GIXD) diffraction is a powerful tool for determining the size, shape, and orientation of nanostructures on surfaces. Through the generation of an evanescent wave on the surface, X-rays intensity decreases exponentially with depth, allotting X-ray techniques with heightened surface sensitivity. These techniques are commonly applied to 2D materials to achieve measurable diffracted intensity.

4.4.1: Intensity and grazing angles

GIXD gains surface sensitivity the from low penetration into bulk and enhanced electric field at surface achieved near the total external reflection condition. The refractive index of X-rays $n = 1 - \delta - i\beta$, being slightly less than unity, leads to the total external reflection of an incident X-ray beam at angles α_i below the critical angle $\alpha_c < \sqrt{2\delta}$. Though all X-rays are reflected below α_c , the X-ray E-field penetrates the surface with an exponentially decaying function known as the evanescent wave. The depth of penetration is given by

$$Z = \frac{\lambda}{2\sqrt{2}\pi \left(\sqrt{\alpha_i^2 - \alpha_c^2 + 4\beta^2} + \alpha_c^2 - \alpha_i^2 \right)^{\frac{1}{2}}}. \quad (4.45)$$

A second consequence of the evanescent wave effect is the factor of four increase in E-field intensity at $\alpha_i = \alpha_c$. This enhanced E-field effect enhances in-plane scattering from surface structures, making it an optimal geometry for 2D crystal structure determination. Consider a crystal substrate with in-plane vectors h and k with the surface normal l . The structure factor $F(q)$ is smeared along the surface normal l , so the determination of integrated intensity requires integrating the entire rod. A practical approach is use discrete portion of the rod $q_z = 0$ to acquire planar intensity cross sections. The derivation of the in-plane structure factor F^{hk} follows the derivation of kinematical diffraction theory with $l = 0$,

$$F^{hk}(q) = f^a(q) \left| \sum_{m=1}^M e^{i(ha^* + kb^*) \cdot r_m} e^{[lq \cdot u_m]} \right|^2. \quad (4.46)$$

Extracting the structure factor F^{hk} from scattered intensity requires additional factors to account for the 2D experimental geometry and deviations from ideal kinematical scattering theory. The Lorentz polarization factor $L_P = P_H / \sin 2\theta_B$ accounts for the polarization of the incident beam

as observed at the Bragg reflection and the Lorentz factor $1/\sin 2\theta_B$ accounts for the reciprocal space width of different reflections. When accounted for these corrections, the in-plane scattering intensity is given by,

$$I_H = I_0 \frac{V|F_H|^2}{v} L_P. \quad (4.47)$$

Though notably, for 2D detectors, the Lorentz factor is eliminated through integration of the full diffraction spot intensity.

4.4.2: GISAXS/GIWAXS

Grazing incidence X-ray scattering (GIXS) is a useful tool to probe the in-plane structure at multiple length scales. Grazing incidence small-angle (GISAXS) and wide-angle (GIWAXS) X-ray scattering are special geometries where multiple exit vectors \mathbf{k}_f are collected over a large-area from an incident wavevector \mathbf{k}_i . By modulating the distance between GISAXS is typically measured with the detector placed a few meters away from the sample and probes in the $\mathbf{q} \sim 0.1 \text{ \AA}^{-1}$ regime. GIWAXS is performed with the detector only at 10 cm from the sample to access $\mathbf{q} \sim 10 \text{ \AA}^{-1}$, which probes atomic plane spacing.

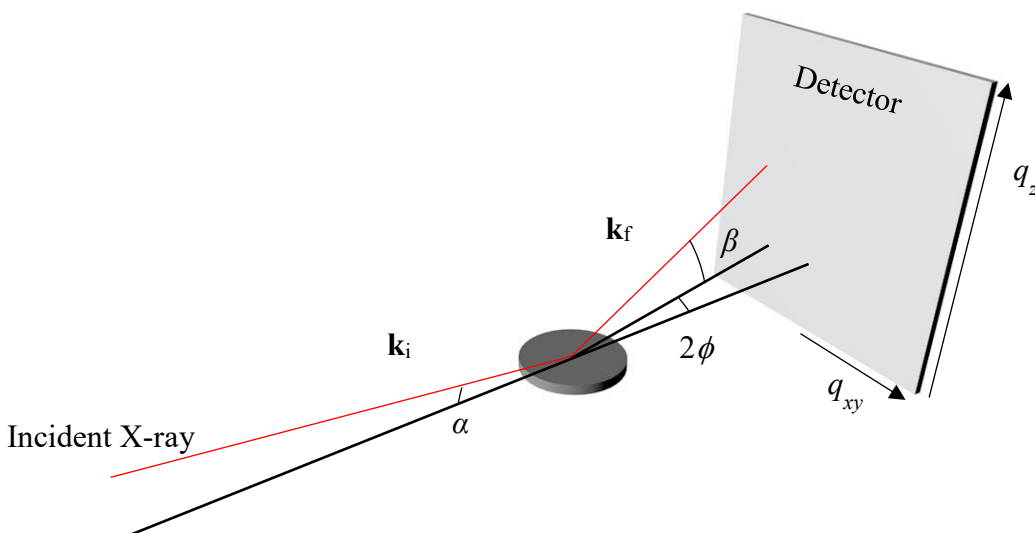


Figure 4.3: GIXS geometric setup showing incident x-ray with vector \mathbf{k}_i , scattered vector \mathbf{k}_f , incident angle α , scattered vertical angle β and horizontal angle 2ϕ .

4.5: X-ray Photoelectron Spectroscopy

X-ray Photoelectron Spectroscopy (XPS) is a highly surface sensitive tool for non-destructive chemical state analysis of a surface at parts per thousand atomic concentrations. [109]

4.5.1: X-ray Photoelectron Spectroscopy

X-ray Photoelectron spectroscopy (XPS) is typically performed under ultra-high vacuum ($< 10^{-7}$ mbar) to prevent air absorption of emitted photoelectrons with nanometer mean free paths in ambient. Though at this time, there are ongoing efforts to develop ambient-pressure XPS to study UHV-incompatible systems. Energy-dispersive spectrometers measure the quantity of ejected photoelectrons as a function of E_k . Electron optics within the spectrometer allow electrons in a finite E_k window (pass energy) to reach the photoelectron detector, which is scanned over a user-defined energy region. E_k is commonly converted to E_b and put on a reverse linear scale. A kinetic energy calibration is performed by setting the measured spectra to a known parameter (e.g. avaricious carbon peak or fermi energy).

4.5.2: Photoemission Physics

Electrons in a material occupy discrete energy states described by the dispersion relation for which the interaction between wavevector \mathbf{q}_v of the electron and the material results in characteristics binding energies (E_b). Photoelectric absorption can occur in a material when an incident X-ray has an energy (E_γ) which exceeds the minimum energy required to excite the most

weakly bonded electron into vacuum, this is the work function (Φ_A) of the material. As E_γ increases, tightly bonded core-shell electrons are excited into vacuum with kinetic energy

$$E_k = \frac{\hbar^2 \mathbf{q}_v^2}{2m} = E_\gamma - (E_b + \Phi_A). \quad (4.48)$$

This approach enables the determination of E_b which is sufficient to deduce the chemical composition of atoms at a surface. This is the basis of X-ray photoelectron spectroscopy (XPS).

Local chemistry induces subtle changes in electron binding energy, thus XPS is commonly used as a means to distinguish different chemical states [140]. An example of this is spin-orbit interactions, which result in doublet peak (e.g. $3d_{3/2}$ and $3d_{5/2}$) for all orbitals with distinct angular momentum (i.e. not s). Core-level shifts also reflect the valence state of the electron, which is most commonly analyzed through comparison to a compound specific elemental library [140]. Core-level shifts can also reflect changes to the electronic structure, including band-bending [141] and doping [82,142]. The width of the measured peak is defined by the full width half-maximum ΔE , and is a convolution of chemical-state effects with the intrinsic energy width Γ of the peak, the X-ray line width, and the analyzer resolution. The intrinsic peak broadening is an example of the uncertainty principle in time-energy space, $\Gamma = \frac{h}{\tau}$ where h is Planck's constant and τ is the core-hole lifetime [143]. The depletion of electrons near the Fermi energy also leads to apparent peak broadening from core-shifting due to increased nuclear charge. This effect is evident from an asymmetric broadening of the low KE tail of the peak [144].

4.5.3: Composition Analysis

Analysis of the XPS peak shape and intensities requires a quantum mechanical treatment to extract quantitative chemical state composition within the measured film. A number of simplified models for the quantum mechanical description of XPS to enable extracting quantitative

information. In practice, determining the photoabsorption coefficients is done either with experimentally verified model calculations. Scofield has calculated photoionization cross sections for neutral atoms ranging from 1 keV to 1500 keV [145].

The substrate—overlayer model [146-148] describe the influence of thin ($< 29 \text{ \AA}$) overlayers on measured XPS peak intensity. The s-o model is based upon effective attenuation length (EAL) calculations,

$$EAL = - \left\{ \cos \alpha \frac{d \ln[(z, \alpha)]}{dz} \right\}, \quad (4.49)$$

which provides a measurement of the probability of inelastic scattering for detected photoelectrons as a function of depth z and electron emission angle α . The precise calculation of EAL differs between models and is the primary source of uncertainty. Nonetheless, reasonable estimates of the overlayer thickness t can be determined by comparing these theoretically predicated EALSs to their experimentally derived values.

EAL theories by Powell and Tanuma [149,150] and Gries [151] have been constructed into a comprehensive NIST database [152] and companion software package to calculate EALS using predictive models for electron kinetic energies ranging from 50 eV to 2,000 eV for a wide range of elements and compounds. The NIST database calculates the inelastic mean free path [153] (IMFP) and transport mean free path [154,155] (TMFP) which provide the length at which intensity is reduced to $1/e$ due to inelastic and elastic scattering of photoelectrons. For a given material, the IMFP has an electron kinetic energy dependence described by the Bethe equation[153]

$$\lambda_i = \frac{E}{E_p \left[\beta \ln(\gamma E) - \left(\frac{C}{E} \right) + \left(\frac{D}{E^2} \right) \right]} \quad (4.50)$$

where E is the electron energy and E_p is the bulk plasmon energy. The parameters β , γ , C , and D depend on the valence, density, atomic weight, and bandgap of the material, described in detail by Tanuma [149]. TMFP describes the frequency at which electrons undergo elastic scattering events by

$$\lambda_t = \frac{1}{N\sigma_t} \quad (4.51)$$

Which depends on the so-called transport cross section (σ_t) of the atom. These σ_t have been calculated for a variety of atomic potential models [154]. EALs as a function of λ_i and λ_t for a wide range of materials with α ranging from 0° to 50° and electron energies between 61 eV and 2016 eV were fit by

$$L = \lambda_i \left(1 - \frac{B\lambda_i}{\lambda_i + \lambda_t} \right), \quad (4.52)$$

where $B = 0.735$ is a linear fit parameter determined by Jablonski [154].

Powell and Tasneem [148] describe two methods for relating film thickness to effective attenuation length for an overlayer (v) and substrate (s) taken at X-ray incidence angle θ and electron emission angle α using measured intensity ratios. Both methods consider elastic-scattering effects to be negligible. The first method uses the difference in peak intensity of the substrate signal I^s for a pure substrate I_0^s compared to the intensity attenuated with an overlayer I_t^s to relate EAL to overlayer thickness by

$$L = \frac{t}{(\ln I_0^s - \ln I_t^s) \cos \alpha}. \quad (4.53)$$

The second method additionally uses the peak intensities of the overlayer I^v for a very thick overlayer I_∞^v and for an overlayer of a given thickness I_t^v to determine the ratios of peak intensities for overlayer and substrate. The thickness dependent EAL is given by

$$L = t \left[\left(F + \frac{I_t^V/I_t^S}{I_\infty^V/I_0^S} \right) \cos \alpha \right]^{-1}, \quad (4.54)$$

where F depends on the photoelectron energy as

$$F = \frac{e^{-t/L_V \cos \alpha}}{e^{-t/L_S \cos \alpha}}, \quad (4.55)$$

where L_V and L_S are EALs for the overlayer and substrate respectively through the film.

4.6: Other Techniques

4.6.1: X-ray Fluorescence

When an X-ray of sufficient energy excites a core-shell electron into vacuum level, the atom relaxes by filling the core-hole with a valence electron accompanied by the ejection of a photon (fluorescence) or another electron (auger). Measuring photons emitted is the basis of X-ray fluorescence (XRF), which provides quantitative information about the elemental composition and coverage of material. Analyzing the characteristic energies at which photons are emitted gives the atomic composition of a sample at sub-monolayer concentrations. Measuring relative phonon intensities can extract the effective coverage of the atomic species, provided geometry, XRF emission efficiency, and absorption effects are properly accounted for [156].

4.6.2: Low-Energy Electron Diffraction

The low-energy electron diffraction (LEED) technique, much like in-plane X-ray diffraction, generates a reciprocal space lattice by the diffraction of a collimated beam of electrons (20-200 eV). The low electron energy makes LEED sensitive to the top 5-10 Å of a surface, owing to a large interaction cross section $\sim 1 \text{ Å}^2$, over 10^6 times greater than X-rays with matter. The downside of the strong interaction between electrons and matter is that the kinematic approximation does not hold for LEED, so any analysis based on LEED spot intensities [157] requires the

implementation of dynamical diffraction theory. Herein, LEED is used as a qualitative *in situ* monitor the evolution of surface structures, whereas X-ray and other surface science techniques are used for structure determination.

Chapter 5: B/Ag(111) Interface

5.1: Abstract

Atomically thin two-dimensional (2D) materials exhibit superlative properties dictated by their intralayer atomic structure, which is typically derived from a limited number of thermodynamically stable bulk layered crystals (e.g., graphene from graphite). The growth of entirely synthetic 2D crystals – those with no corresponding bulk allotrope – would circumvent this dependence upon bulk thermodynamics and substantially expand the phase space available for structure-property engineering of 2D materials. However, it remains unclear if synthetic 2D materials can exist as structurally and chemically distinct layers anchored by van der Waals (vdW) forces, as opposed to strongly bound adlayers. Here, we show that atomically thin sheets of boron (i.e., borophene) grown on the Ag(111) surface exhibit a vdW-like structure without a corresponding bulk allotrope. Using X-ray standing wave (XSW)-excited X-ray photoelectron spectroscopy (XPS), the positions of boron in multiple chemical states are resolved with sub-Ångström spatial resolution, revealing that the borophene forms a single planar layer that is 2.4 Å above the unreconstructed Ag surface. Moreover, our results reveal that multiple borophene phases exhibit these characteristics, denoting a unique form of polymorphism consistent with recent predictions. This observation of synthetic borophene as chemically discrete from the growth substrate suggests that it is possible to engineer a much wider variety of 2D materials than those accessible through bulk layered crystal structures.

5.2: Introduction

Boron can form highly coordinated networks built around a motif of unconventional covalent bonds, which are frequently delocalized about three or more atoms [158,159]. Recently,

2D sheets of borophene have been synthesized by depositing pure boron on atomically flat Ag(111) substrates under ultra-high vacuum (UHV) conditions [5,6], as illustrated in Figure 5.1a. These structures are distinct from conventional atomically thin 2D materials, which are derived from thermodynamically stable bulk layered crystals [160] (e.g., graphene from graphite) and exhibit superlattice properties [30,161,162] dictated by their intralayer atomic structure. In contrast, borophene is believed to exhibit a planar form similar to laterally fused nanoscale boron clusters [49,94,159,163,164], with a number of predicted, energetically similar vacancy superlattices characterized by a vacancy concentration v_x [93,165]. Specifically, the $v_{1/6}$ and $v_{1/5}$ structure models—shown in Figure 5.1b,c respectively—have been proposed for borophene on the Ag(111) surface [5,49,101]. These structures should exhibit distinct chemical signatures due to the differences in B-B coordination numbers (labeled in the inset models), with the $v_{1/6}$ structure demonstrating a 2:2:1 ratio of 4-fold, 5-fold, and 6-fold coordination and the $v_{1/5}$ showing a 1:1 ratio of 4-fold and 5-fold coordination. Despite the differences in in-plane structure between the two models, the predicted vertical separation from the Ag(111) substrate is 2.4 Å in both cases – a value similar to the gap between graphene [74,166] or hexagonal boron nitride [120] and metal growth substrates. Because the out-of-plane structure of borophene with respect to the underlying Ag(111) substrate has not been directly quantified, it remains experimentally unclear whether borophene is comprised of weakly bound sheets in a planar [5,49,101] or buckled [6] morphology or as a strongly chemisorbed layer. Here, we characterize the structure of borophene under pristine UHV conditions with XSW-excited XPS [122,167], which measures the distribution of atoms relative to the substrate lattice with both sub-Å spatial resolution and chemical state specificity. Independent of the specific in-plane structure, borophene is found to exist as a single, atomically

flat layer (i.e., not buckled) that is separated from the underlying Ag(111) substrate by a noncovalent gap of 2.4 Å with no evident B-Ag primary bonding. This work thus experimentally demonstrates that borophene is a synthetic, elemental 2D material with no bulk analogue.

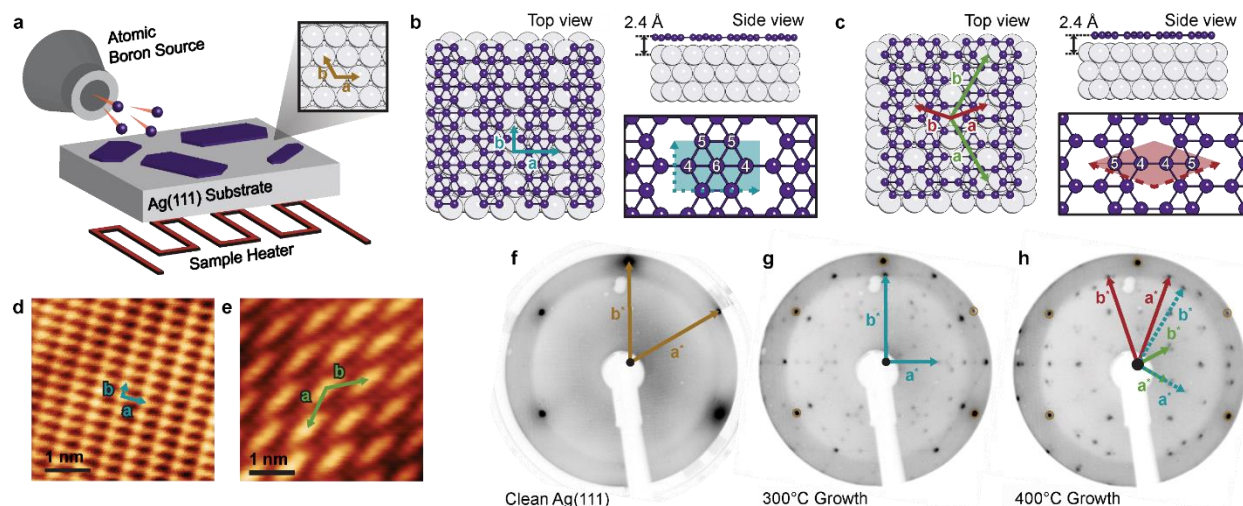


Figure 5.1: Borophene synthesis and atomic structures. (a) Schematic of borophene growth. (b,c) Atomic models of Ag(111)-supported borophene in the $\nu_{1/6}$ and $\nu_{1/5}$ structures, respectively. The enlarged models show the LEED derived rectangular (R) and diamond (D) 2D unit cells over each phase with the boron atomic coordination numbers labeled. (d,e) STM topography images showing the atomic-scale structures corresponding to the R and D phases. (f,g,h) LEED patterns acquired at 70 eV, corresponding to (f) clean Ag(111), (g) borophene growth at 300 °C (predominantly R phase), and (h) borophene growth at 400 °C (predominantly D phase). (STM images in a and b provided by A.J. Mannix)

Two structural phases of borophene have been observed experimentally via scanning tunneling microscopy (STM) and low-energy electron diffraction (LEED): a primitive rectangular phase [R phase; (Figure 5.1d)] and a diamond phase [D phase; (Figure 5.1e)] [5,6], which are expected to match the computationally predicted $\nu_{1/6}$ and $\nu_{1/5}$ structures, respectively [5,100,101,168]. The phase of borophene is determined by the boron deposition rate and the Ag(111) substrate temperature during growth [5,6].

5.3: Methods

5.3.1: LEED at I09

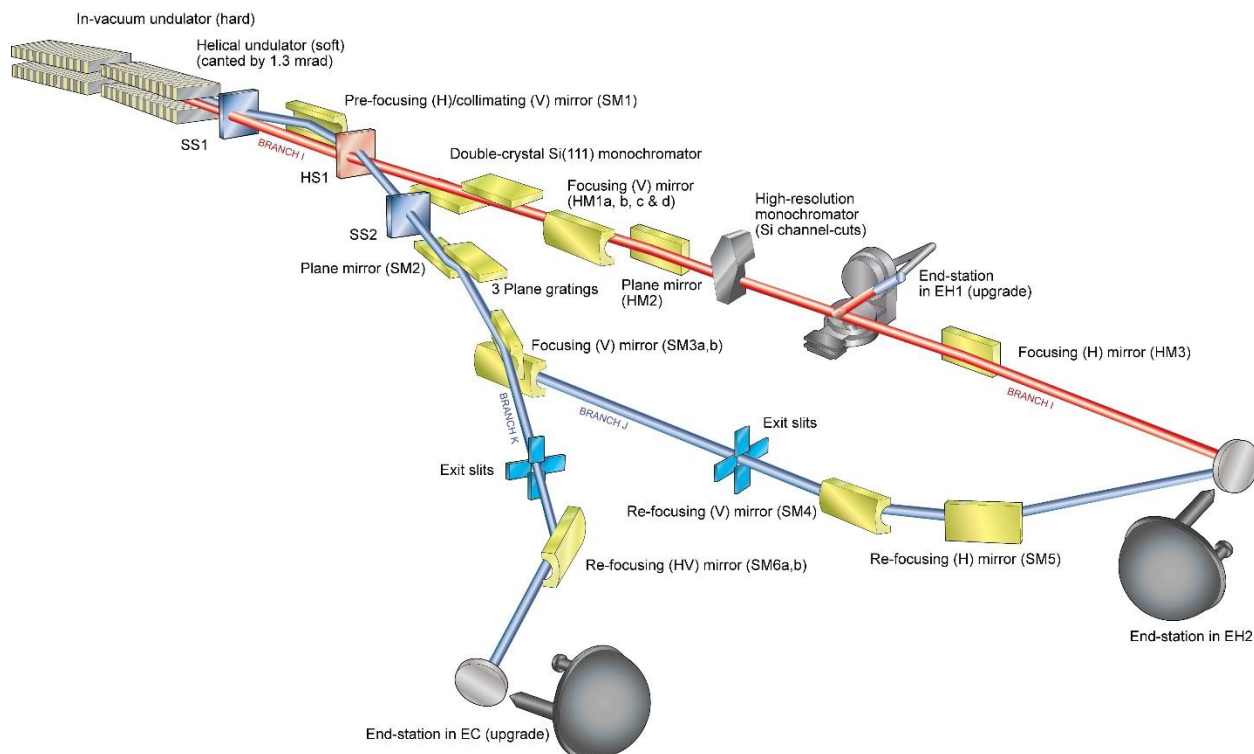


Figure 5.2: Diagram of the I09 beamline at Diamond. Experimental was performed in the EH2 end-station using hard and soft X-rays from separate undulators. (From Ref. [169])

The UHV system in EH2 contains 2 surface preparation chambers (SPC-1 and SPC-2) and the analysis chamber. Borophene samples were prepared in SPC-2, which is equipped with a QCM and has a hBN (ceramic) heater (accurate to $\pm 10^\circ$) and radiative or e-beam filament heating. Both SPC-2 and the analysis chamber are equipped with LEED systems. The analysis chamber has a higher resolution MCP-LEED. LEED patterns were acquired to verify the 2D crystal phases present after boron deposition. The LEED pattern for the 300 °C growth (Figure 5.1g) is consistent with the R phase [170] and the $v_{1/6}$ reciprocal lattice vectors (but rotated 30° with respect to the Ag spots). Growth at 400 °C results in a LEED pattern (Figure 5.1h) consistent with predominantly D

phase [6], which can be explained by a combination of the reciprocal lattice vectors of both the $\nu_{1/5}$ and $\nu_{1/6}$ models. As will be shown later by XPS, the 300 °C borophene is ~90% R phase and the 400 °C borophene is ~90% D phase.

5.3.2: X-ray at I09

To analyze the character of the bonds at the B/Ag(111) interface, we probed the chemical identity of the R and D phases *in situ* using XPS and XSW at the Diamond Light Source I09 beamline, which is capable of providing both soft (100 – 2100 eV) and hard X-rays (2.1 – 20 keV) at the same spot on the sample from two separate undulators. Soft X-rays used a defocused beam size of 300 x 300 μm^2 . Hard X-rays were focused down to 40% of the original 300 x 300 μm^2 beam size. XSW measurements were acquired using hard X-rays in a back-reflection geometry (i.e., $\theta_B \lesssim 90^\circ$) to maximize the B 1s yield and minimize the effect of Ag(111) mosaicity [122]. An incident beam energy of $E_\gamma = 2.629$ keV was selected by tuning the first harmonic of the I09 undulator and the Si(111) double-crystal monochromator. An incident beam energy of $E_\gamma = 2.629$ keV was selected by tuning the first harmonic of the I09 undulator and the Si(111) double-crystal monochromator to measure Ag{111}. At this energy, the incident beam full-width half-maximum (FWHM) bandwidth was $\Delta E_\gamma = 0.36$ eV. The undulator was tuned to 3.06 keV to collect Ag(020). The third harmonic was tuned to 4.29 keV to access the Ag(022). The Bragg diffracted beam in this near back-reflection geometry was measured by a CCD camera pointed at a Cu plate coated with YAG fluorescent powder. We measured O 1s, Ag 3d, C 1s, B 1s, and survey XPS spectra at variable soft X-ray energies, the FWHM bandwidth was $\Delta E_\gamma = 90$ meV at 500 eV. No evidence of other elements (namely, oxygen or carbon) was observed in the survey scans, verifying a

chemically pure borophene sample. Borophene samples were found to tolerate X-ray irradiation with no apparent degradation (i.e., no change in B 1s signal) despite multi-hour X-ray exposures.

Table 5.1: Energies and angles to access Ag Bragg conditions.

	Energy (keV)	300 °C borophene		400 °C borophene	
		Polar (°)	Azimuth (°)	Polar (°)	Azimuth (°)
Ag(111)	2.6327	3.7	18.04	3.9	18.04
Ag($\bar{1}11$)	2.6327	72.3	84.09	72.4	85.48
Ag(020)	3.0357	58.3	22.50	58.4	21.51
Ag(022)	4.2917	-	-	37.1	84.473

All X-ray measurements were performed in the analysis chamber of the I09 end-station. Photoelectron spectra were acquired using a Scienta EW4000 HAXPES analyzer aligned with the horizontal polarization direction of the incident beam. The soft X-ray incident beam energy was set at 700 eV for collecting the survey and O 1s spectra, 450 eV for the Ag 3d and C 1s spectra, and 350 eV for the B 1s spectrum and Fermi energy measurement. Soft XPS measurements were performed at an incident angle $\alpha = 60^\circ$ to maximize the collected photoelectron emission from the sample. Survey scans (**Error! Reference source not found.**) of the borophene on Ag(111) reveal characteristic binding energies (E_b) of only silver and boron. No evidence of other elements (namely, oxygen or carbon) was observed in the survey scans, verifying a chemically pure borophene sample. To collect angle-resolved XPS, the area of the detector was divided into 12 or 16 angular slices over the usable angular acceptance range of 51.6° , with a maximum acceptance of the XPS detector of 58.0° . XPS data were analyzed using CasaXPS software [171]. Additionally, B 1s spectra were also measured at $\alpha = 30^\circ$ to acquire depth-sensitive XPS data of the borophene samples. XPS binding energy scale calibration for all the soft and hard spectra was

established by measuring the Fermi edge (Figure 5.3) at 350 eV and setting the position (from a step down background fit) to $E_b = 0$. XPS spectra were acquired at multiple lateral locations on the sample surface to ensure that the data presented are representative of the sample. The only observable change was a slight variation in the majority and minority phase fraction.

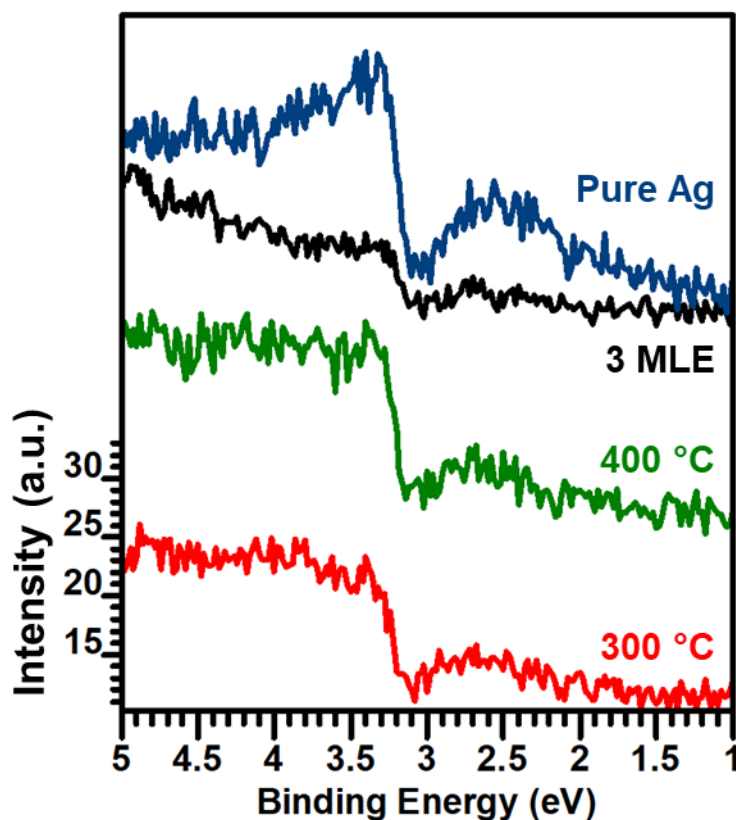


Figure 5.3: Fermi edge measurements of 300 °C, 400 °C, 3 monolayer-equivalent boron, and Pure Ag.

5.3.3: STM at Argonne

Comparative STM imaging (Figure 5.1d,e) was performed in a separate UHV system on samples grown under similar conditions (at a growth temperature of ~ 400 °C), resulting in the presence of both R and D phase islands. The STM images were acquired by an Omicron-Scienta

Cryo-SPM microscope at 2.5 K in constant-current topography mode, using an electrochemically etched tungsten tip.

5.4: Synthesis

5.4.1: Synthesis of $\nu_{1/6}$ and $\nu_{1/5}$ phases

Samples were grown in a dedicated preparation chamber attached to the main X-ray analysis chamber at beamline I09 at the Diamond Light Source under ultra-high vacuum (UHV, $P < 5 \times 10^{-10}$ mbar). Borophene was grown on single-crystal Ag(111) substrates (>99.999% purity) purchased from Mateck and Surface Preparation Laboratories. Substrates were prepared by repeating cycles of Ar ion sputtering (1 kV) and annealing (550 °C), and the quality of the surface was confirmed by LEED and XPS. The Ag(111) substrate was heated radiatively by a ceramic BN ribbon. The sample temperature was calibrated based on measurements of a reference sample composed of a diamond substrate bonded to a thermocouple. Boron was deposited from a FOCUS EFM-3 electron beam evaporator using a solid boron rod (99.9999% purity) purchased from ESPI metals. The boron deposition rate was monitored with a quartz crystal microbalance (QCM) to achieve consistent deposition rates of 0.002 Å/s during borophene growth. Boron was deposited for 20 min to a coverage of nominally 0.3 B/Å², as defined by the QCM-measured deposition rate for the 300 °C and 400 °C samples presented in the manuscript. One complete monolayer of borophene corresponds to 0.35 B/Å² and 0.29 B/Å² in the $\nu_{1/6}$ and $\nu_{1/5}$ models, respectively, as shown in Figure 5.1b,c. The XSW measurement further constrains the boron coverage, such that it cannot significantly exceed 1 monolayer. A multilayer boron reference sample was deposited on Ag(111) at room temperature, yielding a thickness of approximately 8 Å and coverage of 1.06 B/Å². The relative B 1s intensities being 1.1, 1.0, and 3.9 between the 300 °C and 400 °C

borophene and 20 °C multilayer boron samples confirm QCM measurements. Attenuation of the Ag 3d signal due to the presence of borophene further confirm sub-monolayer overlayers with 0.23 B/Å² and 0.29 B/Å² coverage for the 300 °C and 400 °C borophene [172]. LEED patterns were acquired at room temperature using conventional reverse-view optics (OCI Vacuum Microengineering).

2D reciprocal space vectors were calculated from the $v_{1/6}$ and $v_{1/5}$ structural models [5,49,101] to provide a comparison for the LEED patterns. LEED patterns were taken at room temperature using a conventional reverse-view diffractometer (OCI Vacuum Microengineering). Figure 5.4a,e present simulated reciprocal space vectors \mathbf{a}^* and \mathbf{b}^* for the $v_{1/6}$ and $v_{1/5}$ models, respectively. The borophene orientational epitaxy on the 6-fold symmetric Ag(111) surface results in 3 unique orientations of borophene islands. Because LEED measures over a spot size on the order of hundreds of microns, all borophene orientations are represented in the LEED patterns. This effect is replicated by superimposing the calculated reciprocal lattice at 0°, 120°, and 240° orientations (Figure 5.4b,f).

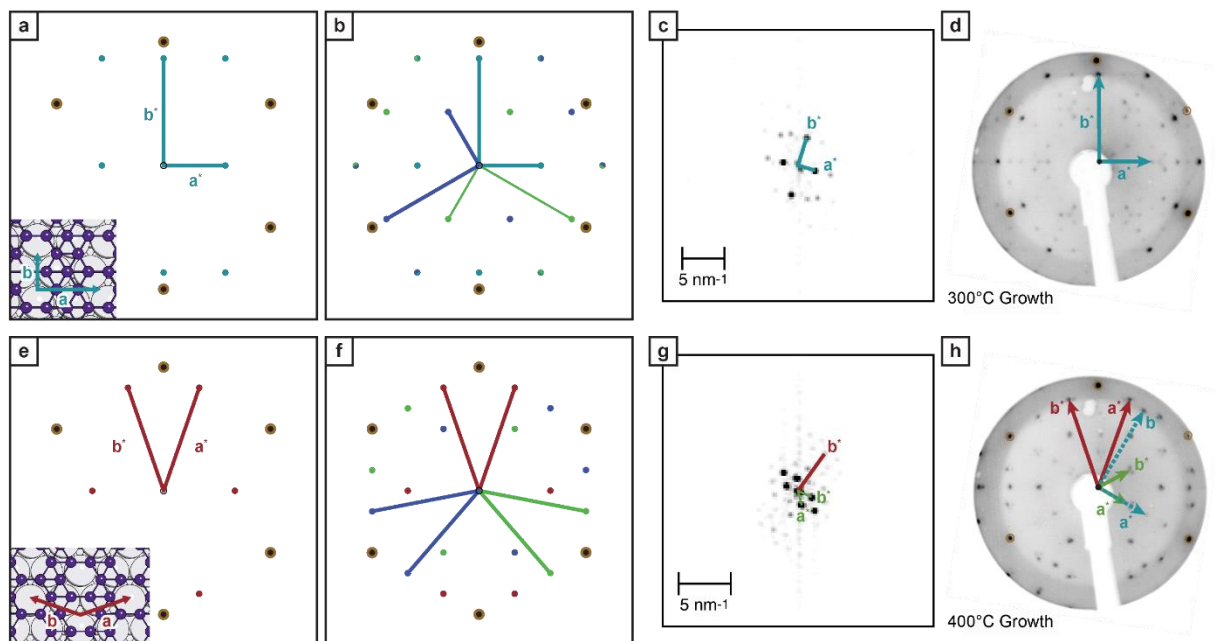


Figure 5.4: Reciprocal space analysis of in-plane borophene atomic structure. (a,e) Calculated reciprocal lattice for the $v_{1/6}$ and $v_{1/5}$ structures, respectively. (b,f) Reciprocal lattices from (a,e), superimposed for three orientations rotated 120° (green) and 240° (blue), corresponding to the symmetry observed experimentally over a larger area of the sample. (c,g) FFT of STM images in Figure 5.1d,e corresponding to the R and D lattices, respectively. (d,h) LEED patterns reproduced from Figure 5.1g,h for comparison. Note that the LEED determined R lattice in (d) is consistent with the $v_{1/6}$ model rotated 30° relative to the Ag lattice in (b).

Additional reciprocal space information can be obtained by calculating the Fourier transformations of STM images. Figure 5.4c,g shows FFTs calculated for the STM images of the R phase (Figure 5.1d) and the D phase (Figure 5.1e). In comparison with the calculated reciprocal space lattices and the FFTs of STM data, we are able to account for the principal features in the LEED patterns (Figure 5.4d,h). Based on this analysis and literature precedent [6,170], we can assign the 300°C as predominantly R phase and the 400°C as predominantly D phase.

5.4.2: Coverage Calibration

To avoid the modulo-d ambiguity present in the XSW measurement, $0.3 \pm 0.1 \text{ B}/\text{\AA}^2$ of Boron was deposited to maintain sub-monolayer borophene coverage. Where one complete

monolayer of borophene corresponds to $0.35 \text{ B}/\text{\AA}^2$ and $0.29 \text{ B}/\text{\AA}^2$ in the $\nu_{1/6}$ and $\nu_{1/5}$ models, respectively. The relative B 1s intensities of 1.0, 0.9, and 3.5 between the 300 °C and 400 °C borophene and 20 °C multilayer boron samples confirm absolute quartz crystal monitor (QCM) measurements. Absolute coverage was calibrated using a QCM mounted on the backside of the sample manipulator. Boron flux was measured with the QCM prior to and after deposition onto the Ag(111) surface. The minimal detectable deposition rate of the QCM is $0.06 \text{ \AA}/\text{s}$, approximately 3x higher than the target deposition rate. To achieve a reliable boron flux, QCM measurements were collected for 10 minutes prior to and after deposition. No clear drift in the QCM data is present over 30 minutes of collection time. A $\sim 1 \text{ m}\text{\AA}/\text{s}$ discrepancy between the QCM measurements was found prior to and after boron deposition, which is the primary source of error in calculated coverage. The SPC-2 manipulator is cooled with water to maintain low pressure during annealing. The pumping of the water induces cyclical variations in the QCM vibration readings, therefore all QCM data was taken over an integrated time range over multiple cycles.

Table 5.2: QCM measured B deposition rate prior to and following deposition on Ag(111).

Deposition Rate ($\text{m}\text{\AA}/\text{s}$)	300 °C	400 °C
QCM Before	2.1	1.6
QCM After	1.1	2.5
Average QCM	1.6 ± 0.5	2.0 ± 0.5
Deposition Time (s)	1,320	1,200

The successful deposition of sub-monolayer borophene was further verified from periodic LEED measurements during boron deposition. Every 5 minutes, the sample manipulator was turned away from the B deposition source and put in position for a LEED measurement. The extension of the LEED system effectively blocked further boron deposition. The series of LEED

images clearly shows increasing borophene spot intensity, which confirms the formation of borophene throughout the 20 minute deposition. The NIST Electron Effective Attenuation Length Database [152] yielded inelastic mean free path (IMFP) = 5.912 Å and transport mean free path (TMFP) = 5.753 Å for 84 eV electrons in boron with $\theta = 60^\circ$ and $\alpha = 30^\circ$.

5.4.3: Borophene Annealing

Post deposition annealing of the 300 °C borophene sample was performed in an attempt to transition from R to D phase borophene. The sample was brought to 300 °C, the temperature was then increased at a rate of 25 °C steps every 10 minutes in a step-wise manner. LEED patterns were taken at every 25 °C step. After reaching 500 °C, the borophene spots were barely visible above the background from the indirect heating source. Post anneal LEED images (Figure 5.5f) reveal a considerable reduction in borophene spots intensity for both the majority R and minority D phase as compared to the as-grown 300 °C LEED pattern (Figure 5.5a).

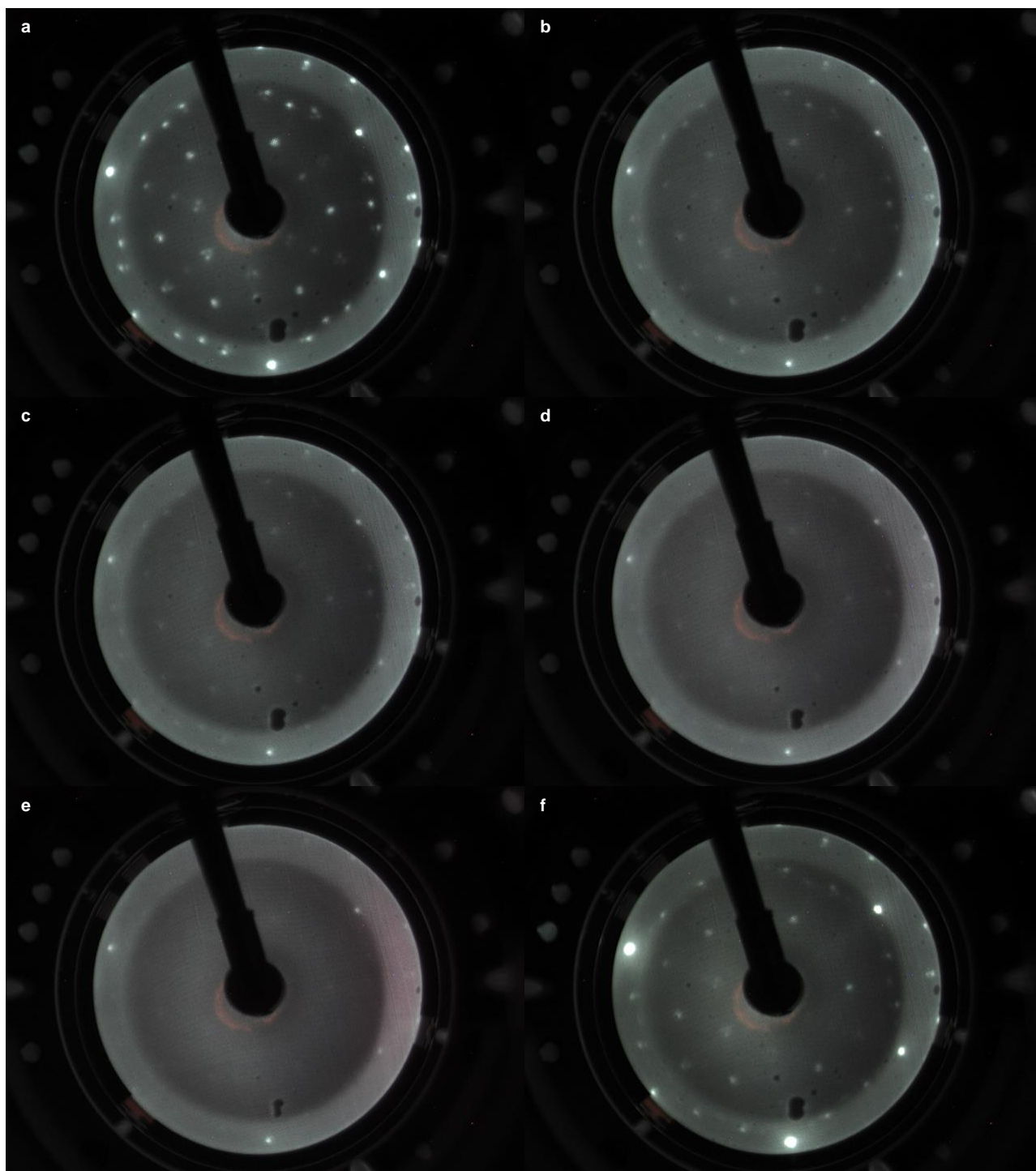


Figure 5.5: LEED patterns of 300 °C Borophene sample (a) as-grown taken at ~20 °C, post growth anneal taken at (b) 9.0 V (~350 °C), (c) 10.0 V (~400 °C), (d) 11.0 V (~450 °C), (e) 12.0 V (~500 °C), and (f) at ~20 °C following the anneal. LEED patterns were acquired at 70 eV.

5.5: Results

5.5.1: High-Resolution X-ray Photoelectron Spectroscopy

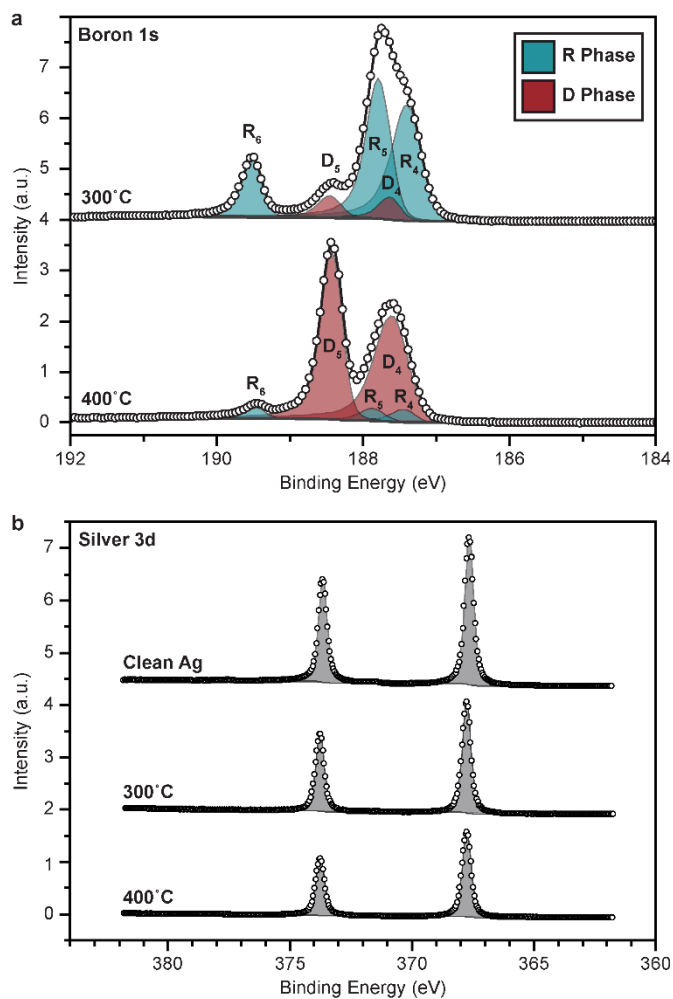


Figure 5.6: High-resolution XPS of borophene. (a) Boron 1s core-level spectra for borophene samples grown at 300 °C and 400 °C. (b) Silver 3d core-level spectra of clean Ag(111) and borophene samples grown at 300 °C and 400 °C. Both plots display the raw data (dots), fitted peak components (filled shapes), and fitted envelope (grey line).

Figure 5.6 shows high-resolution B 1s and Ag 3d core-level spectra for borophene grown at 300 °C and 400 °C. In both samples, the B 1s spectra (Figure 5.6a) are composed of a common set of chemically-shifted components, and are considerably narrower than multilayer boron B 1s

spectra (Figure 5.5). This observation suggests that the boron atoms in borophene occupy a number of discrete local bonding environments. In particular, the spectra can be fit with five individual components, which we attribute to different B-B coordination numbers present in the two principal borophene phases: three for the R phase ($R_{4,5,6}$ —i.e., 4-fold, 5-fold, and 6-fold coordination) and two for the D phase ($D_{4,5}$ —i.e., 4-fold and 5-fold coordination), following the trend observed in graphene of higher binding energy corresponding to higher coordination [173]. The selective broadening of the $R_{4,5}D_4$ boron peaks is from distinct vacancy structures at borophene edges and grain boundaries, which favor low coordination. The relative integrated peak intensity of these components reflects the proportions of boron atoms in their corresponding chemical environment. The intensity ratios show the 300 °C sample is ~90% R phase and ~10% D phase, whereas the 400 °C sample is ~10% R phase and ~90% D phase. Moreover, the ratios in peak intensities are $I_{R_4}:I_{R_5}:I_{R_6} \approx 2:2:1$ for the R phase and $I_{D_4}:I_{D_5} \approx 1:1$ for the D phase, which are consistent with the predicted ratios of 4-fold, 5-fold, and 6-fold coordinated boron atoms in the $v_{1/6}$ and $v_{1/5}$ borophene crystal structures [5,49,101]. In both samples, the Ag 3d spectra (Figure 5.6b) are indistinguishable from that of clean Ag(111), apart from mild attenuation due to the boron overlayer, which is indicative of weak B-Ag interactions.

Table 5.3: XPS fitting parameters for Soft and Hard B 1s X-ray spectra taken at identical collection range of takeoff angle α . Binding energies (E_b) and peak full-width half-maxima (FWHM) are listed in units of electron Volts.

B 1s	350 eV Soft X-rays						2.629 keV Hard X-rays					
	300 °C Borophene			400 °C Borophene			300 °C Borophene			400 °C Borophene		
	B%	E_b	FWHM	B%	E_b	FWHM	B%	E_b	FWHM	B%	E_b	FWHM
R ₄	* 36.4	187.3	0.5	†7.0	187.4	0.5	* 37.0	187.1	0.8	*6.8	187.0	0.8
R ₅	* 36.4	187.7	0.4	†7.0	187.8	0.4	* 37.0	187.5	0.7	*6.8	187.4	0.7
R ₆	16.0	189.5	0.4	†3.5	189.4	0.3	16.5	189.2	0.6	3.4	189.2	0.6
D ₄	†5.6	187.6	0.6	40.4	187.6	0.6	*4.5	187.4	0.8	* 41.3	187.3	0.7

D ₅	[†] 5.6	188.4	0.3	42.0	188.4	0.3	5.0	188.2	0.5	41.9	188.1	0.6
----------------	------------------	-------	-----	-------------	-------	-----	-----	-------	-----	-------------	-------	-----

^{*,†}Values held at fixed relative B% during fitting. Bold indicates majority phase.

The XPS survey data (**Error! Reference source not found.**) show only boron and silver core-level peaks, confirming no contamination by carbon, oxygen, or other elemental species. The survey spectra show binding energies of Ag 3p at 572.7 eV, Ag 3d_{3/2} at 374.1 eV, Ag 3d_{5/2} at 368.1 eV, and B 1s at 187.7 eV. Auger MVV peaks were observed at 345 and 351 eV. High-resolution Ag 3d spectra (Figure 5.6b) are comprised only of Ag 3d_{3/2} and Ag 3d_{5/2} spin orbit components.

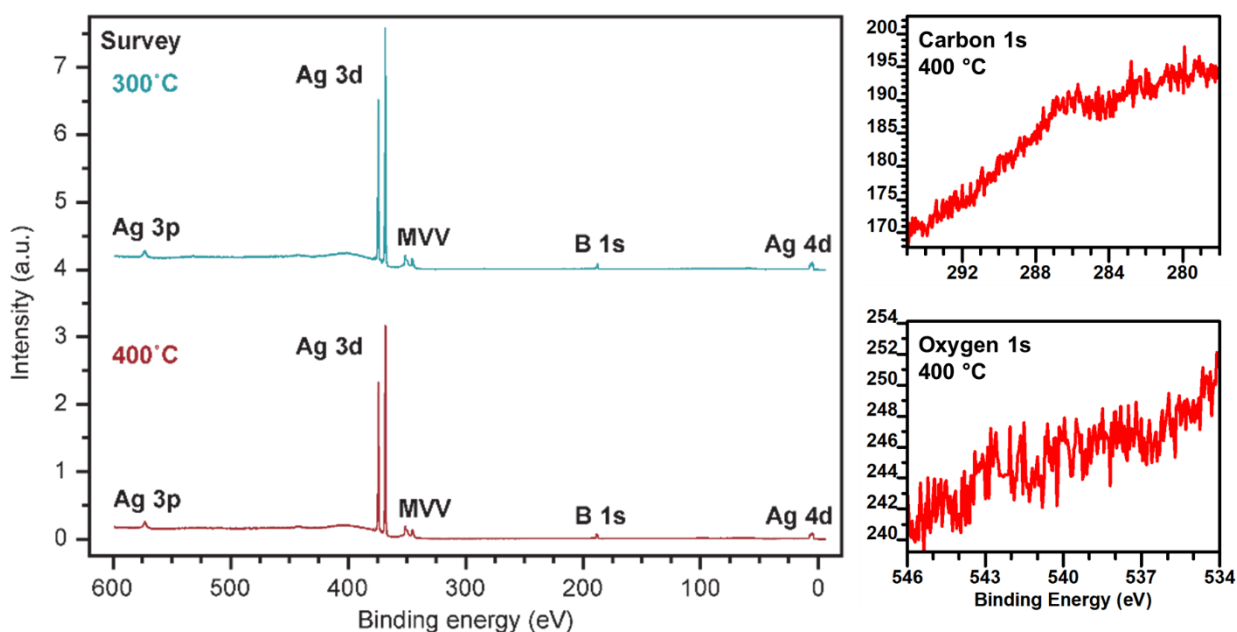


Figure 5.7: XPS survey, C 1s, and O 1s spectra of borophene 300 °C and 400 °C samples. Survey scans (left) show binding energies of silver and boron, and no evidence of other elements is evident, namely, carbon (top-right) or oxygen (bottom-right) from the raw data.

The Ag 3d_{5/2} E_b of 368.1 eV matches standard binding energies from Ag-Ag metallic bonds (368.2 eV) [174]. High-resolution Ag 3d core-level spectra from a clean Ag(111) control yielded the same FWHM and E_b as the Ag 3d spectra taken after borophene deposition (Table 5.4), indicating no major changes to the chemical environment of the surface silver atoms.

Table 5.4: XPS fitting parameters for Soft and Hard Ag 3d X-ray spectra taken at identical collection range of takeoff angle α . Binding energies (E_b) and peak full-width half-maxima (FWHM) are listed in units of electron Volts.

350 eV Soft X-rays						
300 °C		400 °C		Pure Ag		
Ag 3d	E_b	FWHM	E_b	FWHM	E_b	FWHM
5/2	367.8	0.42	367.8	0.42	367.7	0.43
3/2	373.8	0.42	373.8	0.42	373.7	0.43

2.629 keV Hard X-rays						
Ag 3d	E_b	FWHM	E_b	FWHM	E_b	FWHM
5/2	-*	0.43	-*	0.45	-*	0.44

*Values are the same after energy calibration.

The components R₄₋₆ and D₄₋₅ (Table 5.3) were fit using hybrid Doniach-Sunjic [144] line shapes in order to extract quantitative information regarding atomic binding energy and coverage. The five components show resolution-broadened FWHM of ~ 0.4 eV and E_b shifts of -0.3 eV, 0.1 eV, 1.8 eV, -0.1 eV, and 0.7 eV relative to 20 °C multilayer boron (187.7 eV, Figure 5.8).

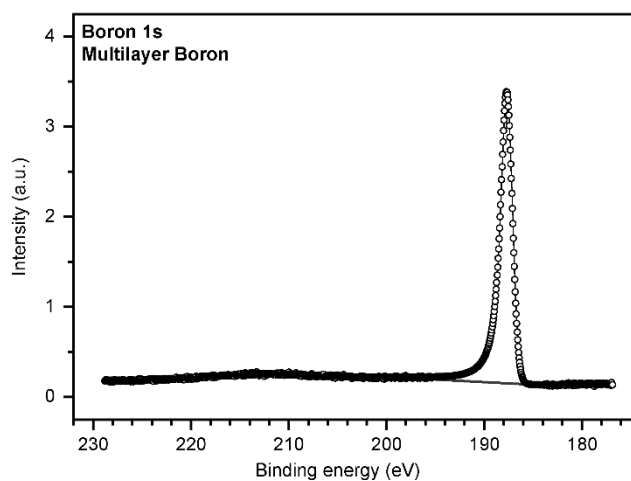


Figure 5.8: XPS of 20 °C deposited multilayer boron. The data (circles) are modeled with a 1-component fit (black line) with $E_b = 187.7$ eV and FWHM = 1.4 eV.

To investigate whether any chemical species possess a varying depth profile, we collected XPS data at 16 distinct photoemission angles [175]. Selecting a series of detector emission angles

between 4° and 56° varied the effective probing depth (Λ_{eff}) for B 1s (Figure 5.9) and Ag $3d_{5/2}$ photoelectrons by several Ångströms. The surface core-level shifts of Ag $3d_{5/2}$ are reportedly < 0.1 eV as compared to bulk [176], so surface states of pure Ag are indistinguishable from bulk. No components of the B 1s or Ag $3d_{5/2}$ spectra exhibit any relative dependence on takeoff angle, indicating that all boron species are co-located and that the Ag(111) surface is bulk-like.

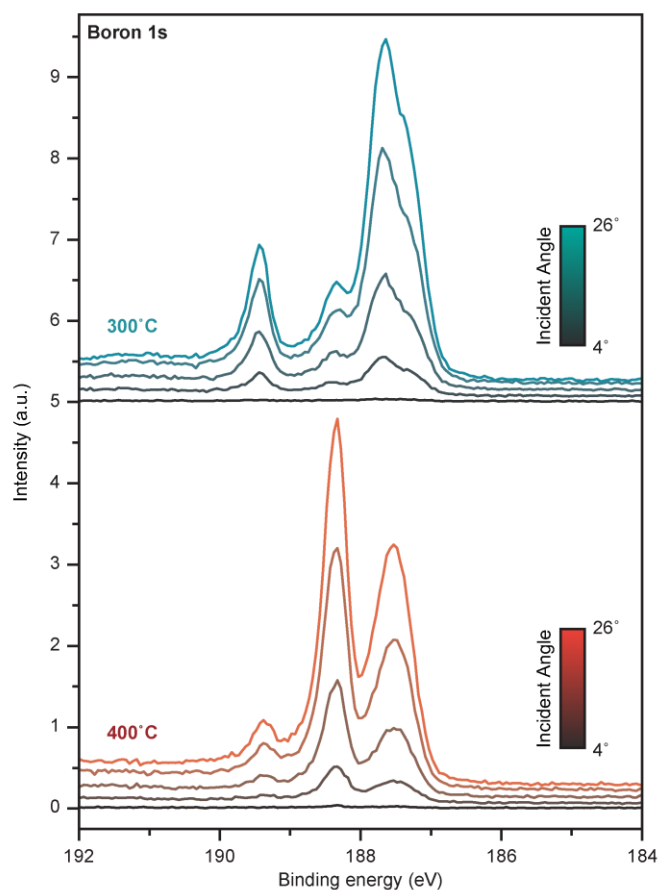


Figure 5.9: Angular-resolved boron 1s XPS from samples grown at 300 °C and 400 °C. Variable incident angle α is shown as 5 distinct slices.

5.5.2: X-ray Standing Wave Analysis

Although high-resolution XPS provides strong evidence of chemical coordination and co-location of boron species near the Ag(111) surface, precise structural determination requires

spatially resolved methods. The XSW technique enhances XPS with high spatial resolution by modulating the photoelectron yield with an X-ray standing wave formed by the interference between the incident and reflected X-ray beams at the Bragg condition (Figure 5.12a). The standing wave period is equal to the substrate Bragg diffraction plane d -spacing. Scanning the incident X-ray energy, E , through the Bragg condition causes the reflectivity, $R(E)$, to approach unity over an eV-wide band-gap and the XSW phase, $\phi(E)$, to shift by π -radians. Chemically specific structural information is acquired by monitoring changes in XPS intensity as the standing-wave shifts from being out-of-phase with the diffraction planes to being in-phase. The resulting XPS modulation can be analyzed to find the substrate lattice location of various atomic species both above and below the crystal surface [177,178]. Such measurements have previously proven to be effective in determining the chemically precise structure of 2D material interfaces [14,74,120]. Here, we use XSW-enhanced XPS to extract ensemble-averaged vertical positions of the surface silver and the chemically distinct boron species for both R and D phase borophene.

Table 5.5: For the two deposition temperatures, XPS determined boron percent speciation (Table 5.3), coherent fraction (f_s), coherent position (P_s), and mean heights (\bar{z}) from XSW analysis in Figure 5.12.

	300 °C borophene				400 °C borophene				^a model
	B%	f_s	P_s	^b \bar{z} (Å)	B%	f_s	P_s	^b \bar{z} (Å)	^b \bar{z} (Å)
<i>Total</i>	100	0.92(3)	0.02(1)	2.41(3)	100	0.91(3)	0.02(1)	2.40(3)	-
^c R ₄	37.0	0.89(2)	0.00(1)	2.36(2)	6.8	0.89(2)	0.01(1)	2.38(4)	2.37
^c R ₅	37.0	0.89(2)	0.00(1)	2.36(2)	6.8	0.89(2)	0.01(1)	2.38(4)	2.31
R ₆	16.5	0.93(2)	0.04(2)	2.47(4)	3.4	0.93(5)	0.06(4)	2.51(9)	2.44
^c D ₄	4.5	0.89(2)	0.00(1)	2.36(2)	41.3	0.89(2)	0.01(1)	2.38(4)	2.28
D ₅	5.0	0.79(5)	0.07(3)	2.52(3)	41.9	0.96(3)	0.03(1)	2.42(2)	2.31

^aB heights based on the DFT $v_{1/6}$ (R) and $v_{1/5}$ (D) structural models for borophene illustrated in Figures 5.9b,c.[49,101]

^bValues calculated using Ag(111) d -spacing = 2.359 Å.

^cValues held at fixed relative B% during fitting. Bold indicates majority phase.

Depending on the precise atomic distribution the photoelectron yield from a selected chemical species (s),

$$Y_s(E) = 1 + R(E) + 2\sqrt{R(E)}f_s \cos(\phi(E) - 2\pi P_s), \quad (6.1)$$

gives a distinct modulation versus energy that is parameterized by the Fourier amplitude (or coherent fraction, f_s) and phase (or coherent position, P_s) of the distribution profile [122,167]. Roughly speaking the coherent position is a normalized measurement of the atomic average position \bar{z}_s , modulo the 2.359 \AA d -spacing of the Ag(111) diffraction plane. The coherent fraction describes the atomic distribution width normal to the diffraction planes [124]. For example, a random distribution of atoms would produce $f_s = 0$ and $f_s = 1$ indicates all atoms are precisely located at P_s .

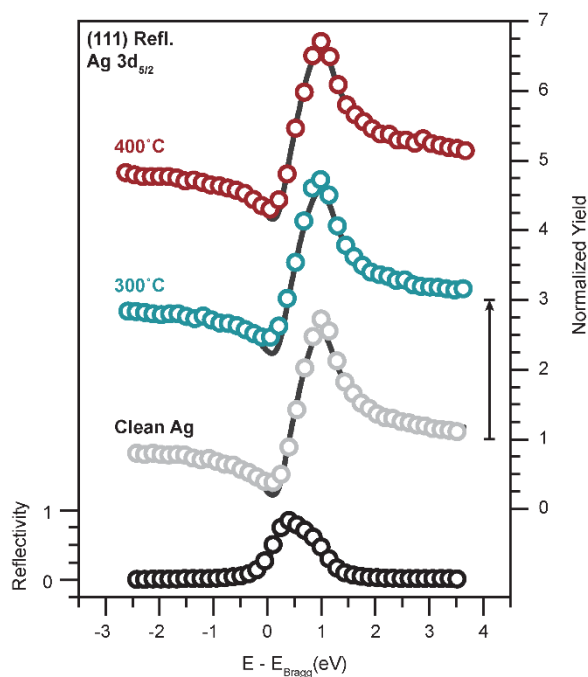


Figure 5.10: XSW characterization of silver at the borophene/Ag(111) interface. Data (circles) and eq. 5.1 model fits (black lines) for incident X-ray energy dependence of the X-ray reflectivity and normalized Ag $3d_{5/2}$ photoelectron yields of 400 °C, 300 °C, and pure Ag(111) control samples

probed at $\alpha = 5.3^\circ$. XSW results are identical within error, yielding near-unity coherent fractions $f_{400^\circ\text{C}} = 1.08(3)$, $f_{300^\circ\text{C}} = 1.03(3)$, and $f_{\text{pureAg}} = 1.04(3)$ and coherent positions $P_{400^\circ\text{C}} = P_{300^\circ\text{C}} = P_{\text{pureAg}} = 0.01(1)$ with all Ag $3d_{5/2}$ photoelectron yields.

The Ag $3d_{5/2}$ XSW-XPS yield results in $f_{\text{Ag}} = 1$ and $P_{\text{Ag}} = 1$ for all samples, indicating that all silver atoms within the ~ 10 Å sampling depth are unaffected by the presence of boron.

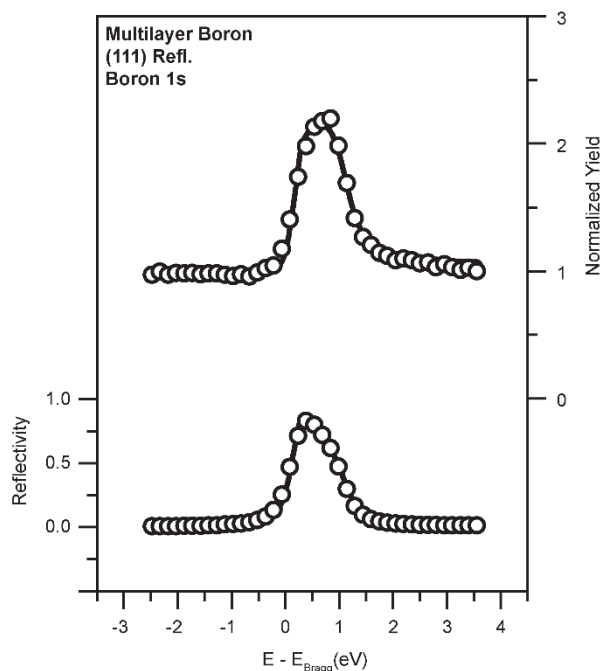


Figure 5.11: XSW characterization of 20 °C deposited multilayer boron on Ag(111). Data (circles) and model fits (black lines) for incident X-ray energy dependence of the X-ray reflectivity and normalized B 1s photoelectron yields of boron. Fits yielded coherent fractions $f = 0.22(3)$ and coherent positions $P = 0.09(1)$.

In contrast to the nearly random B 1s XSW-XPS distribution ($f = \sim 0.2$) for ~ 3 layers of boron deposited at 20 °C (Figure 5.11), the *total* B 1s XPS yield fit of both 300 °C and 400 °C borophene showed $f_t > 0.9$ and $P_t = 0.0$ corresponding to a narrow single-layer boron distribution (Gaussian width $\sigma_t = 0.15$ Å) positioned at 2.4 Å above the topmost Ag(111) atomic planes. Critically, this measurement indicates that, independent of the specific phase or B-B coordination, all boron atoms

in borophene are positioned at a noncovalent distance above the Ag(111) surface. The f_t and P_t values measured for borophene on Ag(111) are highly consistent with the DFT calculated values [49,101], apart from a slightly larger-than-expected distribution width ($\sigma = 0.1 \text{ \AA}$ expected for thermal disorder) that may be due to the very minor presence of boron clusters uncorrelated with the Ag(111) lattice (see supporting information for additional analysis). The relatively small calculated adhesive potential of the $v_{1/6}$ structure (175 meV/atom) [49] supports our observation that the interface is free of primary B-Ag bonds. This result shows that both R and D phase borophene are highly planar boron polymorphs stabilized by Ag(111).

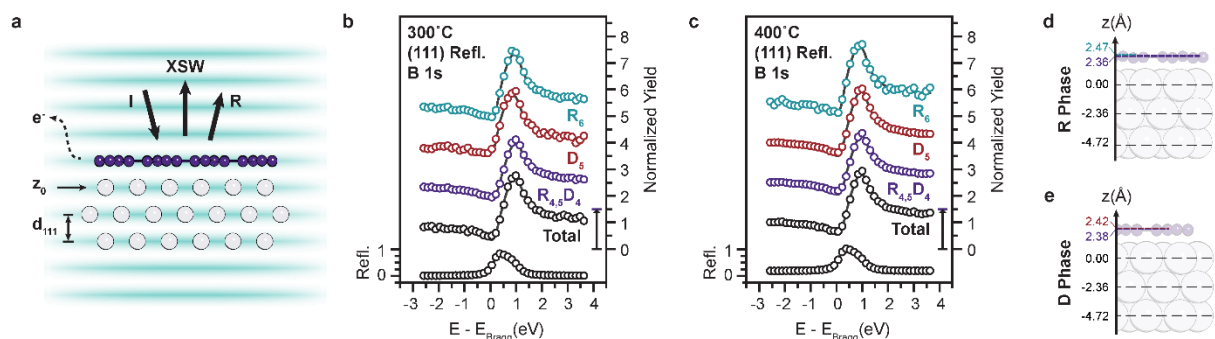


Figure 5.12: XSW characterization of the borophene/Ag(111) structure. (a) Schematic of XSW (blue lines) generated by interference between the incident (I) and reflected (R) X-ray beams during Bragg diffraction from a Ag(111) single-crystal with a D phase borophene layer. (b,c) Data (circles) and model fits (black lines) for incident X-ray energy dependence of the X-ray reflectivity and normalized B 1s photoelectron yields of samples grown at 300 °C and 400 °C, respectively. Total B 1s is shown with chemically distinct boron species from Figure 5.6a. (d,e) Structural characterization from XSW for the R phase and D phase derived from the 300 °C and 400 °C sample growths, respectively, with predicted positions from Table 5.5 denoted by solid lines. Coordination-specific structural information can also be extracted from the XSW data using the peak-fits obtained from high-resolution B 1s XPS (detailed fitting procedures given in the Supporting Information). A 5-component fit of the R phase and D phase to the 300 °C (Figure 5.12b) and 400 °C (Figure 5.12c) XSW-XPS data shows nearly identical photoelectron yields ($Y_{R_{4,5,6}D_{4,5}}$) for all components. The model fitting results, given in Table 5.5, reveal that all

chemically distinct species of borophene are highly planar ($f > 0.8$) with essentially the same 2.4 Å spacing above the terminal plane of Ag(111) atoms ($0.0 < P < 0.1$). These results are depicted schematically in Figure 5.12d,e for the 300 °C and 400 °C borophene samples relative to the $\nu_{1/6}$ and $\nu_{1/5}$ structures, respectively.

XSW measurements taken at multiple spots across the 300 °C and 400 °C samples were used to calculate 3σ error bars reported in Table 5.5. Equation 5.1 is derived using the dipole approximation, quadrupolar effects were taken into account to calculate the coherent fractions and positions of boron species listed in Table 5.5 [122]. Due to a large degree of spectral overlap, R_4 , R_5 , and D_4 peaks were held at constant relative intensity to avoid negative covariance during XSW fitting. The impact of this constraint on the interpretation of the D_4 phase is minimal as the R phase components are ~10% of the $R_4+R_5+D_4$ intensity for the 400 °C sample. However, for the 300 °C sample, this assumption precludes the decoupling of the XSW-induced modulations for the R_4 and R_5 signals. Analysis of individual chemical species reveal that the well-isolated 300 °C sample R_6 and 400 °C sample D_5 signals both exhibit exceptionally high coherent fractions ($f_{R_6D_5} > 0.93$) when compared to the co-constrained $R_{4,5}D_4$ components. It also appears that f_s increases for spectral components with large core-shifts (Table 5.3) relative to the location of the 20 °C multilayer boron sample peak (187.7 eV). Therefore, one explanation for a relatively low coherent fraction for low E_b components is the presence of uncorrelated boron. A 5% atomic fraction of boron with $f = 0.2$ intermixed (Figure 5.11) with the borophene would be sufficient to reduce the f_s of the $R_{4,5}D_4$ peak from 0.93 to 0.89. Boron clusters scattered across the borophene have previously been observed in STM, and an atomic fraction near 6% is consistent with large-area

STM scans of borophene at comparable boron coverages [6]. Assuming this fraction of boron clusters, $f_{R_{4,5}D_4}$ fall within expectations for thermal disorder.

5.5.3: Off-Specular X-ray Standing Wave Analysis

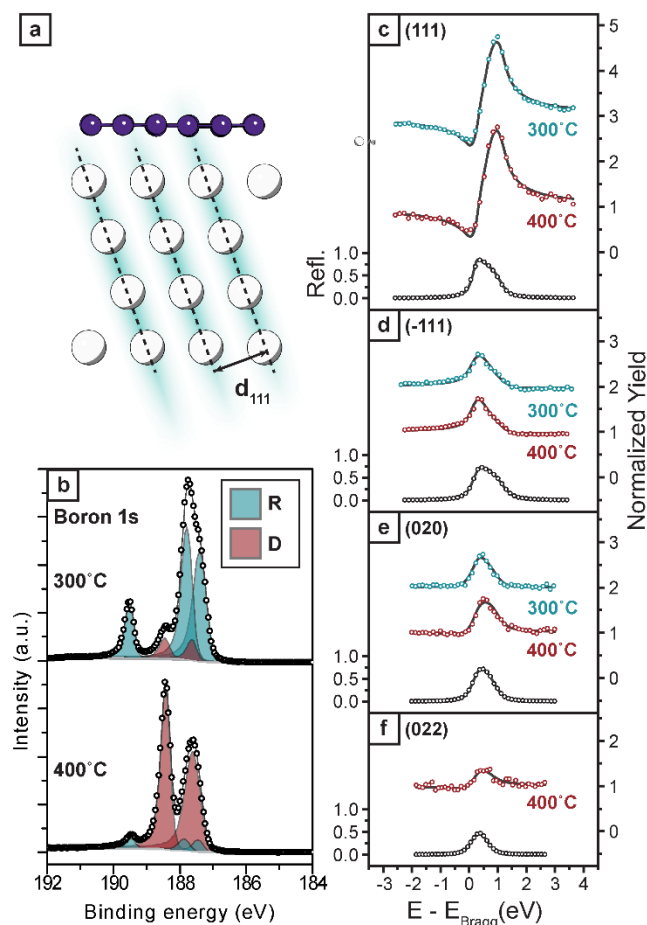


Figure 5.13: XSW characterization of the in-plane borophene/Ag(111) structure. (a) Schematic of XSW (blue lines) generated by interference between X-ray beams during $(\bar{1}11)$ Bragg diffraction from a Ag(111) single-crystal with a D phase borophene layer. High-resolution XPS of (b) B 1s core-level spectra for borophene samples grown at 300 °C and 400 °C. (c,d,e,f) Data (circles) and model fits (black lines) for incident X-ray energy dependence of the X-ray reflectivity of Ag(111), Ag($\bar{1}11$), Ag(020), and Ag(022) and normalized B 1s photoelectron yields of samples grown at 300 °C and 400 °C, respectively.

The yields of the measured off-normal reflections [Table 5.6, Ag($\bar{1}11$), Ag(020), and Ag(022)] show no differences in the 5 borophene peaks, evident from the unchanging normalized

XPS intensity profile with energy for each reflection. This indicates that the distinct chemical species of borophene have indistinguishable f_s and P_s for each of the three measured reflections. Borophene, however, is known to have distinct in-plane positions of the 4-fold, 5-fold, and 6-fold coordinated borons, so the origin of the seemingly identical photoelectron yields for the XPS peaks must come from the projection of the long-range borophene structure along the $\text{Ag}(\bar{1}11)$, $\text{Ag}(022)$, and $\text{Ag}(020)$.

Table 5.6: Coherent fraction (f^H) and coherent Position (P^H) of B relative to $H = hkl$ Bragg planes for the two deposition temperatures

	300 °C borophene		400 °C borophene	
	f^H	P^H	f^H	P^H
Ag(111)	0.92(3)	0.92(3)	0.91(3)	0.91(3)
Ag($\bar{1}11$)	0.2(1)	0.62(6)	0.2(1)	0.6(1)
Ag(020)	0.2(1)	0.00(5)	0.1(1)	0.7(2)
Ag(022)	-	-	0.2(1)	0.98(6)

The borophene and Ag share a common direction along the in-plane $\text{Ag}[\bar{1}10]$ vector, labeled $\mathbf{a}_{\text{Ag}(1\times 1)}$ in figure 511a. After traversing $3\mathbf{a}_{\text{Ag}(1\times 1)}$ the boron atoms (and vacancies) are in the same position above the Ag atoms. The same is true along $3\mathbf{b}_{\text{Ag}(1\times 1)}$, therefore the borophene is in (3×3) registry with the underlying $\text{Ag}(111)$. The two 4-fold, two 5-fold, and one vacancy are positioned at intervals of $3n/5$ along $\mathbf{a}_{\text{Ag}(1\times 1)}$ and $\mathbf{b}_{\text{Ag}(1\times 1)}$. The XSW measures sees these positions projected onto the $\text{Ag}(111)$ unit cell, recast as a hexagonal $\text{Ag}(1\times 1)$ cell with in-plane components $\mathbf{a}_{\text{Ag}(1\times 1)}$ along $\text{Ag}[\bar{1}10]$ and \mathbf{b} along $\text{Ag}[0\bar{1}1]$ and vertical \mathbf{c} along $\text{Ag}(111)$. When projected into the $\text{Ag}(1\times 1)$ cell, the boron atoms and vacancies are positioned at intervals of $\mathbf{a}/5$ and $\mathbf{b}/5$, with twenty boron atoms and five vacancies. This structure as seen by the XSW appears similar to

borophene, but shank down by a factor of 3 along both $\mathbf{a}_{\text{Ag}(1\times 1)}$ and $\mathbf{b}_{\text{Ag}(1\times 1)}$ and the 4-fold and 5-fold sites are reversed (see atoms labeled in Figure 5.14b).

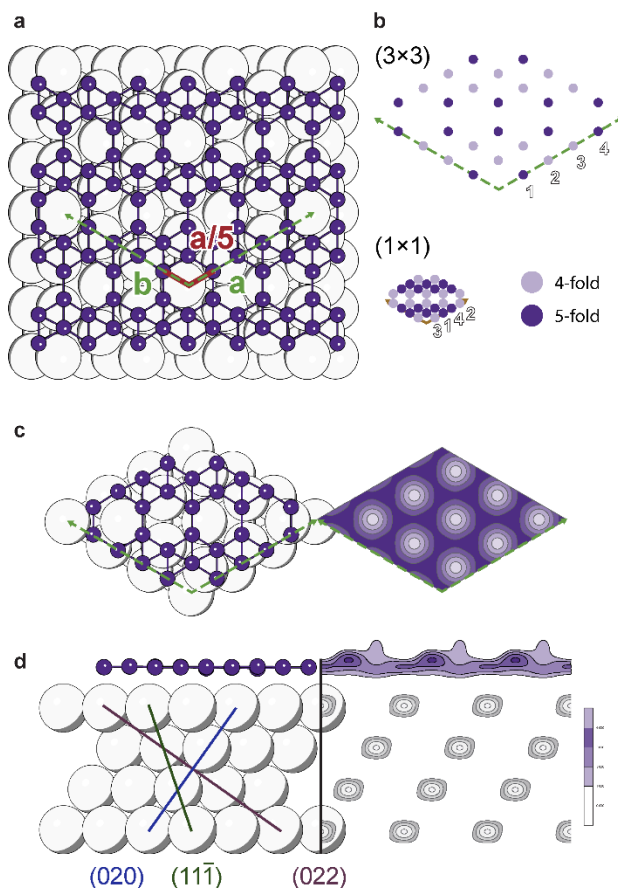


Figure 5.14: In-plane atomic model structure of (a) Ag(111)-supported borophene in the $\nu_{1/5}$ structure, the basis vectors of the Ag(3×3) cell labeled in green. (b) Reduction of the D phase borophene from Ag(3×3) to Ag(1×1). (c) top-down and (d) side view of (Left) atomic model and (Right) B atomic density.

The indistinguishable XSW-XPS peak yields of the off-normal measurements can be understood by examining the apparent B-Ag registry between $\nu_{1/5}$ borophene and Ag(1×1) single-crystal surface. It is evident from STM and LEED in Figure 5.1, there exist three orientations of borophene on Ag(111) surface cell rotated 120° relative to each other. These three distinct

borophene domains are attributed to the $p6m$ symmetry of the underlying Ag(111) which is imposed on the borophene, which has cmm (or less) symmetry. The XSW measures these three domains simultaneously, which once averaged, have equal fractions of 4-fold and 5-fold boron at a given position when projected onto the Ag($\bar{1}11$), Ag(022), and Ag(020) lattice planes.

Despite the 20 boron atoms with at least 5 distinct positions relative to the Ag(1×1), measured coherent fractions in Table 5.6 were as much as 0.2 for the off-normal reflections. Critically, this indicates definite long-range commensuration between the borophene and Ag(111) substrate ($f_H = 0$ for incommensurate structures), with boron atoms located periodically above particular Ag(111) sites. A Fourier inversion method was used to determine the averaged structure of borophene within the Ag(1×1) [133]. Each measured XSW reflection provides a Fourier component of the 3D atomic density of boron. The summation of orthogonal set of hkl Fourier components with f^H and P^H generates a model-independent 3D map $\rho(\mathbf{r})$, shown in Figure 5.14c,d for B 1s and Ag $3d_{5/2}$.

$$f^H e^{2\pi i P^H} = \int \rho(\mathbf{r}) e^{-i\mathbf{G}_H \cdot \mathbf{r}} d\mathbf{r} \quad (6.2)$$

For the case of the Ag $3d_{5/2}$ yield, the sum of the measured Fourier components gives an atomic density map with the familiar FCC structure, with resolution given by the measured coherent components. The Fourier inversion of the B 1s yields reveals the atomic structure of borophene is highly planar, but with some non-uniformities in the concentration of boron atoms. The areas of highest boron concentration are located directly above the terminating Ag(111) atoms, which indicates that boron atoms prefer to be close to the Ag atoms. However, relating these features to boron atoms proves challenging, because the spacing of Fourier components is much greater than

the projected distance between boron atoms. Model-depending fitting analysis is underway to help resolve this structure.

5.6: Conclusions

Based on the boron 2D lattice determination by LEED, the coordination by XPS, and height by XSW, the R and D phases observed in STM [5,6] are confirmed to be distinct in-plane vacancy configurations as predicted computationally for the $\nu_{1/6}$ and $\nu_{1/5}$ phases [5,49,101]. This conclusion implies that borophene exhibits a unique 2D, vacancy-mediated form of structural degeneracy that is reminiscent of the complexity observed in 3D boron allotropes. This polymorphism within the borophene family further suggests that the properties of borophene and its derivatives can be systematically modified based on substrate interactions, strain, and other parameters. Overall, these results demonstrate that materials without layered bulk allotropes can be induced to form highly planar structures at the 2D limit based purely on non-covalent interactions with metal substrates, thereby establishing a new class of synthetic 2D materials.

Chapter 6: EG/Ge(110) Reconstruction

Understanding and engineering the properties of crystalline surfaces has been critical in achieving functional electronics at the nanoscale. Employing scanning tunneling microscopy, surface X-ray diffraction, and high-resolution X-ray reflectivity experiments, we present a thorough study of epitaxial graphene (EG)/Ge(110) and report a Ge(110) “6×2” reconstruction stabilized by the presence of epitaxial graphene unseen in group-IV semiconductor surfaces. X-ray studies reveal that graphene resides atop the surface reconstruction with a 0.34 nm van der Waals (vdW) gap and provides protection from ambient degradation.

6.1: Introduction

Single-crystal group-IV semiconductor surfaces, as a termination of ideal bulk crystals, draw significant interest for their tendency toward complex and highly anisotropic atomic orbital relaxations [179-185] accompanied by the emergence of energetically distinct surface states [186,187]. Effective surface passivation of group-IV semiconductors ultimately enables neutralization of the unbound orbitals at semiconducting surfaces [188-190], a crucial advancement in large-scale microelectronics fabrication. Most studies, however, have focused exclusively on intrinsic reconstructed surfaces or engineered reconstructions via reactive chemistry. In contrast, the ability to influence chemically homogeneous semiconductor interfaces via van der Waals interactions has not yet been explored.

Graphene synthesized on single-crystal surfaces produces a confined 2D space which stimulates the intercalation of impurity atoms [191,192] and the formation of new 2D materials [4]. This confined interface accommodates a new perspective on semiconductor surface reconstructions by the recent chemical vapor deposition (CVD) synthesis of van der Waals (vdW)

epitaxial graphene (EG) atop atomically flat Ge(110) wafers [81,193]. The chemically inert sp^2 -bonded lattice of graphene [30], protects the Ge surface from ambient while allowing diffusion of atomic species at the encapsulated surface [84,194]. The Ge atoms rearrange into a disordered phase at the ~ 900 °C synthesis temperature, with no evident long-range periodicity [83]. Despite apparently weak vdW bonding, our earlier work [82] showed that interactions at EG/Ge(110) interface led to induced strain and doping of the graphene accompanied by changes in the physical structure of the Ge surface layer. Scanning tunneling microscopy (STM) studies of the annealed EG/Ge(110) interface showed a graphene lattice on top of what appeared to be an ordered 1D reconstruction of the Ge surface atoms with a 2 nm period [82] along the $[\bar{1}12]$ direction. These striped features are also observed in the pristine Ge(110) “16x2” reconstruction, however with a much larger 5 nm period [183-185,195-198], making this EG stabilized Ge structure distinct from those previously reported.

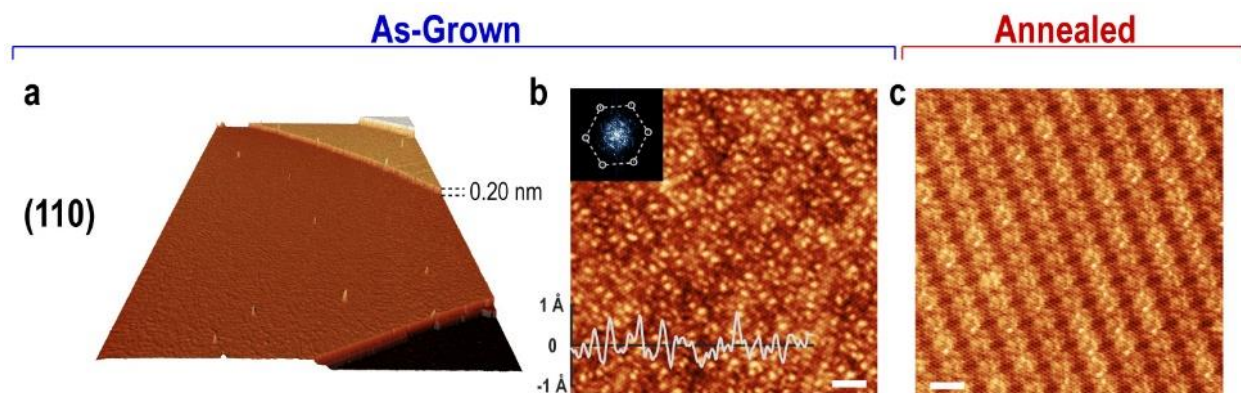


Figure 6.1: STM images of graphene on Ge(110) showing (a) perspective view (size: 500 nm \times 310 nm, $V = 2$ V, $I = 100$ pA), (b) graphene honeycomb lattice atop of as-grown Ge(110) terrace (scale bar = 2 nm, $V = 1.4$ V, $I = 80$ pA). Inset: Fourier transform of (b) with 6-fold symmetry of graphene indicated by dotted hexagon (scale bar = 2 nm $^{-1}$), (c) graphene honeycomb lattice atop annealed 2D reconstruction of the Ge(110) (scale bar = 2 nm, $V = -1$ V, $I = 400$ pA). (Source: adapted from Ref. [82])

Herein, we report a more detailed, higher spatial resolution structural description of this interface by combining grazing incidence X-ray diffraction (GIXD) and high-resolution X-ray reflectivity (XRR) measurements with STM. These highly surface sensitive atomic-scale measurements reveal relaxation of the top-most Ge layers and document the emergence of a surface reconstruction specific to EG/Ge(110). In this particular system, the robust orbital structure of graphene enables the study of vdW interactions at the EG/Ge(110) surface at temperatures approaching the Ge melting point. Upon annealing the EG/Ge(110) surface in ultra-high vacuum (UHV), we show that the presence of the EG introduces a perturbation to the crystalline surface causing it to adopt a specific, long-range order with a Ge(110) “6×2” unit cell, previously unobserved on any group-IV semiconducting surface. Local and global measurements confirm a novel surface 2D reconstruction based on the rearrangement of Ge atoms in the topmost layers of the bulk crystal. Examining the EG/Ge(110) interface with sub-Å resolution verifies a vdW gap between graphene and a partially filled Ge buffer layer. Thus, encapsulation of the Ge(110) surface with EG enables the emergence of an air-stable, ordered Ge surface reconstruction covering nearly the entire Ge(110) surface.

6.2: Methods

6.2.1: Sample Preparation

Ge(110) wafers (University Wafer, resistivity 0.1-0.5 Ω -cm with Ga or Sb dopants) were placed into a horizontal quartz tube furnace (inner diameter of 34 mm) and the system was evacuated to $\sim 10^{-6}$ Torr. The chamber was then filled to atmospheric pressure with 200 sccm of Ar (99.999 %) and 100 sccm of H₂ (99.999 %). The Ge samples were annealed at 910 °C for 30 minutes, after which 3.6-4.6 sccm of CH₄ (99.99 %) was introduced for graphene synthesis. To

terminate growth, samples were rapidly cooled in the same atmosphere used during synthesis by sliding the furnace away from the growth region.

The as-grown graphene on Ge(110) samples were transferred *ex-situ* into UHV ($<10^{-10}$ mbar) and degassed for 1-2 hrs at ~ 400 °C. Annealed samples were heated to ~ 700 °C in UHV for 1-2 hrs. The graphene physical and electronic structure were characterized with STM in an Omicron VT with a base pressure of 10^{-11} mbar. STM measurements were performed on both samples at room temperature using electrochemically etched W tips.

6.2.2: X-ray photoelectron spectroscopy

XPS data were collected *ex situ* using a Thermo Scientific ESCALAB 250X in the KECK II facility at Northwestern University. The ESCALAB is equipped with a monochromatic Al K α X-ray source incident at 45° with a 650 μm spot size. Photoelectrons were collected in a hemispherical energy analyzer with a 15 eV pass energy and 0.1 eV step size. A low-energy electron flood gun was used to compensate for charge accumulation on the sample surface. The Fermi energy was used to calibrate the XPS energy.

6.2.3: Synchrotron X-ray Measurements

High-resolution X-ray measurements were performed at the Advanced Photon Source (APS) station 33ID-D of Argonne National Laboratory. Out-of-plane XRR and in-plane GIXD data were collected for an as-grown EG/Ge(110) sample and then for that same sample after annealing it to 700 °C. Monochromatic 10.00 keV (wavelength $\lambda = 0.1240$ nm) X-rays were focused to $70 \mu\text{m} \times 30 \mu\text{m}$ using a Kirkpatrick-Baez mirror with a flux of 2×10^{11} photons/s. To reduce oxidation, the sample was kept in a He/H atmosphere. Data were collected using a Dectris 100K Pilatus area detector mounted on a Newport 6-circle goniometer. The XRR and GIXD

intensities from the area detector were extracted following established experimental methods provided in Refs. [137,199].

Uncertainties in the extracted XRR and GIXD intensities were computed based on counting statistics, while enforcing 2% and 8% minimum error bars during fitting of the XRR and GIXD data, respectively. The XRR data were fit between $Q_z = 8.4$ to 44.0 nm^{-1} using model-based analysis. The measurement range is reported in the out-of-plane component (Q_z) of the momentum transfer vector $Q = 4\pi \text{Sin}(2\theta/2)/\lambda$, where the scattering angle 2θ is defined as the angle between the incident and scattered wavevectors \mathbf{k}_i and \mathbf{k}_f , respectively.

GIXD data were collected at fixed $\alpha = \beta = 0.2^\circ$ geometry between $Q_{xy} = 3.5$ to 44.0 nm^{-1} ; where α and β are the angles between the surface and wavevectors \mathbf{k}_i and \mathbf{k}_f , respectively. The critical angle for total external reflection of 10.00 keV X-rays from an ideal Ge mirror is $\alpha_c = 0.245^\circ$; in which case the critical scattering vector $Q_c = 0.433 \text{ nm}^{-1}$. Based on the evanescent wave effect for the refraction of the incoming and outgoing X-rays, [200] the scattered X-rays are probing an effective depth of 2.0 nm, i.e., the 10th Ge layer contributes e^{-1} times the top Ge layer [109,200]. All in-plane, allowed and forbidden, bulk Ge reflections were ignored in GIXD analysis. In total, 158 reflections were measured to optimize the in-plane structure using integrated intensity azimuthal ϕ scans. Of the 158 reflections measured, 134 were unique based on symmetry. GIXD integrated peak intensities were background subtracted and corrected for the Lorentz polarization factor following standard convention [199].

6.3: Results

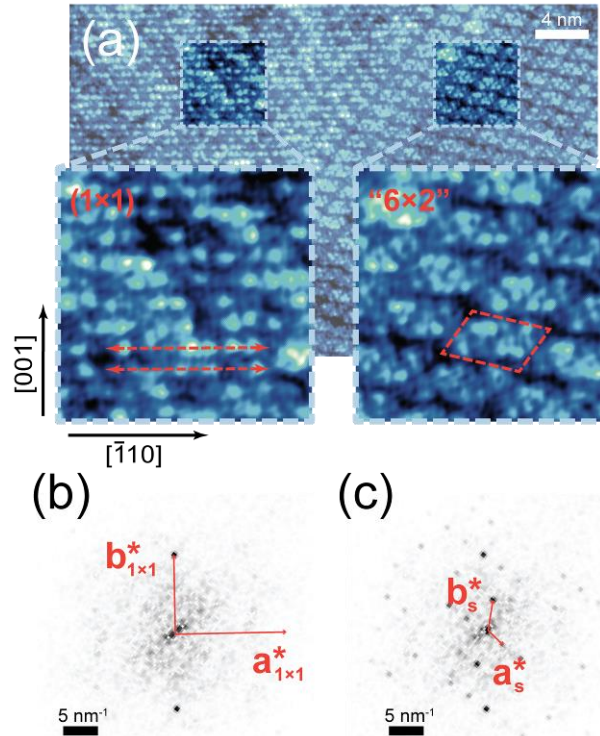


Figure 6.2: STM data of annealed EG/Ge(110) ($V = -1$ V, $I = 400$ pA) with enhanced sensitivity to underlying Ge(110) atomic planes. Left inset: the (01) planes (red) of the unreconstructed Ge(110)-(1x1) phase. Right inset: proposed Ge(110) reconstructed unit cell (red). The superstructure cell is defined with reciprocal space STM data that show lattice points corresponding to (b) the orientation and spacing of $\mathbf{b}_{1 \times 1}^*$ and (c) the Ge(110) “6x2” superstructure with lattice parameters $|\mathbf{a}_s^*| = 3.1 \text{ nm}^{-1}$, $|\mathbf{b}_s^*| = 5.0 \text{ nm}^{-1}$, and $\gamma = 120^\circ$. (STM image provided by B.T. Kiarly)

Upon annealing EG/Ge(110) samples to 700°C under ultra-high vacuum (UHV) conditions, STM images show the formation of an in-plane reorganization of the underlying Ge(110) surface Figure 6.2a,right. In some regions of the samples, the Ge(110) reconstruction can be seen alongside a metastable, unreconstructed Ge(110)-(1x1) phase Figure 6.2a,left. Close examination of the fast Fourier transform of the Ge(110)-(1x1) surface Figure 6.2b confirms a

precise match with the expected periodicity along the [001] bulk Ge direction ($\mathbf{b}_{1x1}^* = 11.2 \text{ nm}^{-1}$), thereby enabling us to impose the crystallographic directions of the Ge crystal onto the STM image. The reciprocal space superstructure unit cell is indicated by the red vectors Figure 6.2c.

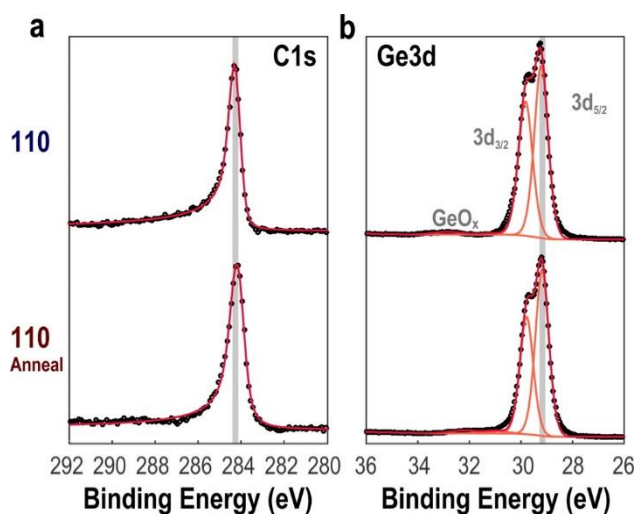


Figure 6.3: Spectra of as-grown and annealed EG/Ge(110) samples (a) C 1s spectra of, raw data (black) Doniach–Sunjic fitted profile (red) vertically offset for clarity, (b) Ge 3d XPS spectra of as-grown and annealed EG/Ge(110) samples. Raw data (black) fitted with symmetric Voigt peaks (orange) centered at energies 29.3, 29.9, and 32.3 for Ge 3d_{5/2}, Ge 3d_{3/2}, and GeO_x, respectively. The sum of the peaks is shown by a red line. (Source: adapted from Ref. [82])

We utilize X-ray photoelectron spectroscopy (XPS) to directly probe both the presence and bonding state of various elements at the interface. Figure 6.3a shows the C 1s spectra for the Ge(110) surfaces before and after annealing. All of the C 1s spectra were fit using the Doniach–Sunjic profile for metallic surfaces, reproducing the asymmetric profile characteristic of graphite and graphene [144]. The fitted singularity index α of 0.15 is consistent with previous reported values for the case of graphite by Wertheim [201] and Cheung [202]. The XPS spectra confirm that C present in the system is isotopically sp² bonded. Furthermore, shifts in the C 1s peak position between the Ge(110) samples are consistent with the doping observed in the Raman spectroscopy [82]. The Ge 3d peak displays similarly pure chemical characteristics, with all samples showing

the characteristic $3d_{5/2}$ and $3d_{3/2}$ doublet of elemental germanium. A minor GeO_x peak is present in the Ge(111) samples, pointing to a minor degree of surface oxidation likely due to the presence of grain boundaries in the graphene. Significantly, all spectra show an absence of Ge–C bonds, confirming the chemical integrity of the graphene before and after annealing.

Table 6.1: Results of model dependent fit to XRR data listing vertical height (Z), layer occupancy fraction (Θ), and distribution width (σ) fitting parameters for as-grown and annealed “6×2” Ge(110). Z is vertical displacement relative to the top-most Ge(110) bulk-like atomic plane, Θ is in units of bulk-like 2D atomic densities (8.8 nm^{-2} for Ge(110) planes and 38.2 nm^{-2} for EG). Uncertainty of 3 standard deviations is given in parentheses.

Layer	As-Grown EG/Ge(110)			Annealed EG/Ge(110) “6×2”			
	Z (nm)	Θ	σ (nm)	Z (nm)	Θ	σ (nm)	
Ge ₁	0.201(2)	0.98(3)	0.0068(6)	0.201(2)	0.99(3)	0.0075(4)	
Ge ₂	0.404(2)	0.95(6)	0.008(1)	0.402(2)	0.93(8)	0.008(1)	
Ge ₃	0.601(1)	0.87(8)	0.017(5)	0.600(2)	0.9(2)	0.017(7)	
Ge ₄	Bulk	0.81(1)	0.8(2)	0.02(1)	0.80(2)	0.6(3)	0.01(2)
	Buckled	0.85(8)	0.1(1)	†0.022	0.85(4)	0.2(2)	†0.025
Ge ₅	Buffer	0.96(2)	0.6(1)	0.043(3)	0.96(2)	0.7(1)	0.03(2)
EG ₁	1.30(1)	0.9(1)	0.024(4)	1.30(1)	0.9(1)	0.021(9)	
EG ₂	1.64(1)	0.4(1)	0.029(9)	1.64(3)	0.4(1)	†0.036	

†Fixed parameter value.

The electron density profile along the [110] direction for the EG/Ge(110) interface was determined from a model-dependent fit to the specular reflectivity data Figure 6.4. The XRR data (Figure 6.4a) show orders-of-magnitude changes in scattered intensity as compared to the ideal bulk terminated surface, indicating distinct positions for the surface Ge and overlaying graphene. The peaks at 32 nm^{-1} and 64 nm^{-1} are consistent with Bragg scattering from single-crystal Ge(220) and Ge(440) planes with characteristic 0.200 nm atomic plane spacing. The most notable deviations from the XRR of the ideal Ge(110) bulk crystal (Figure 6.4a) are the peaks near $Q_z =$

18 and 54 nm^{-1} , which correspond to 1st and 3rd order diffraction peaks from the 0.35 nm vdW gap periodicity that exists between EG layers and the EG-Ge buffer layer. The dips at $q_z = 22, 46,$ and 58 nm^{-1} correspond to the 0.04 nm inward relaxation of the Ge buffer layer towards the Ge(110) bulk planes. The EG/Ge(110) 1D model system was generated following established XRR analysis methods in Refs. [138,203,204]. The model consists of a semi-infinite bulk Ge lattice, upon which Ge and EG layers were added to ultimately achieve a $\chi^2 \sim 10$ best fit for as-grown and annealed EG/Ge(110).

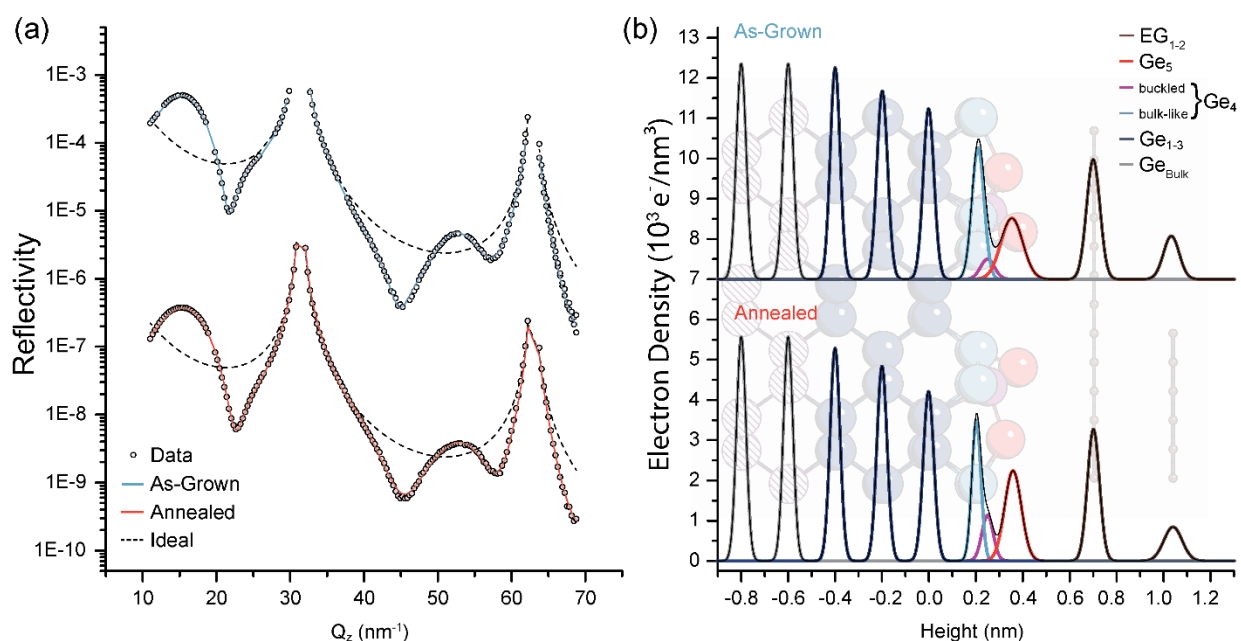


Figure 6.4: XRR data of EG/Ge(111) as-grown (top) and annealed “6×2” (bottom) samples, corresponding electron density, and model structure. (a) High-resolution XRR data and model fit. The dashed line is the simulated XRR for an ideal bulk terminated Ge(110) surface. (b) The model fit derived electron density profile along the [110] direction for the EG/Ge(110) structure. In the background is shown a side-view of a ball-and-stick representation of the model with coverages consistent with the electron density profile.

The model fit (Figure 6.4b) of the Ge(110) interface is constructed from 5 Ge layers with 6 distinct vertical Ge atomic positions and an EG layer with a partial EG bilayer. The best-fit positions (Z), occupancies (Θ), and distribution widths (σ) of the EG/Ge(110) for both the as-grown and “6x2” reconstructed XRR data are enumerated with 3 sigma confidence in Table 6.1. The first three layers of Ge (Ge_{1-3}) atop the semi-infinite Ge crystal remain at bulk positions (0.200 nm), but with a gradual increase in vacancy concentrations and distribution width broadening compared to bulk Ge. The fourth layer (Ge_4) and fifth layer (Ge_5) of Ge deviate substantially from bulk, forming a relaxed Ge complex consisting of a partially buckled layer underneath an inward relaxed surface layer, which relaxes further upon annealing. For the fourth layer of the as-grown interface, $80 \pm 20\%$ of the Ge atoms sit at the height of bulk Ge(110) planes, with the remaining 10% buckled outward 0.04 ± 0.08 nm towards the EG. The inclusion of a buckled subsurface layer has been used previously in simulated pristine uncovered Ge(110) reconstructions and helps to stabilize the topmost Ge buffer layer (Ge_5) [183,184]. A $60 \pm 10\%$ occupancy Ge buffer layer (Ge_5) is relaxed 0.05 ± 0.01 nm inward from its bulk position. The nearly 50% vacancy concentration in Ge_5 allows in-plane diffusion of the Ge, enabling the reorganization of the surface into the “6x2” superstructure upon annealing to 700 °C under UHV conditions. The annealed “6x2” EG/Ge(110) shows a sharpening of the interface (~ 0.01 nm) accompanied by diffusion of Ge into the reconstructed buckled and surface layers. When compared to other models for uncovered Ge(110) surface reconstructions [183,184,196,197], the model Ge(110) vertical structure shares key commonalities, namely broadening of the bulk Ge(110) layers, a buckled surface layer, and a partially occupied topmost layer shifted from its ideal position toward the Ge(110) bulk.

Despite the considerable deviation of the relaxed Ge surface vertical profile from an unreconstructed ideal Ge(110) surface, the overlying EG appears pristine and unaffected by annealing. Both prior to and after annealing, the first layer of graphene (EG₁) is located 0.34 nm above the (Ge₅) with approximately 90±10% surface coverage, while a 40±10% coverage bilayer (EG₂) sits 0.34 nm above EG₁. The bilayer improved the χ^2 value by ~10. The improvement in the fit (Figure 6.4a) was most notable at the 18 nm⁻¹ peak. The graphene spacing closely matches the gap of EG and other vdW bonded structures, suggesting that EG weakly interacts with the Ge surface. The EG displacement (0.34±0.04 nm) matches previous STM measurements (0.35 nm) of EG/Ge(110) [83]. The first layer EG has a measured σ of 0.024±0.004 nm, which is ~ 0.02 nm narrower than the underlying Ge buffer layer and comparable to those measured for EG on SiC [14]. The EG is highly planar, effectively bridging the corrugations in the “6×2” Ge(110) surface.

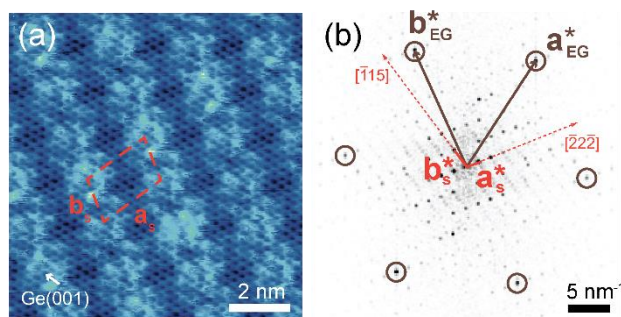


Figure 6.5: Lattice of annealed EG/Ge(110) (a) STM showing the characteristic “6×2” reconstruction with lattice parameters of \mathbf{a}_s and \mathbf{b}_s underneath EG ($V = -1$ V, $I = 400$ pA). The EG hexagonal basis vector lies along the Ge [001] direction. (b) Reciprocal space STM data displaying relative orientations of Ge(110) “6×2” in red and EG in brown. (STM image provided by B.T. Kiarly)

STM images of the annealed EG/Ge(110) samples show the formation of an in-plane reorganization of the underlying Ge(110) surface (Figure 6.5a). The lateral periodicity of the EG/Ge(110) surface is apparent from FFT analysis of the STM data. The reciprocal space “6×2”

unit cell is indicated by the red vectors alongside the epitaxial graphene (Figure 6.5b). To study the Ge(110) “6×2” atomic rearrangement over large-areas and with enhanced Ge sensitivity, GIXD was performed on both the as-grown and annealed EG/Ge(110). GIXD maxima of the as-grown EG/Ge(110) match expected Bragg peaks from the Ge(110) bulk crystal. The annealed EG/Ge(110) GIXD data show additional in-plane diffraction maxima. These maxima (Figure 6.6a)

appear at 2D superstructure reciprocal lattice points $h_s k_s$ defined by basis vectors $\mathbf{a}_s^* = \frac{1}{6} \mathbf{G}_{\bar{1}\bar{1}\bar{1}}$ and

$\mathbf{b}_s^* = \frac{1}{12} \mathbf{G}_{\bar{1}\bar{1}\bar{5}}$, where \mathbf{G}_{hkl} are reciprocal lattice vectors for diamond-cubic bulk Ge with lattice

constant 0.5658 nm. The real space “6×2” unit cell basis vectors \mathbf{a}_s and \mathbf{b}_s have lengths 2.08 nm and 1.39 nm along the $[\bar{5}\bar{5}\bar{2}]$ and $[\bar{1}\bar{1}\bar{2}]$ directions, respectively, with angle $\gamma = 70.5^\circ$. The

transformation matrix

$$\frac{1}{12} \begin{pmatrix} 2 & \bar{2} \\ 1 & 5 \end{pmatrix} \begin{pmatrix} \mathbf{a}_{1\times 1}^* \\ \mathbf{b}_{1\times 1}^* \end{pmatrix} = \begin{pmatrix} \mathbf{a}_s^* \\ \mathbf{b}_s^* \end{pmatrix} \quad (6.1)$$

relates the reciprocal lattice basis vectors of the 2D superstructure to the (1×1) basis vectors of the Ge (110) bulk-terminated surface. In real space, the superstructure can be properly referred to in

matrix notation as $\begin{pmatrix} 5 & \bar{1} \\ 2 & 2 \end{pmatrix}$ or in Wood notation as Ge(110) “6×2”, being a non-rectangular

superstructure of the rectangular Ge(110)-(1×1) basis with $|\mathbf{a}_s| = \frac{1}{2} d_{\bar{5}\bar{5}\bar{2}}$ and $|\mathbf{b}_s| = d_{\bar{1}\bar{1}\bar{2}}$.

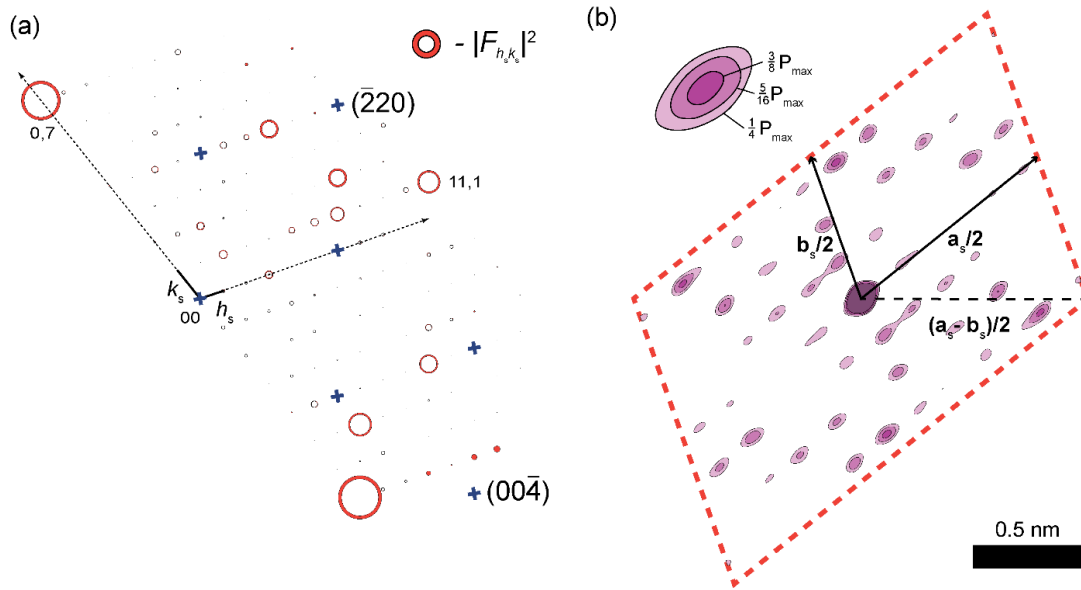


Figure 6.6: GIXD surface characterization of EG/Ge(110). (a) GIXD measured values of $|F_{h_s k_s}|^2$ in 2D reciprocal space indexed in h_s and k_s of the Ge(110) “6×2” basis. The measured values are proportional to the areas of the hollow circles. The statistical error (red) is indicated by the perimeter width of each circle. Bulk Ge(110) reflections are marked with an x (blue). (b) The contour map of the direct space Patterson function for the Ge(110) “6×2” surface from eq. 6.2. All peaks with values greater than $1/4$ the origin peak are shown.

The areas of the hollow black circles in Fig. 3(a) are proportional to the values of $|F_{h_s k_s}|^2$, which are derived from the measured in-plane ($Q_z = 0$) integrated scattered intensities at each Ge 2D superstructure peak. $F_{h_s k_s}$ is the 2D structure factor [109], which is sensitive to the atomic arrangement of the Ge atoms within the “6×2” unit cell. Directly extracting Ge positions through the complex Fourier inversion of $F_{h_s k_s}$ is not possible due to the missing phase of $F_{h_s k_s}$. Instead, we use a Fourier inversion of the set of 134 symmetry inequivalent $|F_{h_s k_s}|^2$ values that leads to a model-independent 2D map of displacement vectors between Ge atoms in the “6x2” reconstructed surface. This 2D Patterson method is a viable first step in solving surface structures with several

symmetry-inequivalent atomic sites from GIXRD data as previously demonstrated [132,205,206].

The 2D electron density correlation function

$$P(x, y) = \frac{1}{A} \sum_{h_s, k_s} |F_{h_s k_s}|^2 \cos[2\pi(h_s x + k_s y)] \quad (6.2)$$

was used to generate the measured 2D Patterson map in Fig. 3(b), where x and y are the fractional coordinates of the unit cell with area A . The peak at the origin is the sum of the self-correlation of all displaced Ge atoms at the surface. The surround peaks represent vector displacements between atoms on the surface. By applying graph theory, the ~ 11 symmetry inequivalent non-origin strong peaks (max value $> 0.3 P_{\max}$) come from a minimum of 4 or 5 distinct high-density regions (i.e. clusters of Ge atoms) for a non-centrosymmetric or centrosymmetric unit cell, respectively. The ratios of Patterson peak values between these strong peaks and the peak at the center of the unit cell is proportional to the overall number of Ge atoms with this displacement. The XRR derived model [Fig. 1(b)] shows that the topmost Ge layer is comprised of 16 ± 2 Ge within the “6x2” unit cell compared to 24 atoms in the same area within a bulk-like (110) Ge layer. The strongest non-origin peaks in the Patterson map show $\sim 1/4$ the value of the center peak, indicating that these Ge displacements are experienced by ~ 4 Ge in the “6x2” surface unit cell. The high concentration of peaks along the $\mathbf{a}_s - \mathbf{b}_s$ direction suggests the formation of ordered Ge clusters underneath the graphene displaced relative to each other along $(\mathbf{a}_s - \mathbf{b}_s)$ [shown by a dashed line in Figure 6.6b. A similar feature can be seen in STM (Figure 6.2a) and matches observations of pentagon-like rings in the well-studied “16x2” reconstruction of pristine Ge(110) and Si(110) in UHV [183,184,195,196,207-209]. The prominent peaks along the \mathbf{b}_s or $[\bar{1}12]$ direction match the periodic corrugated ribbons seen in the STM of graphene atop the EG/Ge(110) “6x2”

reconstruction (Figure 6.5a). Here we are resolving displacements between individual clusters of Ge atoms. To resolve the individual atomic positions would require a much larger set of GIXD peaks or a GIXD – theory combined approach.

6.4: Conclusions

In summary, we used STM, GIXD, and XRR data to reveal the formation of a previously unidentified Ge(110) “6×2” reconstruction upon annealing, stabilized by weak vdW interactions of EG 0.34 ± 0.04 nm atop a reordered Ge(110) surface. Through model-independent analysis of GIXD and STM, we show that annealing EG/Ge(110) leads to a reorganization of the Ge buffer layer into Ge clusters positioned along the $[\bar{1}12]$ bulk Ge direction. XRR reveals a vertical relaxation of a Ge surface and verifies the integrity of the vdW gap between the Ge and overlaying graphene after the formation of the Ge(110) “6×2” reconstruction. The graphene atop the Ge further acts as an encapsulating layer, protecting the Ge(110) surface in ambient. This non-destructive approach for controlling atomic surface reconstructions with vdW materials represents a methodology for engineering single-crystal surfaces and interfaces.

Chapter 7: EG/SiC(0001) Heterostructures

Atomically thin MoS₂/graphene heterostructures are promising candidates for nanoelectronic and optoelectronic technologies. When synthesized on epitaxial graphene (EG) on SiC, these heterostructures exhibit high electronic quality and wafer-scale processability owing to commensurate growth enabled by van der Waals epitaxy. We examine here the thickness-controlled van der Waals epitaxial growth of MoS₂ on EG *via* chemical vapor deposition, giving rise to transfer-free synthesis of a two-dimensional heterostructure with registry between its constituent materials. The rotational commensurability observed between the MoS₂ and EG is driven by the energetically favorable alignment of their respective lattices and results in nearly strain-free MoS₂, as evidenced by synchrotron X-ray scattering.

7.1: Introduction

Vertical heterostructures composed of stacked two-dimensional (2D) materials allow the exploration of fundamental interfacial interactions and novel electronic functionality. The MoS₂/graphene heterostructure [107,210] is a model 2D metal/semiconductor heterostructure which uses the full potential of both materials due to complementary carrier mobilities and optical responsivities [211]. The properties of MoS₂/graphene heterostructures depend strongly on the underlying substrate and the graphene synthesis technique. Controlling rotational alignment on a large-scale ensures 2D materials will have reproducible properties on a wafer-scale. Epitaxial graphene (EG) grown on SiC by the preferential thermal desorption [92,212,213] produces uniform large-area synthesis of graphene unperturbed by the underlying substrate, particularly after the decoupling of the buffer layer by post-annealing in hydrogen [191,214]. Furthermore, the

functionality of these heterostructures could be tailored through atomic intercalation of the EG/SiC buffer layer [215-217].

The atomic-scale electronic and structural properties of MoS₂/EG heterostructures have not been thoroughly established. Towards these ends, we report here the rotationally commensurate growth of atomically thin MoS₂ crystals on EG by van der Waals epitaxy. We investigate the electronic and structural properties of the resulting MoS₂/EG heterostructures with synchrotron X-ray reflectivity (XRR) and grazing incidence X-ray scattering (GIXS) as part of a comprehensive suite of methods including atomic force microscopy (AFM), ultra-high vacuum (UHV) scanning tunneling microscopy and spectroscopy (STM/STS), *in situ* X-ray photoelectron spectroscopy (XPS), and Raman spectroscopy, which are discussed further in our collaborative work [106]. These X-ray techniques are then extended to mixed dimensional vdW heterostructures, which integrate graphene with 0D fullerenes [32], 1D nanotubes[218], and 3D crystals [23] to form mixed-dimensional vdW heterostructures [219].

7.2: Methods

7.2.1: Synthesis of MoS₂

High-quality EG was grown on a 9 mm × 5 mm n-type 4H-SiC(0001) wafer (Cree Inc.). The wafer was sonicated successively in acetone and isopropyl alcohol (IPA) for 10 minutes each. Subsequently, the substrates were transferred to an ultra-high vacuum (UHV) chamber ($\sim 5 \times 10^{-10}$ Torr) where they were degassed at 550 °C for ~12h. EG was grown on the Si face of the wafer by direct heating and thermal desorption of Si atoms at 1270 °C for 20 minutes (with temperature ramping rate of 100 °C/min and cooling rate of 50 °C/min).

To produce MoS₂ on EG, Molybdenum trioxide (MoO₃, 99.98% trace metal Sigma Aldrich) was placed in the middle of the hot zone of a Lindberg/Blue 1'' quartz tube furnace in an alumina boat 2.5 cm upstream of a 5 mm × 9 mm EG substrate (graphitized Si face is facing up). The sulfur powder (Sigma Aldrich) in an alumina boat was placed 30 cm upstream of the MoO₃ boat under a PID temperature controlled heating belt. The tube was initially pumped to a base pressure of ~50 mTorr and purged with Ar gas to 400 Torr. During the anneal prior to the reaction and during the reaction itself, the pressure was kept constant at 43 Torr (to yield mostly monolayer MoS₂ crystals) using a needle valve controller and Ar carrier gas flowing at 25 sccm. The MoO₃ and EG substrate were annealed for 20 min at 150 °C (with a 5 min ramp to 150 °C from room temperature) to eliminate residual water and physisorbed contaminants in the tube and on the substrate. Subsequently, the furnace was heated to a maximum temperature of 800 °C at a rate of 12 °C/min. Once the target temperature was reached, the furnace was kept at 800 °C for 20 min and cooled down naturally to room temperature. Concurrently, the sulfur was annealed under the same inert conditions for 49 min at 50 °C (with 5 min ramp to 50 °C from room temperature) and brought to a maximum temperature of 140 °C at a rate of 4 °C/min. The sulfur ramp to 140 °C began when the furnace was approximately at 500 °C. The sulfur was then kept at the maximum temperature for 23 min.

To form the self-assembled monolayer (SAM) of octadecylphosphonic acid (OPA), 1-2 drops of OPA solution were spin-coated at 4000 rotations per minute for 1 minute onto the EG substrate. EG was stored in the UHV chamber until immediately before the spin coating step to avoid contamination. The sample was then heated to 85 °C for 10 minutes to evaporate excess solvent and OPA [220]. Finally, aluminum, iron, or platinum (purity ~99.99%, Lesker) were

thermally evaporated under high vacuum conditions ($\sim 5 \times 10^{-6}$ Torr, NANO 38, Lesker) at a rate of ~ 0.2 Å/min (monitored by a quartz microbalance) onto the OPA SAM.

7.2.2: GISAXS/GIWAXS

The GIWAXS data of MoS₂/EG/SiC were collected at sector 12-ID-C at the Argonne National Laboratory Advanced Photon Source. The 23.5 keV monochromatic X-ray beam was defined using slits of $50 \mu\text{m} \times 2 \text{mm}$ to have a $5 \text{mm} \times 2 \text{mm}$ footprint on the sample at incident angle $\alpha = 0.14^\circ$. The incident flux was 4×10^{12} photons/s. As depicted in Figure 7.2a, a 100K Pilatus Area Detector was mounted on a rotating ν -arm positioned at approximately 354 mm from the sample to collect the GIWAXS signal. Data within $q = 2.2 \text{ \AA}^{-1}$ to 4.8 \AA^{-1} in Figure 7.2 was collected at $\nu = 10.262^\circ$ relative to the direct beam. The sample was kept under a helium environment and placed on a ϕ rotation stage.

The 33-ID-C line was used to collect high-resolution grazing incidence X-ray scattering and diffraction data from the bulk MoS₂ single-crystal and MoS₂/EG samples. Monochromatic 10 keV X-rays were focused to $70 \mu\text{m} \times 30 \mu\text{m}$ using a horizontal Kirkpatrick-Baez mirror with a flux of 2×10^{11} photons/s. Data were collected using a Dectris 100K Pilatus area detector mounted on a Newport 6-circle goniometer. The reciprocal space map in Figure 7.2b was generated using the Ewald sphere construction method, wherein pixels from $q_z = 0.08 \text{ \AA}^{-1}$ to 0.12 \AA^{-1} were projected onto a 2D reciprocal space map using interpolation plots in Mathematica. Peaks were fit using the Gaussian fitting function in MATLAB.

GIXS measurements of OPA on EG were performed *ex situ* at sector 8-ID-E of the Advanced Photon Source at Argonne National Laboratory. The GIXS setup employs simultaneous grazing incidence small- and wide-angle X-ray scattering (GISAXS/GIWAXS) detectors. GISAXS data

was collected for $|Q_{\max}| < 2 \text{ nm}^{-1}$ with a Pilatus 1M detector and GIWAXS data was collected in regions for $Q > 2 \text{ nm}^{-1}$ with a Pilatus 100K offset horizontally from the direct beam. Sector 8-ID-E employed polarized monochromatic 7.35 keV x-rays through a beam defining slit $40 \mu\text{m}$ by $500 \mu\text{m}$ with incident photon flux of $\sim 10^{11}$ photons/s. Samples were mounted on a ϕ -rotatable vacuum stage and 100 s exposures were taken every 1.0° . The incident angle was set at $\alpha = 0.26^\circ$, approximately 70% of the critical angle of the SiC substrate. The GISAXS experimental geometry was calibrated using a silver behenate standard. The data were analyzed using the NIKA software package from Argonne along with MATLAB and Mathematica fitting routines.

7.2.3: XRR

7.3: High-resolution X-ray measurements were performed at the Advanced Photon Source (APS) station 33ID-D of Argonne National Laboratory. XRR were collected for the as-grown EG/SiC(0001) and MoS₂ on EG/SiC(0001) samples. Monochromatic 10.00 keV (wavelength $\lambda = 0.1240 \text{ nm}$) X-rays were focused to $70 \mu\text{m} \times 30 \mu\text{m}$ using a Kirkpatrick-Baez mirror with a flux of 2×10^{11} photons/s. To reduce oxidation, the sample was kept in a He/H atmosphere. Data were collected using a Dectris 100K Pilatus area detector mounted on a Newport 6-circle goniometer. The XRR intensities from the area detector were extracted following established experimental methods provided in Refs. [137,199].

7.4: Results

7.4.1: In-plane structure

CVD growth of MoS₂ on EG is performed at a variety of conditions in order to tune and optimize the MoS₂ film thickness. Figures 7.1b,c are AFM topography and phase images, respectively, of MoS₂ grown on EG at 43 Torr. Figure 7.1d extracts the edge orientations of the

MoS₂ triangles shown in Figure 7.1b by plotting a line along one edge of each triangle. A large majority of the triangles have parallel edges as indicated by the blue lines, while a few triangles, indicated in red, have edges rotated by 30°. The rare occurrence of a third rotational orientation of a MoS₂ triangular domain is shown in pink. From this analysis, it is apparent that there are two predominant types of azimuthal registration of MoS₂ on EG. This crystal orientation alignment is attributed to van der Waals epitaxy [52], which accommodates the large lattice mismatch (~28%) between graphene and MoS₂, as will be further discussed below.

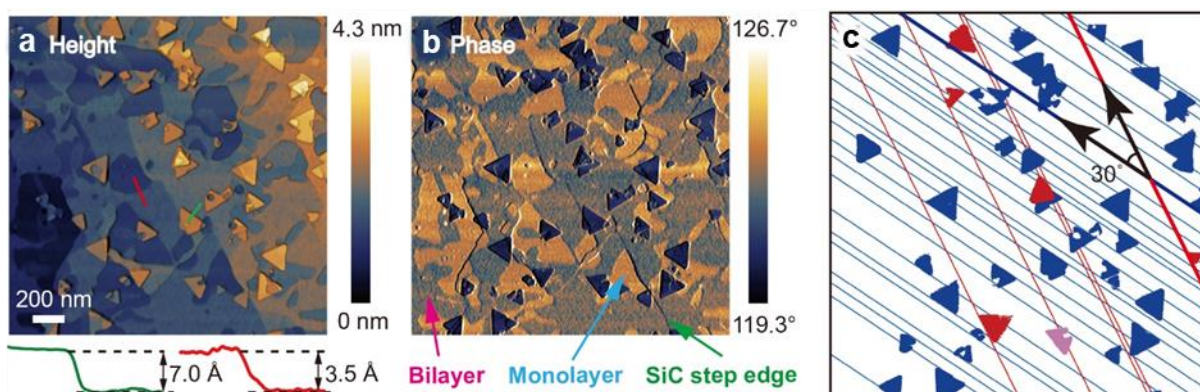


Figure 7.1: CVD-grown MoS₂ on EG grown at 43 Torr. (a) AFM height and (b) phase images of MoS₂/EG. Line profiles show monolayer MoS₂ (green) and graphene (red) thicknesses. The contrast between bilayer and monolayer regions of EG is more obvious in the phase image. (c) Extraction of edge orientations of MoS₂ crystals in (a) showing two predominant registrations of MoS₂ on EG.

To verify that these local AFM and STM observations persist over the entire sample, synchrotron grazing incidence wide-angle X-ray scattering (GIWAXS) is employed to investigate the van der Waals epitaxy of MoS₂ on EG. A schematic of GIWAXS is shown in Figure 7.2a and experimental details are outlined in the Methods section. In GIWAXS, the incident X-ray beam is at incident angle $\alpha = 0.14^\circ$, slightly below the critical angle of total external reflection of the substrate. The out-of-plane angle β and in-plane angle 2ϕ define the position at which the scattered

X-ray wave vector \mathbf{k}_f intersects the plane of the 2D detector. The q_{xy} 2D reciprocal space map of the MoS₂/EG/SiC structure projected from $q_z = 0.08 \text{ \AA}^{-1}$ to 0.12 \AA^{-1} is shown in Figure 7.2b with first order spots of MoS₂, EG, and SiC identified. The blue, orange, and magenta arrows indicate the reciprocal lattice vectors \mathbf{b}^* for MoS₂, EG, and SiC, respectively. As seen by the reciprocal space points, the reciprocal lattices for MoS₂ and EG are aligned, whereas SiC has a well-known 30° rotation with respect to EG [221]. This observation indicates that the majority of the MoS₂ crystals are epitaxially grown along the EG lattice direction with matching six-fold symmetry, confirming the symmetry inferred from AFM (Figure 7.2). The real-space structure reconstructed for such aligned MoS₂ growth is shown in Figure 7.2c, where the two MoS₂ triangles represent the preferred orientations in the epitaxial MoS₂/EG heterostructure. Projected first order MoS₂ and SiC peaks onto ϕ are included in Figure 7.2d to examine the angular distribution. The relative angle between the MoS₂ and SiC lattices is indeed $30^\circ \pm 0.3^\circ$, which is a much narrower azimuthal distribution than that of CVD MoS₂ grown on sapphire [222]. The full-width-at-half-maxima of the first order MoS₂, EG, and SiC peaks as a function of ϕ are 0.7° , 0.5° , and 0.05° (limited by X-ray optics), respectively, which confirms that the MoS₂ is in good registry with EG.

Figure 7.2e shows the scattered intensity from the 2D reciprocal space map of Figure 7.2b collected along q_y at $q_x = 0$. The real-space lattice constants calculated for MoS₂, EG, and SiC are $3.16 \pm 0.01 \text{ \AA}$, $2.46 \pm 0.01 \text{ \AA}$ and $3.07 \pm 0.01 \text{ \AA}$, respectively. To gain more insight into the structure of MoS₂ on EG, in-plane GIXD of MoS₂/EG and bulk MoS₂ was performed (Figure 7.2). The resulting lattice constants of MoS₂/EG and bulk MoS₂ are $3.160 \pm 0.005 \text{ \AA}$ and $3.159 \pm 0.006 \text{ \AA}$, which indicate a relaxed in-plane structure of MoS₂ on EG similar to its bulk counterpart. The lack of in-plane strain in the synthesized MoS₂ 2D crystals can be explained by total strain relaxation

in the van der Waals gap, analogous to a buffer layer alleviating the strain in conventional epitaxy [223].

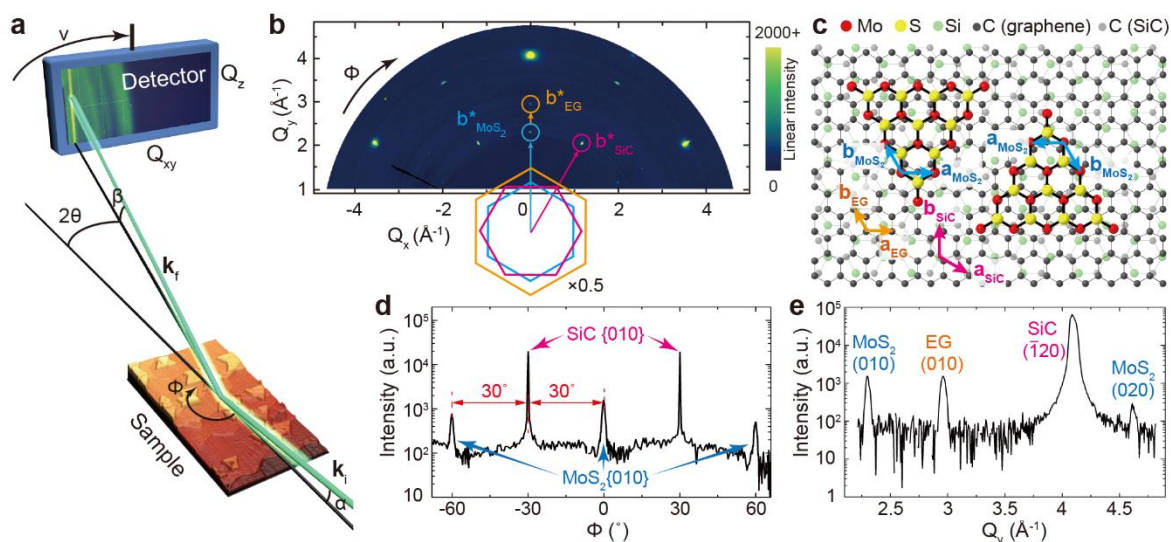


Figure 7.2: Rotationally commensurate van der Waals epitaxy of MoS₂ on EG. (a) Schematic of GIWAXS measurement. (b) Q_{xy} 2D reciprocal space map of MoS₂/EG projected from $Q_z = 0.08 \text{ \AA}^{-1}$ to 0.12 \AA^{-1} by synchrotron GIWAXS. The \mathbf{b}^* reciprocal space vectors are indicated by arrows. (c) Real-space model of the MoS₂/EG heterostructure with MoS₂ lattice aligned with that of EG. (d) Projected first order peaks of MoS₂ and SiC onto ϕ showing sharp distributions. (e) Referring to (b), in-plane scattered intensity along Q_y direction at $Q_x = 0$. The determined real-space lattice constants of MoS₂, EG, and SiC are $3.16 \pm 0.01 \text{ \AA}$, $2.46 \pm 0.01 \text{ \AA}$, and $3.07 \pm 0.01 \text{ \AA}$, respectively.

As indicated by the red MoS₂ triangles in Figure 7.2d, there is a secondary, less preferred registration between MoS₂ and EG, where MoS₂ lattice is rotated by 30°. To examine the relative amount of 30° rotated growth, GIWAXS data of the MoS₂(010) peak taken along the EG[010] direction (aligned growth, blue) and the SiC[010] direction (30° rotated growth, red) are shown in Figure 7. The integrated intensities of these two peaks are 2.6×10^5 and 4.2×10^4 , respectively. This indicates that the amount of MoS₂ with lattice 30° rotated from the EG lattice is $14 \pm 4\%$ of the total and the aligned growth is dominant ($86 \pm 4\%$). This large-area GIWAXS result is consistent with the orientation distribution of MoS₂ domains shown in the AFM images in Figure 7.1. Thus,

in Figure 7.2d, we attribute the majority blue MoS₂ triangles to aligned growth, and the minority red triangles to 30° rotated growth. The inset of Figure 7.3 shows the schematic of these two registrations, where the blue, black and red arrows indicate the armchair directions of aligned MoS₂, EG and 30° rotated MoS₂, respectively. These two growth orientations have also been observed previously for MoS₂ grown on sapphire [222,224]. Rare deviations in the preferred orientations, such as the pink MoS₂ crystal domain shown in Figure 7.1d, indicate lack of registry of the MoS₂ domain with the EG and can be attributed to local disturbances in the substrate surface. These occurrences were not frequent enough to produce detectable scattered X-ray intensity. The in-plane analysis of MoS₂ on EG/SiC reveals multiple orientations of MoS₂ flakes and selective nucleation on step edges. While the pristine electronic properties and lack of in-plane strain are strong indications of a vdW gap between MoS₂ and EG, Direct measurements of the interface between MoS₂ and EG are needed to verify the integrity of the vdW gap.

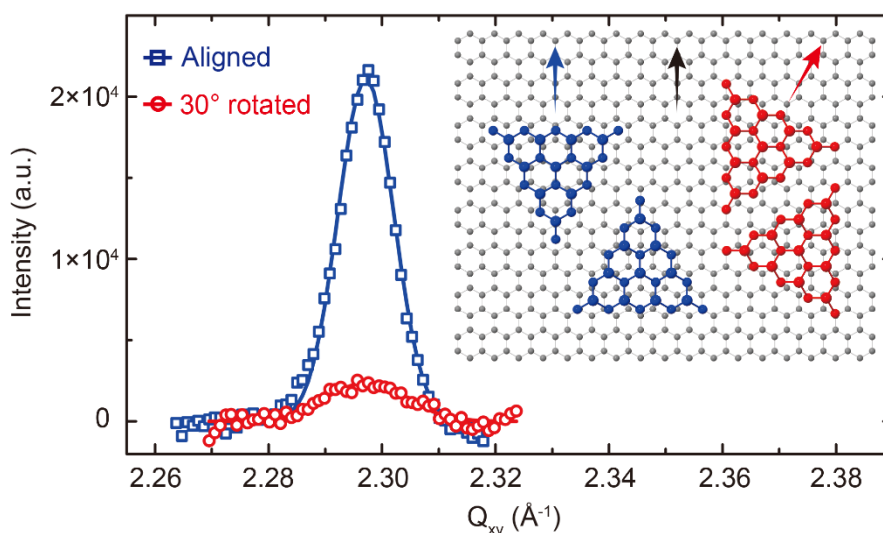


Figure 7.3: Examination of the growth orientation of MoS₂. GIWAXS data of the MoS₂(010) peak taken along the EG[010] direction (aligned growth, blue) and the SiC[010] direction (30° rotated growth, red). The integrated intensities of these two peaks are 2.6×10^5 and 4.2×10^4 , respectively. Inset: schematic of the two growth orientations of MoS₂ on EG. The armchair directions of MoS₂

from aligned (blue) and 30° rotated (red) growth are indicated by the blue and red arrows, respectively. The black arrow indicates the armchair direction of EG.

7.4.2: Vertical Model

XRR was employed to probe the interface between MoS₂ and the underlying EG/SiC. Generating a model from X-ray reflectivity, being an ensemble averaging of all layered structures on the sample surface, necessitates the use of a model which captures all these layered structures simultaneous, reflected in the measured XRR data. The model consists of layers of distinct elements described by their height above the semi-infinite SiC(0001) surface, z , fractional monolayer occupancy, Θ , and distribution width, u . Following previous XRR analysis of EG/SiC [134], the SiC substrate contained four relaxed adlayers of alternating C and Si atop a semi-infinite bulk 4H-SiC(0001) (Si-terminated) substrate. Three overlaying graphene layers (EG₁₋₃) rested atop an EG₀ buffer layer consisting of two distinct C positions. To account for the CVD grown MoS₂ atop the few-layer graphene on SiC(0001), six MoS₂ layers were added to the EG/SiC system, of which three MoS₂ layers [(MoS₂)₁₋₃] were assumed to be sitting atop EG₁₋₃ with and vdW gap and the other three MoS₂ layers reflect the fractional coverage of bilayer MoS₂ seen in AFM [106].

Physical constraints were applied to the parameters (z , Θ , and u) to obtain a reasonable model fit. The stoichiometry of each MoS₂ layer was fixed, so a single occupancy Θ parameter was used for one Mo and surrounding two S layers in a single MoS₂ layer. The covalent interactions between Mo and S were assumed to be bulk-like (Mo-S vertical separation = 1.5 Å) and identical for each MoS₂ layer. The occupancy for a given (MoS₂) _{n} layer was assumed to be no greater than the exposed surface of the corresponding EG _{n} layer, where the fraction of exposed surface is given by $\Theta_n - \Theta_{n+1}$ for EG _{n} . Likewise, physically related parameters were described with a single viable to reduce the large number of free parameters (~192) used to describe this system.

7.4.3: Vertical Structure

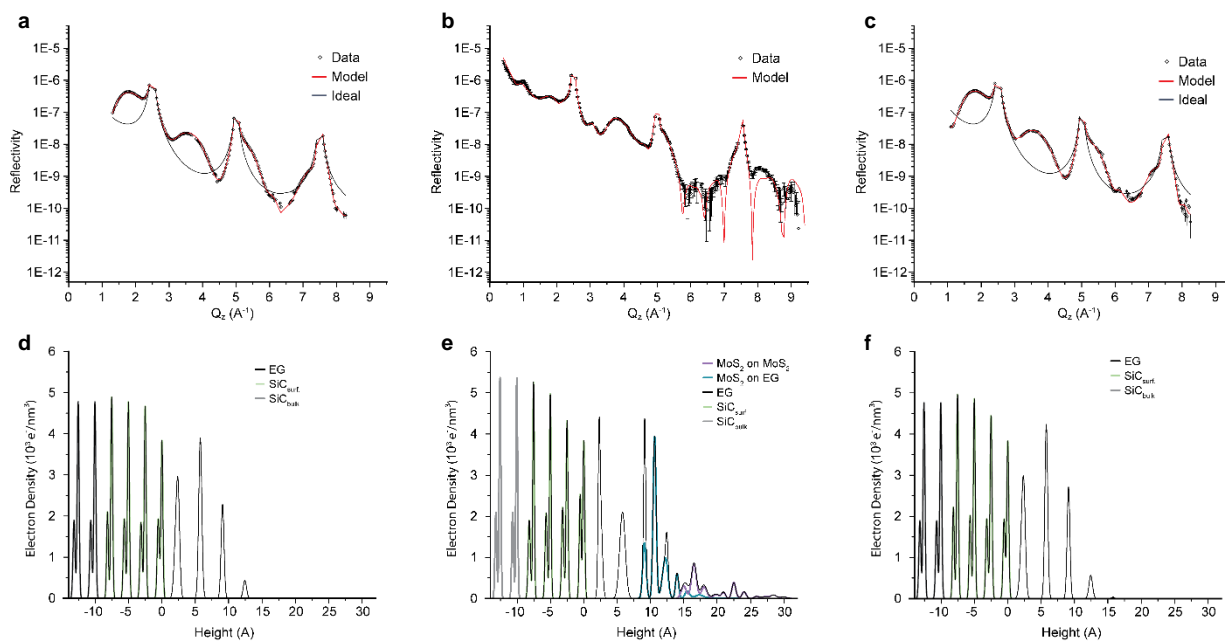


Figure 7.4: XRR data of (a) EG/SiC, (b) CVD-deposited MoS_2 on EG/SiC, and (c) EG/SiC following MoS_2 transfer. XRR data show with black dots and accompanying error bars, model fit with red line, and simulated XRR for an ideal bulk terminated 4H-SiC(0001) surface with a dashed line. (d-f) The XRR model fit derived electron density profile along the [0001] direction.

The XRR derived model fits of EG on SiC(0001) (Figure 7.4d) show exceptional agreement with previously reported values [14,88]. The peaks present at 1.9 \AA^{-1} , 3.7 \AA^{-1} , and 5.6 \AA^{-1} correspond to the 3.3 \AA d-spacing of graphene. The EG_0 layer is comprised of a $40 \pm 10\%$ covalently bonded C layer and $60 \pm 10\%$ relaxed C layer resting $2.1 \pm 0.1 \text{ \AA}$ and $2.4 \pm 0.1 \text{ \AA}$, respectively, above the terminus Si layer of SiC. The gap between the overlaying graphene (EG_{1-3}), closely match values expected from bulk ($3.4 \pm 0.2 \text{ \AA}$). The distribution width ($0.16 \pm 0.2 \text{ \AA}$) confirms EG_{1-3} are pristine graphene layers.

The addition of CVD deposited MoS_2 is accompanied by additional undulations in the XRR data. The C-C peaks at 1.9 \AA^{-1} , 3.7 \AA^{-1} , and 5.6 \AA^{-1} remain, confirming the few-layer graphene

remains pristine after deposition. New sharp undulations present at 1.0 \AA^{-1} and 3.1 \AA^{-1} are primarily accounted for by Mo-Mo spacing ($5.9 \pm 0.2 \text{ \AA}$) which correspond to the formation of few-layer MoS₂ as seen by AFM. These primary features show additional modulations from Mo-C spacing and from the two S layers which accompany each Mo layer in MoS₂. To model the presence of MoS₂, the parameters for EG/SiC(0001) were initially held at fixed values, then relaxed to achieve a best fit. The underlying EG₂₋₃ are unchanged following MoS₂ deposition, and (MoS₂)₂₋₃ on EG₂₋₃ show a vdW gap separation of $4.6 \pm 0.3 \text{ \AA}$ with $20 \pm 6\%$ MoS₂ coverage. Bulk-like bilayer MoS₂ covers the sample with $34 \pm 4\%$ of the (MoS₂)₁₋₃ forming a bilayer.

Significant changes to the model were needed at the region near the interface, consisting of EG₀₋₁, to achieve a good fit. The two distinct carbon peaks that makeup EG₀ shifted outward to $2.3 \pm 0.1 \text{ \AA}$ and $2.5 \pm 0.1 \text{ \AA}$, and their distribution width decreased to ($\sim 0.08 \text{ \AA}$) and ($\sim 0.2 \text{ \AA}$). While the overlaying EG₁ layer broadened in distribution width ($\sim 0.4 \text{ \AA}$). This abnormality in EG₁ was further accompanied by a substantially higher (MoS₂)₁ coverage ($88 \pm 9\%$) suggesting a considerably higher degree of interaction between MoS₂ on EG₁ than on the more graphitic EG₂₋₃ layers. This disproportionately high coverage could be has been reported in previous work on MoS₂ on EG/SiC [225], which shows the formation of near unity coverage MoS₂ specifically on EG₁, and multilayers MoS₂ were only observed atop defective graphene. However, this observation does not fully explain our results and is inconsistent with our AFM data [106].

To verify the chemical integrity of the MoS₂ and EG/SiC XPS data was taken before and after MoS₂ deposition. The Mo 3d and S 2p peaks showed no notable deviation from bulk-like MoS₂, while the C 1s peak is inconclusive owing to the large number of distinct C chemical states present in EG/SiC [14]. The lack of strong covalent chemistry suggests the changes to the interface

are induced through vdW interactions between layers. The structure of the EG₀ buffer layer has previously been shown to be highly sensitive to the stabilizing influence of EG₁ [88]. While the weak electronic screening of graphene allows interfaces on either side of graphene to interact through graphene [50]. Thus, MoS₂ interactions with the EG₀ buffer layer through EG₁ would not be without precedent.

However, complications arise when considering the EG₀ buffer layer, as subtle changes to the interface will have an enhanced impact on the measured XRR by the presence of MoS₂. While it has been clear since early CTR investigations of this interface that the EG₀ layer is sitting at a much-reduced distance (~ 2.2 Å) [134], the precise structure of this interface has undergone continued scrutiny [14,88]. The study performed by Emery [14], utilized XRR measurements enhanced with chemically specific XSW-XPS data, to reveal 2 distinct chemical states of C within EG₀ corresponding to a more sp³-hybridized C at 2.1 ± 0.1 Å and a more sp²-hybridized C at 2.45 ± 0.10 Å. Another XRR and XSW-XPS study performed by Conrad [88] proposes an interface structure with 3 distinct C states that transform with the formation of additional EG layers atop EG₀.

Ultimately, our investigation of the influence of MoS₂ on EG/SiC cannot be conclusive, because the transformation seen at the interface between EG and SiC(0001) with the addition of MoS₂ could either reflect 1) a structural change in the EG/SiC to accommodate the addition of epitaxial MoS₂ or 2) imperfect modeling of the EG/SiC interface, which only becomes evident with the addition of MoS₂.

7.4.4: Annealing Study

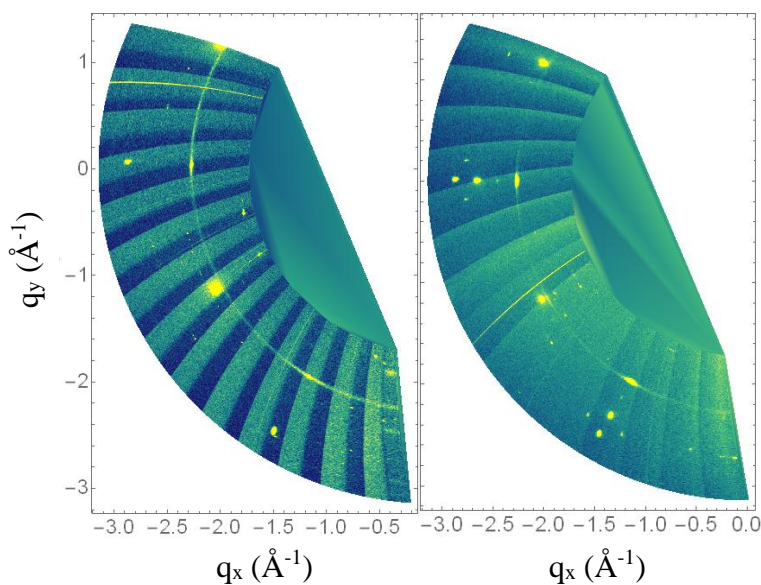


Figure 7.5: GIWAXS measurements of (Left) as-grown CVD-deposited MoS₂ on EG/SiC and (Right) the same sample following an 800 °C and < 40 torr.

A post-growth *in situ* anneal of MoS₂ on EG/SiC was performed at 800 °C and < 40 torr pressure in an effort to improve registry between MoS₂ and EG/SiC(0001). For the as-grown sample, there is a clear MoS₂ powder ring present, indicating the presence of disordered MoS₂ flakes across the EG surface. The integrated intensity of the well oriented spots, normalized to the integrated intensity of the ring, gives the ratio of aligned MoS₂ to disordered MoS₂. Clear improvements in the registry of the MoS₂ are evident in the 800 °C annealed sample from the decreased relative intensity of the powder ring following annealing.

More striking in the 800 °C annealed sample, is the formation of new diffraction peaks, each surrounded by 3 satellite peaks. It appears that MoS₂ stabilizes new structures, which only forms into a well-ordered phase following a post-growth anneal. The central spot corresponds to a new hexagonal phase with a 2.69 Å lattice. This value matches no reported structure of MoS₂ or

C reported in online databases (i.e. ICSD). Complimentary measurements with chemical sensitivity (e.g. XPS) would help identify the elements participating in this structure, allowing for more complete characterization of this new surface structure.

7.4.5: X-ray Damage Study

AFM taken after X-ray exposure shows the formation of additional spots on the MoS₂ flakes which are indicative of oxidation of the MoS₂ flakes. This result is corroborated by XPS measurements which reveal an increased O 1s peak.

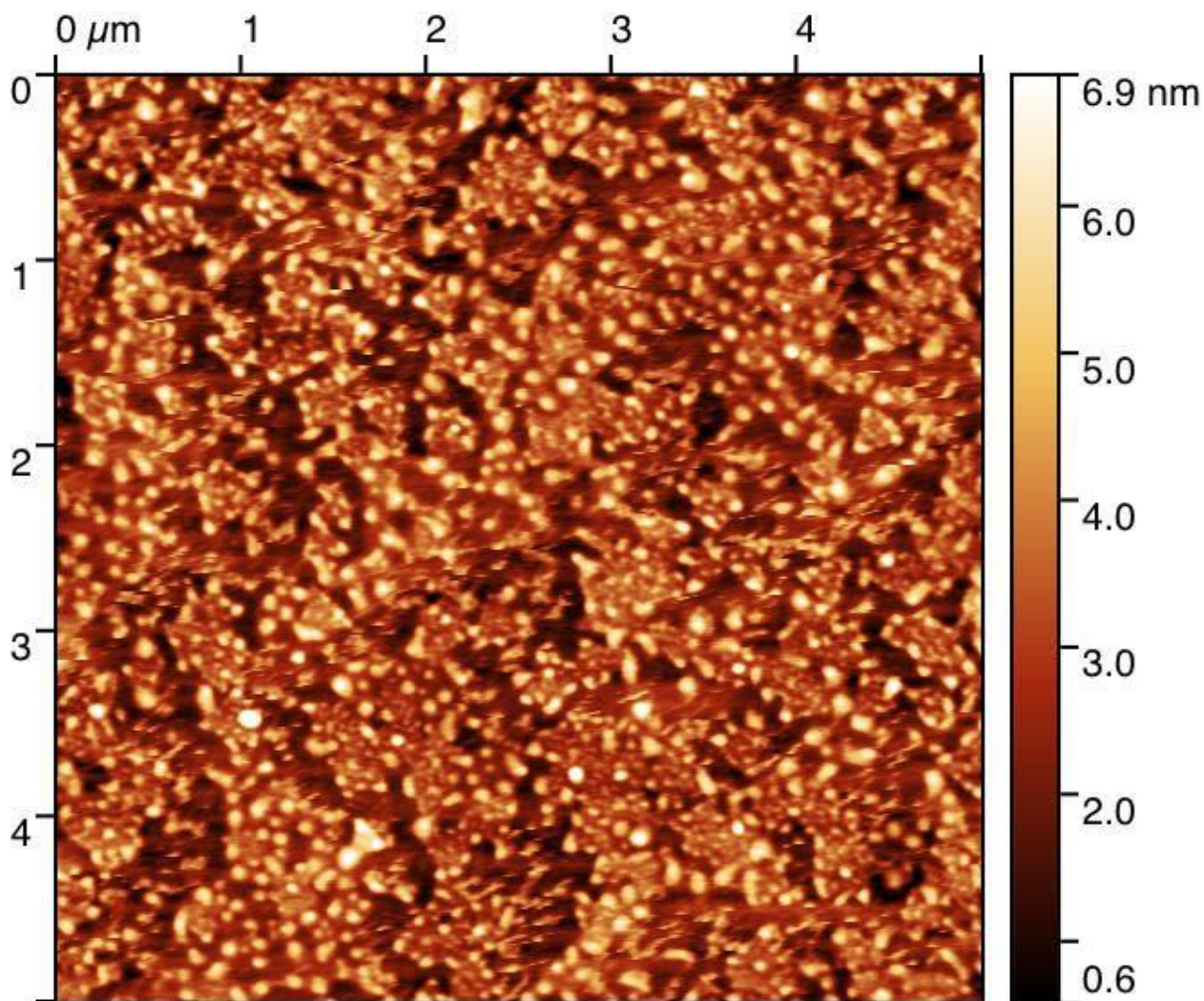


Figure 7.6: AFM of degraded MoS₂ flakes on EG/SiC after hours of exposure to the unattenuated X-ray beam at 33-ID-D. (AFM image provided by J.I. Balla and X. Liu)

7.4.6: Organic molecules on EG/SiC

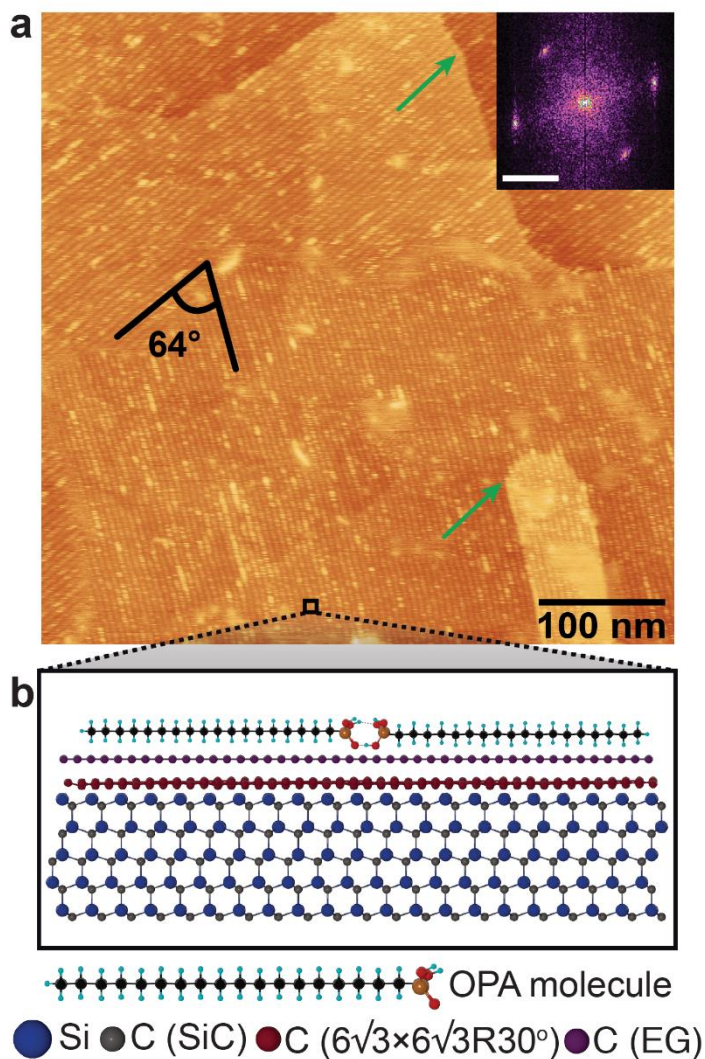


Figure 7.7: AFM of MMS. (a) AFM of OPA SAM on EG. The two domain orientation differ by ~64°. The SAM is continuous over EG/SiC step edges, indicated by green arrows. Fourier transform (inset, scale bar is 1 nm⁻¹) corresponds to a corrugation periodicity of 5.5 ± 0.3 nm. (b) Schematic cross section of OPA on EG/SiC. Bottom to top: 4H-SiC (blue and grey), carbon-rich buffer layer SiC (6√3 × 6√3)R30° surface reconstruction (maroon), graphene layer (purple), and two neighboring OPA molecules with hydrogen bonds between phosphonic acid headgroups. (AFM image provided by J.I. Balla and X. Liu)

We extended synchrotron grazing incidence small-angle X-ray scattering (GISAXS) and grazing incidence wide-angle X-ray scattering (GIWAXS) analysis to examine the registry of 1D heterostructures [226]. Here we investigated the structure of metal deposited on OPA molecules or metalized molecular stripes (MMS). The real space model of the assembly overlaid with the graphene (green), SiC (pink) and MMS (blue) lattice vectors is shown in Figure 7.8a. The corresponding 2D reciprocal space map of platinum MMS is produced from GISAXS images collected as a function of azimuthal angle φ in Figure 7.8b. The six MMS $\{10\}$ Bragg peaks on the map are formed from the superposition of 3 MMS domain orientations. To examine the relative orientations of the MMS domains, an intensity profile cut along the φ direction of the reciprocal space map is fitted with Gaussians and included in Figure 7.8c. The MMS scattered intensity reaches a maximum every $60\pm 2^\circ$ indicating that the MMS domains are conformal to the 6-fold symmetry of the underlying graphene in agreement with the AFM observations. To determine the orientation of the 1D MMS domains with respect to the underlying substrate, GIWAXS data is acquired simultaneously with the GISAXS experiment and provides the coordinates of the SiC $\{101\}$ Bragg peaks, from which the \mathbf{a}_{SiC} in-plane direction can be extracted. The Ewald sphere construction method is used to convert raw GISAXS and GIWAXS data into reciprocal space as shown in Figure 7.8c for direct comparison. The SiC $\{101\}$ Bragg peaks are aligned relative to the MMS $\{10\}$ peaks in Figure 7.8c. In real space, this corresponds to a 30° rotation [221,227] between the \mathbf{a}_{SiC} and \mathbf{a}_{MMS} and a parallel alignment between \mathbf{a}_{MMS} and \mathbf{a}_{EG} real space vectors (Figure 7.8a), indicating that the metal stripes are laying along the EG “arm-chair” direction. MMS spacing and domain structure were calculated from the integrated intensity along the longitudinal (L) path of the reciprocal space map as shown in Figure 7.8d. The 5.41 ± 0.05 nm spacing between the platinum

MMS (5.36 ± 0.14 nm for iron, 5.40 ± 0.06 nm for aluminum) was determined from the MMS $\{10\}$ peaks found at 1.16 ± 0.01 nm⁻¹. The 106 ± 12 nm platinum MMS domain size (120 ± 10 nm for iron and 120 ± 5 nm aluminum) was determined from ΔL of the MMS peak by the Scherrer equation [108]. The average number of MMS within a domain is between 18 to 22 for platinum (20 to 25 for iron and 21 to 23 for aluminum). Overall, these GISAXS and GIWAXS results reveal that the MMS network is uniform across the mm² X-ray beam footprint on the substrate and show the precise alignment between the MMS and underlying graphene.

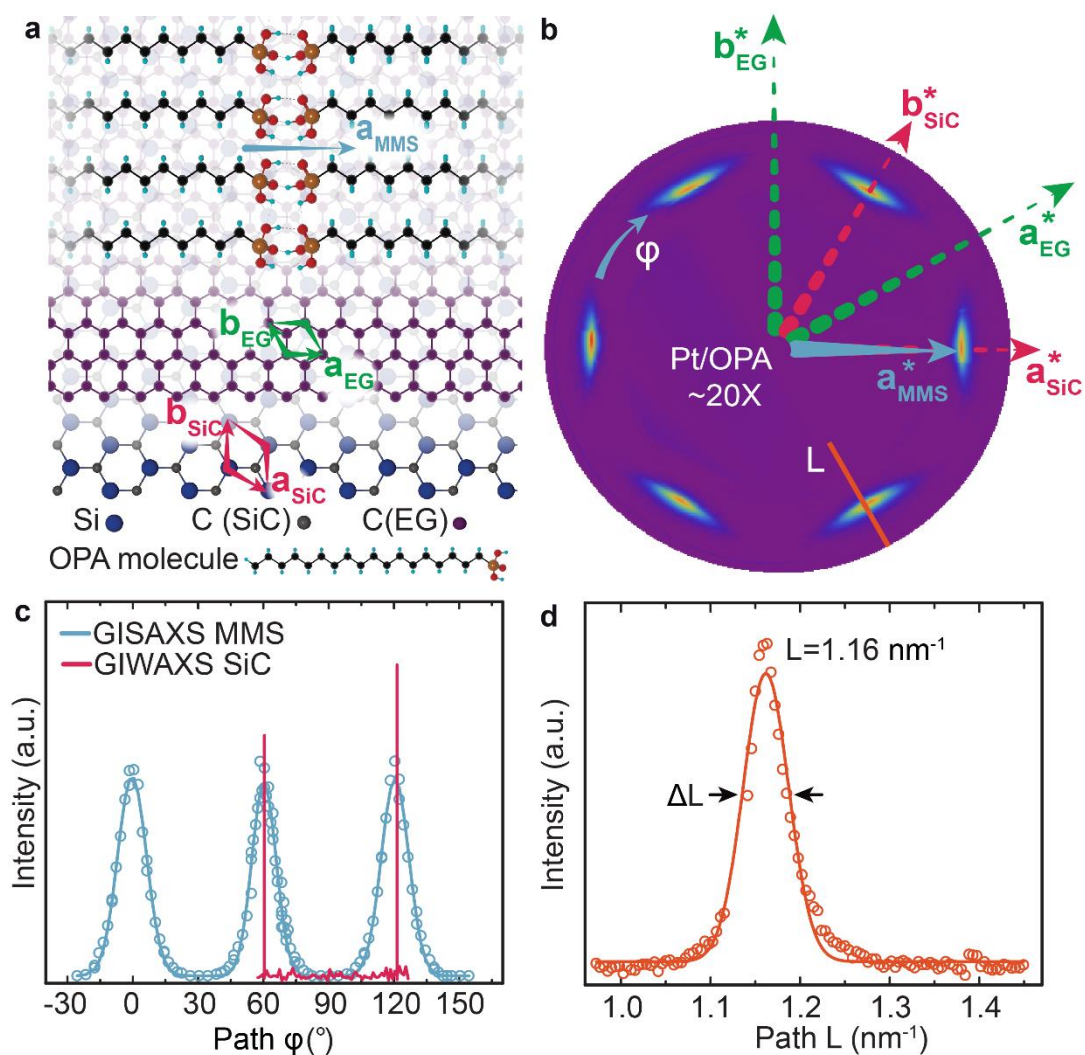


Figure 7.8: Grazing incidence small and wide-angle X-ray scattering. (a) Top view of the assembly in real space overlaid with the graphene (green), SiC (pink) and MMS (grey) unit cell vectors. (The MMS vector extends much longer than shown.) (b) A corresponding 2D reciprocal space map of platinum MMS overlaid with the respective reciprocal unit vectors of panel (a) (the 2D reciprocal space map is scaled by $\sim 20\times$ for clarity). (c) GISAXS intensity profile cut (light blue) from panel (b) along the φ direction (blue) showing maximum intensity at $60^\circ \pm 2^\circ$ intervals. The GISAXS plot is overlaid with GIWAXS SiC $\{101\}$ Bragg peaks (pink) indicating the direction of the MMS with respect to the substrate. (d) Intensity profile cut from panel (b) along the L path allowing determination of MMS spacing.

7.5: Conclusions

In summary, a 2D heterostructure of rotationally commensurate MoS₂ on EG has been grown *via* van der Waals epitaxy with controlled thickness. The structural and electronic quality of these samples has been probed down to the atomic scale using a combination of horizontally and vertically sensitive synchrotron X-ray scattering techniques. MoS₂ is found to preferentially grow with lattice aligned with EG. The relative amount of a less preferred registry is also determined. Furthermore, in-plane X-ray diffraction show that the MoS₂ is nearly strain-free, thus providing an ideal system for probing the fundamental properties of two-dimensional MoS₂. This in addition to our OPA study suggests that EG may be a promising substrate for van der Waals epitaxial growth of other emerging two-dimensional nanomaterials in addition to providing a well-defined platform for the future study and application of MoS₂/graphene heterostructures.

Chapter 8: Future Work

8.1: Borophene on Au(111)

Early theoretical work predicted stable forms of 2D boron on the (111) faces Au, Ag, Cu, and Ni [49]. Of these, borophene has only been successfully grown on Ag(111) [5,6], leaving Au, Cu and Ni yet to be explored. Of these metals, Au(111) is the only surface to show a lowest energy $v_{1/9}$ in-plane structure and 1.1 Å vertically buckled structure, making it distinct from the measured borophene phases on Ag(111). This structure reflects the weaker interaction between the $v_{1/9}$ phase and Au (77 meV/atom) compared to the $v_{1/6}$ phase on Ag (175 meV), explained by weakening of the substrate interactions with the reduction of fractional vacancies in the borophene. The weakened substrate interactions are reflected in the vertical position of the borophene above the substrate, this weakening trend was theoretically predicted for $v_{1/6}$ and $v_{1/5}$ phases of borophene, however the vertical positions of the $v_{1/6}$ and $v_{1/5}$ phases appear identical in our XSW measurements. Synthesizing polymorphs of borophene with drastically different vacancy configurations would enable us to explore theoretical predictions of borophene substrate interactions with more certainty and provide valuable insight into 2D boron polymorphism.

8.2: Blue Phosphorus

2D forms of phosphorus were first isolated by mechanical exfoliation of bulk black phosphorus (BP) [228]. Bulk BP has long been known to exhibit high degrees of polymorphism [41], showing reversible transitions to an arsenic and simple-cubic crystal structure [43]. Blue phosphorus, along with 2 other structural derivatives by geometrical tweaks to BP, were predicted to form layered stable free-standing monolayers [228]. Blue phosphorus was recently synthesized at the 2D limit on Au (111) using molecular beam epitaxy under ultra-high vacuum [44].

STM reveals a 2D diamond structure, which appears in (4x4) registry with the underlying Au(111) and (5x5) registry with the proposed model for blue phosphorus. The proposed superstructure model contains 42 P atoms, 24 of which rest 2.40 Å above the Au(111) and 18 vertically buckled outward at 3.58 Å above the Au(111). The in-plane structure is believed to be somewhat strained to accommodate a slight lattice mismatch between the structure of blue phosphorus and the underlying Au(111). Dark lines are seen in the STM data, which are reflected in the simulations by a relaxation of the bottom layer as well as omitted rows of top layer atoms. Interestingly, this structure deviates considerably from measurements and simulations of bulk blue phosphorus [41,43], suggesting strong interactions at the interface which could be investigated further through chemically resolved structural measurements using synchrotron X-rays.

References:

- [1] A. H. Castro Neto, F. Guinea, N. M. R. Peres, K. S. Novoselov, and A. K. Geim, The Electronic Properties of Graphene, *Reviews of Modern Physics* **81**, 109 (2009).
- [2] Y. Zhang, V. W. Brar, C. Girit, A. Zettl, and M. F. Crommie, Origin of Spatial Charge Inhomogeneity in Graphene, *Nature Physics* **5**, 722 (2009).
- [3] A. K. Newaz, Y. S. Puzyrev, B. Wang, S. T. Pantelides, and K. I. Bolotin, Probing Charge Scattering Mechanisms in Suspended Graphene by Varying Its Dielectric Environment, *Nat Commun* **3**, 734, 734 (2012).
- [4] Z. Y. Al Balushi, K. Wang, R. K. Ghosh, R. A. Vila, S. M. Eichfeld, J. D. Caldwell, X. Qin, Y. C. Lin, P. A. DeSario, G. Stone, S. Subramanian, D. F. Paul, R. M. Wallace, S. Datta, J. M. Redwing, and J. A. Robinson, Two-Dimensional Gallium Nitride Realized Via Graphene Encapsulation, *Nat Mater* **15**, 1166 (2016).
- [5] B. Feng, J. Zhang, Q. Zhong, W. Li, S. Li, H. Li, P. Cheng, S. Meng, L. Chen, and K. Wu, Experimental Realization of Two-Dimensional Boron Sheets, *Nat Chem* **8**, 563 (2016).
- [6] A. J. Mannix, X. F. Zhou, B. Kiraly, J. D. Wood, D. Alducin, B. D. Myers, X. Liu, B. L. Fisher, U. Santiago, J. R. Guest, M. J. Yacaman, A. Ponce, A. R. Oganov, M. C. Hersam, and N. P. Guisinger, Synthesis of Borophenes: Anisotropic, Two-Dimensional Boron Polymorphs, *Science* **350**, 1513 (2015).
- [7] P. Vogt, P. De Padova, C. Quaresima, J. Avila, E. Frantzeskakis, M. C. Asensio, A. Resta, B. Ealet, and G. Le Lay, Silicene: Compelling Experimental Evidence for Graphenelike Two-Dimensional Silicon, *Phys Rev Lett* **108**, 155501 (2012).
- [8] A. J. Mannix, B. Kiraly, B. L. Fisher, M. C. Hersam, and N. P. Guisinger, Silicon Growth at the Two-Dimensional Limit on Ag(111), *ACS Nano* **8**, 7538 (2014).
- [9] Y. Chen, M. W. Gramlich, S. T. Hayden, and P. F. Miceli, In Situ X-Ray Scattering Study of Ag Island Growth on Si(111)7×7, *Physical Review B* **94**, 11, 045437 (2016).
- [10] M. Satta, S. Colonna, R. Flammini, A. Cricenti, and F. Ronci, Silicon Reactivity at the Ag(111) Surface, *Phys Rev Lett* **115**, 026102, 026102 (2015).
- [11] A. K. Geim, Graphene: Status and Prospects, *Science* **324**, 1530 (2009).
- [12] C. R. Dean, A. F. Young, I. Meric, C. Lee, L. Wang, S. Sorgenfrei, K. Watanabe, T. Taniguchi, P. Kim, K. L. Shepard, and J. Hone, Boron Nitride Substrates for High-Quality Graphene Electronics, *Nat Nanotechnol* **5**, 722 (2010).
- [13] J. H. Chen, C. Jang, S. Xiao, M. Ishigami, and M. S. Fuhrer, Intrinsic and Extrinsic Performance Limits of Graphene Devices on SiO₂, *Nat Nanotechnol* **3**, 206 (2008).
- [14] J. D. Emery, B. Detlefs, H. J. Karmel, L. O. Nyakiti, D. K. Gaskill, M. C. Hersam, J. Zegenhagen, and M. J. Bedzyk, Chemically Resolved Interface Structure of Epitaxial Graphene on SiC(0001), *Phys Rev Lett* **111**, 215501 (2013).
- [15] J. C. Meyer, A. K. Geim, M. I. Katsnelson, K. S. Novoselov, T. J. Booth, and S. Roth, The Structure of Suspended Graphene Sheets, *Nature* **446**, 60 (2007).
- [16] J. C. Shelton, H. R. Patil, and J. M. Blakely, Equilibrium Segregation of Carbon to a Nickel (111) Surface: A Surface Phase Transition, *Surface Science* **43**, 493 (1974).

- [17] T. A. Land, T. Michely, R. J. Behm, J. C. Hemminger, and G. Comsa, Stm Investigation of Single Layer Graphite Structures Produced on Pt(111) by Hydrocarbon Decomposition, *Surface Science* **264**, 261 (1992).
- [18] M. Eizenberg and J. M. Blakely, Carbon Interaction with Nickel Surfaces: Monolayer Formation and Structural Stability, *The Journal of Chemical Physics* **71**, 3467 (1979).
- [19] I. Forbeaux, J. M. Themlin, and J. M. Debever, Heteroepitaxial Graphite On6h–SiC(0001): Interface Formation through Conduction-Band Electronic Structure, *Physical Review B* **58**, 16396 (1998).
- [20] N. D. Mermin, Crystalline Order in Two Dimensions, *Physical Review* **176**, 250 (1968).
- [21] K. S. Novoselov, A. K. Geim, S. V. Morozov, D. Jiang, Y. Zhang, S. V. Dubonos, I. V. Grigorieva, and A. A. Firsov, Electric Field Effect in Atomically Thin Carbon Films, *Science* **306**, 666 (2004).
- [22] X. Li, W. Cai, J. An, S. Kim, J. Nah, D. Yang, R. Piner, A. Velamakanni, I. Jung, E. Tutuc, S. K. Banerjee, L. Colombo, and R. S. Ruoff, Large-Area Synthesis of High-Quality and Uniform Graphene Films on Copper Foils, *Science* **324**, 1312 (2009).
- [23] J.-H. Lee, E. K. Lee, W.-J. Joo, Y. Jang, B.-S. Kim, J. Y. Lim, S.-H. Choi, S. J. Ahn, J. R. Ahn, M.-H. Park, C.-W. Yang, B. L. Choi, S.-W. Hwang, and D. Whang, Wafer-Scale Growth of Single-Crystal Monolayer Graphene on Reusable Hydrogen-Terminated Germanium, *Science* **344**, 286 (2014).
- [24] X. Li, W. Cai, J. An, S. Kim, J. Nah, D. Yang, R. Piner, A. Velamakanni, I. Jung, E. Tutuc, S. K. Banerjee, L. Colombo, and R. S. Ruoff, Large-Area Synthesis of High-Quality and Uniform Graphene Films on Copper Foils, *Science* **324**, 1312 (2009).
- [25] J. N. Coleman, M. Lotya, A. O'Neill, S. D. Bergin, P. J. King, U. Khan, K. Young, A. Gaucher, S. De, R. J. Smith, I. V. Shvets, S. K. Arora, G. Stanton, H. Y. Kim, K. Lee, G. T. Kim, G. S. Duesberg, T. Hallam, J. J. Boland, J. J. Wang, J. F. Donegan, J. C. Grunlan, G. Moriarty, A. Shmeliov, R. J. Nicholls, J. M. Perkins, E. M. Grievson, K. Theuwissen, D. W. McComb, P. D. Nellist, and V. Nicolosi, Two-Dimensional Nanosheets Produced by Liquid Exfoliation of Layered Materials, *Science* **331**, 568 (2011).
- [26] J. Kang, J. W. Seo, D. Alducin, A. Ponce, M. J. Yacaman, and M. C. Hersam, Thickness Sorting of Two-Dimensional Transition Metal Dichalcogenides Via Copolymer-Assisted Density Gradient Ultracentrifugation, *Nat Commun* **5**, 5478, 5478 (2014).
- [27] E. Grånäs, T. Gerber, U. A. Schröder, K. Schulte, J. N. Andersen, T. Michely, and J. Knudsen, Hydrogen Intercalation under Graphene on Ir(111), *Surface Science* **651**, 57 (2016).
- [28] C. Lee, X. Wei, J. W. Kysar, and J. Hone, Measurement of the Elastic Properties and Intrinsic Strength of Monolayer Graphene, *Science* **321**, 385 (2008).
- [29] R. R. Nair, P. Blake, A. N. Grigorenko, K. S. Novoselov, T. J. Booth, T. Stauber, N. M. Peres, and A. K. Geim, Fine Structure Constant Defines Visual Transparency of Graphene, *Science* **320**, 1308 (2008).
- [30] A. K. Geim and K. S. Novoselov, The Rise of Graphene, *Nat Mater* **6**, 183 (2007).
- [31] T. Bjorkman, A. Gulans, A. V. Krasheninnikov, and R. M. Nieminen, Van Der Waals Bonding in Layered Compounds from Advanced Density-Functional First-Principles Calculations, *Physical Review Letters* **108**, 5, 235502 (2012).
- [32] H. W. Kroto, J. R. Heath, S. C. O'Brien, R. F. Curl, and R. E. Smalley, C60: Buckminsterfullerene, *Nature* **318**, 162 (1985).

- [33] S. Iijima, Helical Microtubules of Graphitic Carbon, *Nature* **354**, 56 (1991).
- [34] B. T. Kiraly, Northwestern University, 2016.
- [35] Y. Zhang, Y. W. Tan, H. L. Stormer, and P. Kim, Experimental Observation of the Quantum Hall Effect and Berry's Phase in Graphene, *Nature* **438**, 201 (2005).
- [36] G. W. Semenoff, Condensed-Matter Simulation of a Three-Dimensional Anomaly, *Physical Review Letters* **53**, 2449 (1984).
- [37] E. Fradkin, Critical Behavior of Disordered Degenerate Semiconductors. II. Spectrum and Transport Properties in Mean-Field Theory, *Phys Rev B Condens Matter* **33**, 3263 (1986).
- [38] F. D. Haldane, Model for a Quantum Hall Effect without Landau Levels: Condensed-Matter Realization of the "Parity Anomaly", *Phys Rev Lett* **61**, 2015 (1988).
- [39] K. Takeda and K. Shiraishi, Theoretical Possibility of Stage Corrugation in Si and Ge Analogs of Graphite, *Phys Rev B Condens Matter* **50**, 14916 (1994).
- [40] S. Cahangirov, M. Topsakal, E. Akturk, H. Sahin, and S. Ciraci, Two- and One-Dimensional Honeycomb Structures of Silicon and Germanium, *Phys Rev Lett* **102**, 236804, 236804 (2009).
- [41] J. C. Jamieson, Crystal Structures Adopted by Black Phosphorus at High Pressures, *Science* **139**, 1291 (1963).
- [42] J. Guan, Z. Zhu, and D. Tomanek, Phase Coexistence and Metal-Insulator Transition in Few-Layer Phosphorene: A Computational Study, *Phys Rev Lett* **113**, 046804 (2014).
- [43] S. E. Boulfelfel, G. Seifert, Y. Grin, and S. Leoni, Squeezing Lone Pairs: The A17 to A7 Pressure-Induced Phase Transition in Black Phosphorus, *Physical Review B* **85**, 6, 014110 (2012).
- [44] J. L. Zhang, S. Zhao, C. Han, Z. Wang, S. Zhong, S. Sun, R. Guo, X. Zhou, C. D. Gu, K. D. Yuan, Z. Li, and W. Chen, Epitaxial Growth of Single Layer Blue Phosphorus: A New Phase of Two-Dimensional Phosphorus, *Nano Lett* **16**, 4903 (2016).
- [45] M. Wu, H. Fu, L. Zhou, K. Yao, and X. C. Zeng, Nine New Phosphorene Polymorphs with Non-Honeycomb Structures: A Much Extended Family, *Nano Lett* **15**, 3557 (2015).
- [46] B. Feng, Z. Ding, S. Meng, Y. Yao, X. He, P. Cheng, L. Chen, and K. Wu, Evidence of Silicene in Honeycomb Structures of Silicon on Ag(111), *Nano Lett* **12**, 3507 (2012).
- [47] S. Cahangirov, V. O. Özçelik, L. Xian, J. Avila, S. Cho, M. C. Asensio, S. Ciraci, and A. Rubio, Atomic Structure of The3×3phase of Silicene on Ag(111), *Physical Review B* **90**, 035448 (2014).
- [48] E. Vlieg, E. Fontes, and J. R. Patel, Structure Analysis of Si(111)-($\sqrt{3} \times \sqrt{3}$)R30°/Ag Using X-Ray Standing Waves, *Physical Review B* **43**, 7185 (1991).
- [49] Z. Zhang, Y. Yang, G. Gao, and B. I. Yakobson, Two-Dimensional Boron Monolayers Mediated by Metal Substrates, *Angew Chem Int Ed Engl* **54**, 13022 (2015).
- [50] Y. Kim, S. S. Cruz, K. Lee, B. O. Alawode, C. Choi, Y. Song, J. M. Johnson, C. Heidelberger, W. Kong, S. Choi, K. Qiao, I. Almansouri, E. A. Fitzgerald, J. Kong, A. M. Kolpak, J. Hwang, and J. Kim, Remote Epitaxy through Graphene Enables Two-Dimensional Material-Based Layer Transfer, *Nature* **544**, 340 (2017).
- [51] K. V. Emtsev, F. Speck, T. Seyller, L. Ley, and J. D. Riley, Interaction, Growth, and Ordering of Epitaxial Graphene on Sic{0001} Surfaces: A Comparative Photoelectron Spectroscopy Study, *Physical Review B* **77** (2008).

- [52] A. Koma, Vanderwaals Epitaxy - a New Epitaxial-Growth Method for a Highly Lattice-Mismatched System, *Thin Solid Films* **216**, 72 (1992).
- [53] M. Xu, T. Liang, M. Shi, and H. Chen, Graphene-Like Two-Dimensional Materials, *Chem Rev* **113**, 3766 (2013).
- [54] M. Ishigami, J. H. Chen, W. G. Cullen, M. S. Fuhrer, and E. D. Williams, Atomic Structure of Graphene on SiO₂, *Nano Lett* **7**, 1643 (2007).
- [55] C. R. Dean, A. F. Young, I. Meric, C. Lee, L. Wang, S. Sorgenfrei, K. Watanabe, T. Taniguchi, P. Kim, K. L. Shepard, and J. Hone, Boron Nitride Substrates for High-Quality Graphene Electronics, *Nature Nanotechnology* **5**, 722 (2010).
- [56] A. M. Shikin, D. Farías, and K. H. Rieder, Phonon Stiffening Induced by Copper Intercalation in Monolayer Graphite on Ni(111), *Europhysics Letters (EPL)* **44**, 44 (1998).
- [57] Y. Gamo, A. Nagashima, M. Wakabayashi, M. Terai, and C. Oshima, Atomic Structure of Monolayer Graphite Formed on Ni(111), *Surface Science* **374**, 61 (1997).
- [58] A. Varykhalov, J. Sanchez-Barriga, A. M. Shikin, C. Biswas, E. Vescovo, A. Rybkin, D. Marchenko, and O. Rader, Electronic and Magnetic Properties of Quasifreestanding Graphene on Ni, *Phys Rev Lett* **101**, 157601, 157601 (2008).
- [59] H. Tetlow, J. Posthuma de Boer, I. J. Ford, D. D. Vvedensky, J. Coraux, and L. Kantorovich, Growth of Epitaxial Graphene: Theory and Experiment, *Physics Reports* **542**, 195 (2014).
- [60] M. Batzill, The Surface Science of Graphene: Metal Interfaces, Cvd Synthesis, Nanoribbons, Chemical Modifications, and Defects, *Surface Science Reports* **67**, 83 (2012).
- [61] C. Riedl, C. Coletti, and U. Starke, Structural and Electronic Properties of Epitaxial Graphene on SiC(0001): A Review of Growth, Characterization, Transfer Doping and Hydrogen Intercalation, *Journal of Physics D: Applied Physics* **43**, 374009 (2010).
- [62] W. Norimatsu and M. Kusunoki, Epitaxial Graphene on SiC{0001}: Advances and Perspectives, *Phys Chem Chem Phys* **16**, 3501 (2014).
- [63] A. B. Preobrajenski, M. L. Ng, A. S. Vinogradov, and N. Martensson, Controlling Graphene Corrugation on Lattice-Mismatched Substrates, *Physical Review B* **78**, 4, 073401 (2008).
- [64] D. Eom, D. Prezzi, K. T. Rim, H. Zhou, M. Lefenfeld, S. Xiao, C. Nuckolls, M. S. Hybertsen, T. F. Heinz, and G. W. Flynn, Structure and Electronic Properties of Graphene Nanoislands on Co(0001), *Nano Lett* **9**, 2844 (2009).
- [65] W. Moritz, B. Wang, M. L. Bocquet, T. Brugger, T. Greber, J. Winterlin, and S. Gunther, Structure Determination of the Coincidence Phase of Graphene on Ru(0001), *Phys Rev Lett* **104**, 136102, 136102 (2010).
- [66] D. Martoccia, P. R. Willmott, T. Brugger, M. Bjorck, S. Gunther, C. M. Schleputz, A. Cervellino, S. A. Pauli, B. D. Patterson, S. Marchini, J. Winterlin, W. Moritz, and T. Greber, Graphene on Ru(0001): A 25 X 25 Supercell, *Phys Rev Lett* **101**, 126102, 126102 (2008).
- [67] B. Wang, M. Caffio, C. Bromley, H. Fruchtl, and R. Schaub, Coupling Epitaxy, Chemical Bonding, and Work Function at the Local Scale in Transition Metal-Supported Graphene, *ACS Nano* **4**, 5773 (2010).
- [68] E. Miniussi, M. Pozzo, A. Baraldi, E. Vesselli, R. R. Zhan, G. Comelli, T. O. Mendes, M. A. Nino, A. Locatelli, S. Lizzit, and D. Alfe, Thermal Stability of Corrugated Epitaxial Graphene Grown on Re(0001), *Phys Rev Lett* **106**, 216101, 216101 (2011).

- [69] Q. J. Wang and J. G. Che, Origins of Distinctly Different Behaviors of Pd and Pt Contacts on Graphene, *Phys Rev Lett* **103**, 066802, 066802 (2009).
- [70] G. Giovannetti, P. A. Khomyakov, G. Brocks, V. M. Karpan, J. van den Brink, and P. J. Kelly, Doping Graphene with Metal Contacts, *Phys Rev Lett* **101**, 026803, 026803 (2008).
- [71] P. Sutter, J. T. Sadowski, and E. Sutter, Graphene on Pt(111): Growth and Substrate Interaction, *Physical Review B* **80**, 245411 (2009).
- [72] C. Gong, G. Lee, B. Shan, E. M. Vogel, R. M. Wallace, and K. Cho, First-Principles Study of Metal–Graphene Interfaces, *Journal of Applied Physics* **108**, 123711 (2010).
- [73] M. Vanin, J. J. Mortensen, A. K. Kelkkanen, J. M. Garcia-Lastra, K. S. Thygesen, and K. W. Jacobsen, Graphene on Metals: A Van Der Waals Density Functional Study, *Physical Review B* **81**, 081408 (2010).
- [74] C. Busse, P. Lazic, R. Djemour, J. Coraux, T. Gerber, N. Atodiresei, V. Caciuc, R. Brako, A. T. N'Diaye, S. Blugel, J. Zegenhagen, and T. Michely, Graphene on Ir(111): Physisorption with Chemical Modulation, *Phys Rev Lett* **107**, 036101, 036101 (2011).
- [75] N. A. Vinogradov, A. A. Zakharov, V. Kocevski, J. Ruzs, K. A. Simonov, O. Eriksson, A. Mikkelsen, E. Lundgren, A. S. Vinogradov, N. Martensson, and A. B. Preobrajenski, Formation and Structure of Graphene Waves on Fe(110), *Phys Rev Lett* **109**, 026101, 026101 (2012).
- [76] B. Hammer and J. K. Norskov, in *Advances in Catalysis, Vol 45: Impact of Surface Science on Catalysis*, edited by B. C. Gates, and H. Knozinger(2000), pp. 71.
- [77] J. J. McCarroll, T. Edmonds, and R. C. Pitkethly, Interpretation of a Complex Low Energy Electron Diffraction Pattern: Carbonaceous and Sulphur-Containing Structures on Ni(111), *Nature* **223**, 1260 (1969).
- [78] C. Klink, I. Stensgaard, F. Besenbacher, and E. Lægsgaard, An Stm Study of Carbon-Induced Structures on Ni(111): Evidence for a Carbodic-Phase Clock Reconstruction, *Surface Science* **342**, 250 (1995).
- [79] F. Mittendorfer, A. Garhofer, J. Redinger, J. Klimes, J. Harl, and G. Kresse, Graphene on Ni(111): Strong Interaction and Weak Adsorption, *Physical Review B* **84**, 201401 (2011).
- [80] L. Gao, J. R. Guest, and N. P. Guisinger, Epitaxial Graphene on Cu(111), *Nano Lett* **10**, 3512 (2010).
- [81] J. H. Lee, E. K. Lee, W. J. Joo, Y. Jang, B. S. Kim, J. Y. Lim, S. H. Choi, S. J. Ahn, J. R. Ahn, M. H. Park, C. W. Yang, B. L. Choi, S. W. Hwang, and D. Whang, Wafer-Scale Growth of Single-Crystal Monolayer Graphene on Reusable Hydrogen-Terminated Germanium, *Science* **344**, 286 (2014).
- [82] B. Kiraly, R. M. Jacobberger, A. J. Mannix, G. P. Campbell, M. J. Bedzyk, M. S. Arnold, M. C. Hersam, and N. P. Guisinger, Electronic and Mechanical Properties of Graphene-Germanium Interfaces Grown by Chemical Vapor Deposition, *Nano Lett* **15**, 7414 (2015).
- [83] J. Dai, D. Wang, M. Zhang, T. Niu, A. Li, M. Ye, S. Qiao, G. Ding, X. Xie, Y. Wang, P. K. Chu, Q. Yuan, Z. Di, X. Wang, F. Ding, and B. I. Yakobson, How Graphene Islands Are Unidirectionally Aligned on the Ge(110) Surface, *Nano Lett* **16**, 3160 (2016).
- [84] R. Rojas Delgado, R. M. Jacobberger, S. S. Roy, V. S. Mangu, M. S. Arnold, F. Cavallo, and M. G. Lagally, Passivation of Germanium by Graphene, *ACS Appl Mater Interfaces* **9**, 17629 (2017).

- [85] R. I. Scace and G. A. Slack, Solubility of Carbon in Silicon and Germanium, *The Journal of Chemical Physics* **30**, 1551 (1959).
- [86] W. Strupinski, K. Grodecki, A. Wyszomolek, R. Stepniewski, T. Szkopek, P. E. Gaskell, A. Gruneis, D. Haberer, R. Bozek, J. Krupka, and J. M. Baranowski, Graphene Epitaxy by Chemical Vapor Deposition on Sic, *Nano Lett* **11**, 1786 (2011).
- [87] A. Al-Temimy, C. Riedl, and U. Starke, Low Temperature Growth of Epitaxial Graphene on Sic Induced by Carbon Evaporation, *Applied Physics Letters* **95**, 3, 231907 (2009).
- [88] M. Conrad, J. Rault, Y. Utsumi, Y. Garreau, A. Vlad, A. Coati, J. P. Rueff, P. F. Miceli, and E. H. Conrad, Structure and Evolution of Semiconducting Buffer Graphene Grown on Sic(0001), *Physical Review B* **96**, 12, 195304 (2017).
- [89] W. A. de Heer, C. Berger, X. Wu, P. N. First, E. H. Conrad, X. Li, T. Li, M. Sprinkle, J. Hass, M. L. Sadowski, M. Potemski, and G. Martinez, Epitaxial Graphene, *Solid State Communications* **143**, 92 (2007).
- [90] C. Virojanadara, M. Syväjärvi, R. Yakimova, L. I. Johansson, A. A. Zakharov, and T. Balasubramanian, Homogeneous Large-Area Graphene Layer Growth On6h-Sic(0001), *Physical Review B* **78**, 245403 (2008).
- [91] R. M. Tromp and J. B. Hannon, Thermodynamics and Kinetics of Graphene Growth on Sic(0001), *Phys Rev Lett* **102**, 106104, 106104 (2009).
- [92] K. V. Emtsev, A. Bostwick, K. Horn, J. Jobst, G. L. Kellogg, L. Ley, J. L. McChesney, T. Ohta, S. A. Reshanov, J. Rohrl, E. Rotenberg, A. K. Schmid, D. Waldmann, H. B. Weber, and T. Seyller, Towards Wafer-Size Graphene Layers by Atmospheric Pressure Graphitization of Silicon Carbide, *Nat Mater* **8**, 203 (2009).
- [93] E. S. Penev, S. Bhowmick, A. Sadrzadeh, and B. I. Yakobson, Polymorphism of Two-Dimensional Boron, *Nano Lett* **12**, 2441 (2012).
- [94] H. Tang and S. Ismail-Beigi, Novel Precursors for Boron Nanotubes: The Competition of Two-Center and Three-Center Bonding in Boron Sheets, *Phys Rev Lett* **99**, 115501 (2007).
- [95] B. Feng, J. Zhang, R.-Y. Liu, T. Iimori, C. Lian, H. Li, L. Chen, K. Wu, S. Meng, F. Komori, and I. Matsuda, Direct Evidence of Metallic Bands in a Monolayer Boron Sheet, *Physical Review B* **94**, 041408 (2016).
- [96] E. S. Penev, A. Kutana, and B. I. Yakobson, Can Two-Dimensional Boron Superconduct?, *Nano Lett* **16**, 2522 (2016).
- [97] Y. Zhao, S. Zeng, and J. Ni, Superconductivity in Two-Dimensional Boron Allotropes, *Physical Review B* **93**, 014502 (2016).
- [98] Y. Liu, E. S. Penev, and B. I. Yakobson, Probing the Synthesis of Two-Dimensional Boron by First-Principles Computations, *Angew Chem Int Ed Engl* **52**, 3156 (2013).
- [99] Q. Zhong, J. Zhang, P. Cheng, B. Feng, W. Li, S. Sheng, H. Li, S. Meng, L. Chen, and K. Wu, Metastable Phases of 2d Boron Sheets on Ag(1 1 1), *J Phys Condens Matter* **29**, 095002 (2017).
- [100] Z. Zhang, A. J. Mannix, Z. Hu, B. Kiraly, N. P. Guisinger, M. C. Hersam, and B. I. Yakobson, Substrate-Induced Nanoscale Undulations of Borophene on Silver, *Nano Lett* **16**, 6622 (2016).
- [101] Z. Zhang, E. S. Penev, and B. I. Yakobson, Two-Dimensional Materials: Polyphony in B Flat, *Nat Chem* **8**, 525 (2016).

- [102] X. Yang, Y. Ding, and J. Ni, Ab Initio Prediction of Stable Boron Sheets and Boron Nanotubes: Structure, Stability, and Electronic Properties, *Physical Review B* **77**, 041402 (2008).
- [103] Z. Zhang, E. S. Penev, and B. I. Yakobson, Two-Dimensional Boron: Structures, Properties and Applications, *Chem Soc Rev* **46**, 6746 (2017).
- [104] A. J. Mannix, B. Kiraly, M. C. Hersam, and N. P. Guisinger, Synthesis and Chemistry of Elemental 2d Materials, *Nat. Rev. Chem.* **1**, 14, 0014 (2017).
- [105] A. K. Geim and I. V. Grigorieva, Van Der Waals Heterostructures, *Nature* **499**, 419 (2013).
- [106] X. Liu, I. Balla, H. Bergeron, G. P. Campbell, M. J. Bedzyk, and M. C. Hersam, Rotationally Commensurate Growth of Mos₂ on Epitaxial Graphene, *ACS Nano* **10**, 1067 (2016).
- [107] Y. Shi, W. Zhou, A. Y. Lu, W. Fang, Y. H. Lee, A. L. Hsu, S. M. Kim, K. K. Kim, H. Y. Yang, L. J. Li, J. C. Idrobo, and J. Kong, Van Der Waals Epitaxy of Mos₂ Layers Using Graphene as Growth Templates, *Nano Lett* **12**, 2784 (2012).
- [108] B. E. Warren, *X-Ray Diffraction* (Dover Publications, 1969).
- [109] J. Als-Nielsen and D. McMorrow, in *Elements of Modern X-Ray Physics* (John Wiley & Sons, Inc., 2011), pp. 113.
- [110] J. Woicik, *Hard X-Ray Photoelectron Spectroscopy (Haxpes)* 2016), Springer Series in Surface Sciences.
- [111] J. D. Watson and F. H. Crick, Molecular Structure of Nucleic Acids; a Structure for Deoxyribose Nucleic Acid, *Nature* **171**, 737 (1953).
- [112] B. W. Batterman, Effect of Thermal Vibrations on Diffraction from Perfect Crystals. II. The Bragg Case of Reflection, *Physical Review* **127**, 686 (1962).
- [113] B. Okkerse, Anomalous Transmission of X-Rays in Germanium .1. Imaginary Part of Atomic Scattering Factor, *Philips Research Reports* **17**, 464 (1962).
- [114] B. W. Batterman and H. Cole, Dynamical Diffraction of X Rays by Perfect Crystals, *Reviews of Modern Physics* **36**, 681 (1964).
- [115] N. Kato, Dynamical Diffraction Theory of Waves in Distorted Crystals. I. General Formulation and Treatment for Perfect Crystals, *Acta Crystallographica* **16**, 276 (1963).
- [116] N. Kato, Dynamical Diffraction Theory of Waves in Distorted Crystals. II. Perturbation Theory, *Acta Crystallographica* **16**, 282 (1963).
- [117] C. J. Fisher, R. Ithn, R. G. Jones, G. J. Jackson, D. P. Woodruff, and B. C. C. Cowie, Non-Dipole Photoemission Effects in X-Ray Standing Wavefield Determination of Surface Structure, *Journal of Physics: Condensed Matter* **10**, L623 (1998).
- [118] F. Schreiber, K. A. Ritley, I. A. Vartanyants, H. Dosch, J. Zegenhagen, and B. C. C. Cowie, Non-Dipolar Contributions in Xps Detection of X-Ray Standing Waves, *Surface Science* **486**, L519 (2001).
- [119] G. van Straaten, M. Franke, F. C. Bocquet, F. S. Tautz, and C. Kumpf, Non-Dipolar Effects in Photoelectron-Based Normal Incidence X-Ray Standing Wave Experiments, *Journal of Electron Spectroscopy and Related Phenomena* **222**, 106 (2018).
- [120] F. H. Farwick Zum Hagen, D. M. Zimmermann, C. C. Silva, C. Schlueter, N. Atodiresei, W. Jolie, A. J. Martinez-Galera, D. Dombrowski, U. A. Schroder, M. Will, P. Lazic, V. Caciuc, S. Blugel, T. L. Lee, T. Michely, and C. Busse, Structure and Growth of Hexagonal Boron Nitride on Ir(111), *ACS Nano* **10**, 11012 (2016).

- [121] M. Schwarz, A. Riss, M. Garnica, J. Ducke, P. S. Deimel, D. A. Duncan, P. K. Thakur, T. L. Lee, A. P. Seitsonen, J. V. Barth, F. Allegretti, and W. Auwarter, Corrugation in the Weakly Interacting Hexagonal-Bn/Cu(111) System: Structure Determination by Combining Noncontact Atomic Force Microscopy and X-Ray Standing Waves, *ACS Nano* **11**, 9151 (2017).
- [122] D. P. Woodruff, Surface Structure Determination Using X-Ray Standing Waves, *Reports on Progress in Physics* **68**, 743 (2005).
- [123] J. Zegenhagen, Surface-Structure Determination with X-Ray Standing Waves, *Surface Science Reports* **18**, 199 (1993).
- [124] J. A. Golovchenko, J. R. Patel, D. R. Kaplan, P. L. Cowan, and M. J. Bedzyk, Solution to the Surface Registration Problem Using X-Ray Standing Waves, *Physical Review Letters* **49**, 560 (1982).
- [125] B. W. Batterman, Detection of Foreign Atom Sites by Their X-Ray Fluorescence Scattering, *Physical Review Letters* **22**, 703 (1969).
- [126] S. K. Andersen, J. A. Golovchenko, and G. Mair, New Applications of X-Ray Standing-Wave Fields to Solid State Physics, *Physical Review Letters* **37**, 1141 (1976).
- [127] G. Materlik, A. Frahm, and M. J. Bedzyk, X-Ray Interferometric Solution of the Surface Registration Problem, *Physical Review Letters* **52**, 441 (1984).
- [128] I. Vartanyants, T.-L. Lee, S. Thiess, and J. Zegenhagen, Non-Dipole Effects in X-Ray Standing Wave Photoelectron Spectroscopy Experiments, *Nucl Instrum Meth A* **547**, 196 (2005).
- [129] S. T. Manson, Dependence of the Phase Shift on Energy and Atomic Number for Electron Scattering by Atomic Fields, *Physical Review* **182**, 97 (1969).
- [130] U. Fano, C. E. Theodosiou, and J. L. Dehmer, Electron-Optical Properties of Atomic Fields, *Reviews of Modern Physics* **48**, 49 (1976).
- [131] J. Zegenhagen, B. Detlefs, T.-L. Lee, S. Thiess, H. Isern, L. Petit, L. André, J. Roy, Y. Mi, and I. Joumard, X-Ray Standing Waves and Hard X-Ray Photoelectron Spectroscopy at the Insertion Device Beamline Id32, *Journal of Electron Spectroscopy and Related Phenomena* **178-179**, 258 (2010).
- [132] T. L. Lee, C. Kumpf, A. Kazimirov, P. F. Lyman, G. Scherb, M. J. Bedzyk, M. Nielsen, R. Feidenhans'l, R. L. Johnson, B. O. Fimland, and J. Zegenhagen, Structural Analysis of the Indium-Stabilized GaAs(001)-C(8x2) Surface, *Physical Review B* **66** (2002).
- [133] L. Cheng, P. Fenter, M. J. Bedzyk, and N. C. Sturchio, Fourier-Expansion Solution of Atom Distributions in a Crystal Using X-Ray Standing Waves, *Phys Rev Lett* **90**, 255503, 255503 (2003).
- [134] J. Hass, R. Feng, J. E. Millán-Otoya, X. Li, M. Sprinkle, P. N. First, W. A. de Heer, E. H. Conrad, and C. Berger, Structural Properties of the Multilayer Graphene/4h-SiC(0001) System as Determined by Surface X-Ray Diffraction, *Physical Review B* **75**, 8, 214109 (2007).
- [135] Y. Chen, M. W. Gramlich, S. T. Hayden, and P. F. Miceli, Poisson-Like Height Distribution of Ag Nanoislands on Si(111)7x7, *Physical Review B* **95**, 8, 035419 (2017).
- [136] I. K. Robinson, Crystal Truncation Rods and Surface Roughness, *Phys Rev B Condens Matter* **33**, 3830 (1986).
- [137] P. Fenter, J. G. Catalano, C. Park, and Z. Zhang, On the Use of Ccd Area Detectors for High-Resolution Specular X-Ray Reflectivity, *J Synchrotron Radiat* **13**, 293 (2006).
- [138] P. A. Fenter, X-Ray Reflectivity as a Probe of Mineral-Fluid Interfaces: A User Guide, *Reviews in Mineralogy and Geochemistry* **49**, 149 (2002).

- [139] J. R. Fienup, Reconstruction of an Object from the Modulus of Its Fourier Transform, *Opt Lett* **3**, 27 (1978).
- [140] C. D. Wagner, L. H. Gale, and R. H. Raymond, Two-Dimensional Chemical State Plots: A Standardized Data Set for Use in Identifying Chemical States by X-Ray Photoelectron Spectroscopy, *Anal. Chem.* **51**, 466 (2002).
- [141] E. A. Kraut, R. W. Grant, J. R. Waldrop, and S. P. Kowalczyk, Precise Determination of the Valence-Band Edge in X-Ray Photoemission Spectra: Application to Measurement of Semiconductor Interface Potentials, *Physical Review Letters* **44**, 1620 (1980).
- [142] O. Ambacher, J. Smart, J. R. Shealy, N. G. Weimann, K. Chu, M. Murphy, W. J. Schaff, L. F. Eastman, R. Dimitrov, L. Wittmer, M. Stutzmann, W. Rieger, and J. Hilsenbeck, Two-Dimensional Electron Gases Induced by Spontaneous and Piezoelectric Polarization Charges in N- and Ga-Face Algan/Gan Heterostructures, *Journal of Applied Physics* **85**, 3222 (1999).
- [143] M. O. Krause and J. H. Oliver, Natural Widths of Atomic K and L Levels, $K\alpha$ X-Ray Lines and Several KII Auger Lines, *Journal of Physical and Chemical Reference Data* **8**, 329 (1979).
- [144] S. Doniach and M. Sunjic, Many-Electron Singularity in X-Ray Photoemission and X-Ray Line Spectra from Metals, *J Phys Part C Solid* **3**, 285 (1970).
- [145] J. H. Scofield, Exchange Corrections Ofkx-Ray Emission Rates, *Phys. Rev. A* **9**, 1041 (1974).
- [146] P. J. Cumpson and M. P. Seah, Elastic Scattering Corrections in Aes and Xps .2. Estimating Attenuation Lengths and Conditions Required for Their Valid Use in Overlayer/Substrate Experiments, *Surface and Interface Analysis* **25**, 430 (1997).
- [147] A. Jablonski and C. J. Powell, The Electron Attenuation Length Revisited, *Surface Science Reports* **47**, 35, Pii s0167-5729(02)00031-6 (2002).
- [148] C. J. Powell, W. S. M. Werner, W. Smekal, and G. Tasneem, Effective Attenuation Lengths for Photoelectrons in Thin Films of Silicon Oxynitride and Hafnium Oxynitride on Silicon, *Surface and Interface Analysis* **45**, 628 (2013).
- [149] S. Tanuma, C. J. Powell, and D. R. Penn, Calculations of Electron Inelastic Mean Free Paths. V. Data for 14 Organic Compounds over the 50-2000 Ev Range, *Surface and Interface Analysis* **21**, 165 (1994).
- [150] S. Tanuma, C. J. Powell, and D. R. Penn, Proposed Formula for Electron Inelastic Mean Free Paths Based on Calculations for 31 Materials, *Surface Science Letters* **192**, L849 (1987).
- [151] W. H. Gries, A Universal Predictive Equation for the Inelastic Mean Free Pathlengths of X-Ray Photoelectrons and Auger Electrons, *Surface and Interface Analysis* **24**, 38 (1996).
- [152] C. J. Powell, A. Jablonski, and F. Salvat, Nist Databases with Electron Elastic-Scattering Cross Sections, Inelastic Mean Free Paths, and Effective Attenuation Lengths, *Surface and Interface Analysis* **37**, 1068 (2005).
- [153] S. Tanuma, C. J. Powell, and D. R. Penn, Calculations of Electron Inelastic Mean Free Paths. Ix. Data for 41 Elemental Solids over the 50 Ev to 30 Kev Range, *Surface and Interface Analysis* **43**, 689 (2011).
- [154] A. Jablonski, F. Salvat, and C. J. Powell, Comparison of Electron Elastic-Scattering Cross Sections Calculated from Two Commonly Used Atomic Potentials, *Journal of Physical and Chemical Reference Data* **33**, 409 (2004).

- [155] A. Jablonski and C. J. Powell, Practical Expressions for the Mean Escape Depth, the Information Depth, and the Effective Attenuation Length in Auger-Electron Spectroscopy and X-Ray Photoelectron Spectroscopy, *Journal of Vacuum Science & Technology A: Vacuum, Surfaces, and Films* **27**, 253 (2009).
- [156] J. H. Hubbell, P. N. Trehan, N. Singh, B. Chand, D. Mehta, M. L. Garg, R. R. Garg, S. Singh, and S. Puri, A Review, Bibliography, and Tabulation of K, L, and Higher Atomic Shell X-Ray Fluorescence Yields, *Journal of Physical and Chemical Reference Data* **23**, 339 (1994).
- [157] E. Zanazzi and F. Jona, A Reliability Factor for Surface Structure Determinations by Low-Energy Electron Diffraction, *Surface Science* **62**, 61 (1977).
- [158] T. Ogitsu, E. Schwegler, and G. Galli, Beta-Rhombohedral Boron: At the Crossroads of the Chemistry of Boron and the Physics of Frustration, *Chem Rev* **113**, 3425 (2013).
- [159] A. P. Sergeeva, I. A. Popov, Z. A. Piazza, W. L. Li, C. Romanescu, L. S. Wang, and A. I. Boldyrev, Understanding Boron through Size-Selected Clusters: Structure, Chemical Bonding, and Fluxionality, *Acc Chem Res* **47**, 1349 (2014).
- [160] K. S. Novoselov, D. Jiang, F. Schedin, T. J. Booth, V. V. Khotkevich, S. V. Morozov, and A. K. Geim, Two-Dimensional Atomic Crystals, *Proc Natl Acad Sci U S A* **102**, 10451 (2005).
- [161] Q. H. Wang, K. Kalantar-Zadeh, A. Kis, J. N. Coleman, and M. S. Strano, Electronics and Optoelectronics of Two-Dimensional Transition Metal Dichalcogenides, *Nat Nanotechnol* **7**, 699 (2012).
- [162] X. Ling, H. Wang, S. Huang, F. Xia, and M. S. Dresselhaus, The Renaissance of Black Phosphorus, *Proc Natl Acad Sci U S A* **112**, 4523 (2015).
- [163] Z. A. Piazza, H. S. Hu, W. L. Li, Y. F. Zhao, J. Li, and L. S. Wang, Planar Hexagonal B(36) as a Potential Basis for Extended Single-Atom Layer Boron Sheets, *Nat Commun* **5**, 3113, 3113 (2014).
- [164] I. Boustani, Systematic Ab Initio Investigation of Bare Boron Clusters: Determination of the Geometry and Electronic Structures of B_n ($N=2-14$), *Physical Review B* **55**, 16426 (1997).
- [165] X. Wu, J. Dai, Y. Zhao, Z. Zhuo, J. Yang, and X. C. Zeng, Two-Dimensional Boron Monolayer Sheets, *ACS Nano* **6**, 7443 (2012).
- [166] F. Bianchini, L. L. Patera, M. Peressi, C. Africh, and G. Comelli, Atomic Scale Identification of Coexisting Graphene Structures on Ni(111), *J Phys Chem Lett* **5**, 467 (2014).
- [167] J. Zegenhagen, Surface Structure Determination with X-Ray Standing Waves, *Surface Science Reports* **18**, 202 (1993).
- [168] A. J. Mannix, B. Kiraly, M. C. Hersam, and N. P. Guisinger, Synthesis and Chemistry of Elemental 2d Materials, *Nat Rev Chem* **1**, 1 (2017).
- [169] I09 Beamline Layout, <http://www.diamond.ac.uk/Beamlines/Surfaces-and-Interfaces/I09/Beamline-layout.html> (2018).
- [170] B. Feng, O. Sugino, R. Y. Liu, J. Zhang, R. Yukawa, M. Kawamura, T. Iimori, H. Kim, Y. Hasegawa, H. Li, L. Chen, K. Wu, H. Kumigashira, F. Komori, T. C. Chiang, S. Meng, and I. Matsuda, Dirac Fermions in Borophene, *Phys Rev Lett* **118**, 096401 (2017).
- [171] N. A. Fairley, Casaxps, Casa Software Limited, 2016.
- [172] C. J. Powell and A. Jablonski, Electron Effective Attenuation Lengths for Applications in Auger Electron Spectroscopy and X-Ray Photoelectron Spectroscopy, *Surface and Interface Analysis* **33**, 211 (2002).

- [173] T. Susi, M. Kaukonen, P. Havu, M. P. Ljungberg, P. Ayala, and E. I. Kauppinen, Core Level Binding Energies of Functionalized and Defective Graphene, *Beilstein J. Nanotechnol.* **5**, 121 (2014).
- [174] J. F. Moulder and J. Chastain, *Handbook of X-Ray Photoelectron Spectroscopy : A Reference Book of Standard Spectra for Identification and Interpretation of Xps Data* (Physical Electronics Division Perkin-Elmer Corp., Eden Prairie, Minn., 1992).
- [175] E. W. Plummer and W. Eberhardt, Angle-Resolved Photoemission as a Tool for the Study of Surfaces, *Adv. Chem. Phys.* **49**, 533 (1982).
- [176] J. N. Andersen, D. Hennig, E. Lundgren, M. Methfessel, R. Nyholm, and M. Scheffler, Surface Core-Level Shifts of Some 4d-Metal Single-Crystal Surfaces: Experiments and Ab Initio Calculations, *Physical Review B* **50**, 17525 (1994).
- [177] L. E. Berman and M. J. Bedzyk, Angular Distribution of the Photoelectron Yield Excited by Two Coherently Coupled Photon Beams, *Phys Rev Lett* **63**, 1172 (1989).
- [178] M. J. Bedzyk, Q. Shen, M. E. Keeffe, G. Navrotsky, and L. E. Berman, X-Ray Standing Wave Study of Iodine on Ge(111), *Surface Science* **220**, 419 (1989).
- [179] C. B. Duke, Semiconductor Surface Reconstruction: The Structural Chemistry of Two-Dimensional Surface Compounds, *Chem Rev* **96**, 1237 (1996).
- [180] Y. Yamamoto, Atomic Arrangements of 16x2 and (17,15,1)-2x1 Structures on a Si(110) Surface, *Phys Rev B* **50**, 8534 (1994).
- [181] G. Binnig, H. Rohrer, C. Gerber, and E. Weibel, 7x7 Reconstruction on Si(111) Resolved in Real Space, *Phys Rev Lett* **50**, 120 (1983).
- [182] T. An, M. Yoshimura, I. Ono, and K. Ueda, Elemental Structure in Si(110)-"16x2" Revealed by Scanning Tunneling Microscopy, *Phys Rev B* **61**, 3006 (2000).
- [183] T. Ichikawa, An Ab Initio Study on the Atomic Geometry of Reconstructed Ge(110)16x2 Surface, *Surface Science* **544**, 58 (2003).
- [184] A. A. Stekolnikov, J. Furthmüller, and F. Bechstedt, Structural Elements on Reconstructed Si(110) Surfaces, *Physical Review B* **70** (2004).
- [185] N. Hisato and I. Toshihiro, Rheed Study of Surface Reconstruction at Clean Ge(110) Surface, *Japanese Journal of Applied Physics* **24**, 1288 (1985).
- [186] N. D. Kim, Y. K. Kim, C. Y. Park, H. W. Yeom, H. Koh, E. Rotenberg, and J. R. Ahn, High-Resolution Photoemission Spectroscopy Study of the Single-Domain Si(110)-16x2 Surface, *Phys Rev B* **75**, 5, 125309 (2007).
- [187] K. Sakamoto, M. Setvin, K. Mawatari, P. E. J. Eriksson, K. Miki, and R. I. G. Uhrberg, Electronic Structure of the Si(110)-(16x2) Surface: High-Resolution Arpes and Stm Investigation, *Phys Rev B* **79**, 6, 045304 (2009).
- [188] M. C. Hersam, N. P. Guisinger, J. Lee, K. Cheng, and J. W. Lyding, Variable Temperature Study of the Passivation of Dangling Bonds at Si(100)-2x1 Reconstructed Surfaces with H and D, *Applied Physics Letters* **80**, 201 (2002).
- [189] J. M. Buriak, Organometallic Chemistry on Silicon and Germanium Surfaces, *Chem Rev* **102**, 1271 (2002).
- [190] G. S. Higashi, Y. J. Chabal, G. W. Trucks, and K. Raghavachari, Ideal Hydrogen Termination of the Si-(111) Surface, *Appl Phys Lett* **56**, 656 (1990).

- [191] C. Riedl, C. Coletti, T. Iwasaki, A. A. Zakharov, and U. Starke, Quasi-Free-Standing Epitaxial Graphene on Sic Obtained by Hydrogen Intercalation, *Phys Rev Lett* **103**, 246804, 246804 (2009).
- [192] K. V. Emtsev, A. A. Zakharov, C. Coletti, S. Forti, and U. Starke, Ambipolar Doping in Quasifree Epitaxial Graphene on Sic(0001) Controlled by Ge Intercalation, *Phys Rev B* **84** (2011).
- [193] G. Wang, M. Zhang, Y. Zhu, G. Ding, D. Jiang, Q. Guo, S. Liu, X. Xie, P. K. Chu, Z. Di, and X. Wang, Direct Growth of Graphene Film on Germanium Substrate, *Sci Rep* **3**, 2465 (2013).
- [194] J. Tesch, E. Voloshina, M. Fonin, and Y. Dedkov, Growth and Electronic Structure of Graphene on Semiconducting Ge(110), *Carbon* **122**, 428 (2017).
- [195] T. Ichikawa, In Situ Stm Observations of Ordering Behaviors on Ge(110) Surfaces and Atomic Geometry of the Ge{17151} Facet, *Surf Sci* **560**, 213 (2004).
- [196] C. H. Mullet and S. Chiang, Reconstructions and Phase Transition of Clean Ge(110), *Surface Science* **621**, 184 (2014).
- [197] N. Takeuchi, Bond Conserving Rotation, Adatoms and Rest Atoms in the Reconstruction of Si(110) and Ge(110) Surfaces: A First Principles Study, *Surf Sci* **494**, 21 (2001).
- [198] P. Bampoulis, A. Acun, L. J. Zhang, and H. J. W. Zandvliet, Electronic and Energetic Properties of Ge(110) Pentagons, *Surf Sci* **626**, 1 (2014).
- [199] R. Feidenhans'l, Surface Structure Determination by X-Ray Diffraction, *Surface Science Reports* **10** (1989).
- [200] R. S. Becker, J. A. Golovchenko, and J. R. Patel, X-Ray Evanescent-Wave Absorption and Emission, *Physical Review Letters* **50**, 153 (1983).
- [201] P. M. T. M. van Attekum and G. K. Wertheim, Excitonic Effects in Core-Hole Screening, *Physical Review Letters* **43**, 1896 (1979).
- [202] T. T. P. Cheung, X-Ray Photoemission of Carbon: Lineshape Analysis and Application to Studies of Coals, *Journal of Applied Physics* **53**, 6857 (1982).
- [203] I. K. Robinson and D. J. Tweet, *Surface X-Ray Diffraction*, *Rep. Prog. Phys.* **55** (1992).
- [204] A. Kraft, R. Temirov, S. K. M. Henze, S. Soubatch, M. Rohlfing, and F. S. Tautz, Lateral Adsorption Geometry and Site-Specific Electronic Structure of a Large Organic Chemisorbate on a Metal Surface, *Physical Review B* **74**, 4, 041402 (2006).
- [205] J. Bohr, R. Feidenhans'l, M. Nielsen, M. Toney, R. L. Johnson, and I. K. Robinson, Model-Independent Structure Determination of the Insb(111)2 X 2 Surface with Use of Synchrotron X-Ray Diffraction, *Phys Rev Lett* **54**, 1275 (1985).
- [206] A. L. Patterson, A Direct Method for the Determination of the Components of Interatomic Distances in Crystals, *Z. Kristall.* **90**, 517 (1935).
- [207] T. An, M. Yoshimura, I. Ono, and K. Ueda, Elemental Structure in Si(110)-"16x2" Revealed by Scanning Tunneling Microscopy, *Physical Review B* **61**, 3006 (2000).
- [208] N. Takeuchi, Bond Conserving Rotation, Adatoms and Rest Atoms in the Reconstruction of Si() and Ge() Surfaces: A First Principles Study, *Surface Science* **494**, 21 (2001).
- [209] P. Bampoulis, A. Acun, L. Zhang, and H. J. W. Zandvliet, Electronic and Energetic Properties of Ge(110) Pentagons, *Surface Science* **626**, 1 (2014).

- [210] L. Yu, Y. H. Lee, X. Ling, E. J. Santos, Y. C. Shin, Y. Lin, M. Dubey, E. Kaxiras, J. Kong, H. Wang, and T. Palacios, Graphene/Mos2 Hybrid Technology for Large-Scale Two-Dimensional Electronics, *Nano Lett* **14**, 3055 (2014).
- [211] K. Roy, M. Padmanabhan, S. Goswami, T. P. Sai, G. Ramalingam, S. Raghavan, and A. Ghosh, Graphene-Mos2 Hybrid Structures for Multifunctional Photoresponsive Memory Devices, *Nat Nanotechnol* **8**, 826 (2013).
- [212] C. Çelebi, C. Yanık, A. G. Demirkol, and İ. İ. Kaya, The Effect of a Sic Cap on the Growth of Epitaxial Graphene on Sic in Ultra High Vacuum, *Carbon* **50**, 3026 (2012).
- [213] W. Norimatsu and M. Kusunoki, Transitional Structures of the Interface between Graphene and 6h-Sic (0001), *Chemical Physics Letters* **468**, 52 (2009).
- [214] J. D. Emery, V. D. Wheeler, J. E. Johns, M. E. McBriarty, B. Detlefs, M. C. Hersam, D. Kurt Gaskill, and M. J. Bedzyk, Structural Consequences of Hydrogen Intercalation of Epitaxial Graphene on Sic(0001), *Applied Physics Letters* **105**, 161602 (2014).
- [215] C. Xia, S. Watcharinyanon, A. A. Zakharov, R. Yakimova, L. Hultman, L. I. Johansson, and C. Virojanadara, Si Intercalation/Deintercalation of Graphene on 6h-Sic(0001), *Physical Review B* **85** (2012).
- [216] K. V. Emtsev, A. A. Zakharov, C. Coletti, S. Forti, and U. Starke, Ambipolar Doping in Quasifree Epitaxial Graphene on Sic(0001) Controlled by Ge Intercalation, *Physical Review B* **84**, 6, 125423 (2011).
- [217] J. Sforzini, P. Hapala, M. Franke, G. van Straaten, A. Stohr, S. Link, S. Soubatch, P. Jelinek, T. L. Lee, U. Starke, M. Svec, F. C. Bocquet, and F. S. Tautz, Structural and Electronic Properties of Nitrogen-Doped Graphene, *Phys Rev Lett* **116**, 126805, 126805 (2016).
- [218] A. Krishnan, E. Dujardin, M. M. J. Treacy, J. Hugdahl, S. Lynum, and T. W. Ebbesen, Graphitic Cones and the Nucleation of Curved Carbon Surfaces, *Nature* **388**, 451 (1997).
- [219] D. Jariwala, T. J. Marks, and M. C. Hersam, Mixed-Dimensional Van Der Waals Heterostructures, *Nat Mater* **16**, 170 (2017).
- [220] J. W. Jiang, X. Zhuang, and T. Rabczuk, Orientation Dependent Thermal Conductance in Single-Layer Mos2, *Sci Rep* **3**, 2209, 2209 (2013).
- [221] A. J. Van Bommel, J. E. Crombeen, and A. Van Tooren, Leed and Auger Electron Observations of the Sic(0001) Surface, *Surface Science* **48**, 463 (1975).
- [222] Q. Ji, M. Kan, Y. Zhang, Y. Guo, D. Ma, J. Shi, Q. Sun, Q. Chen, Y. Zhang, and Z. Liu, Unravelling Orientation Distribution and Merging Behavior of Monolayer Mos2 Domains on Sapphire, *Nano Lett* **15**, 198 (2015).
- [223] M. I. Utama, Q. Zhang, J. Zhang, Y. Yuan, F. J. Belarre, J. Arbiol, and Q. Xiong, Recent Developments and Future Directions in the Growth of Nanostructures by Van Der Waals Epitaxy, *Nanoscale* **5**, 3570 (2013).
- [224] D. Dumcenco, D. Ovchinnikov, K. Marinov, P. Lazic, M. Gibertini, N. Marzari, O. Lopez Sanchez, Y. C. Kung, D. Krasnozhan, M. W. Chen, S. Bertolazzi, P. Gillet, A. Fontcuberta i Morral, A. Radenovic, and A. Kis, Large-Area Epitaxial Monolayer Mos2, *ACS Nano* **9**, 4611 (2015).
- [225] Y. C. Lin, N. Lu, N. Perea-Lopez, J. Li, Z. Lin, X. Peng, C. H. Lee, C. Sun, L. Calderin, P. N. Browning, M. S. Bresnehan, M. J. Kim, T. S. Mayer, M. Terrones, and J. A. Robinson, Direct Synthesis of Van Der Waals Solids, *ACS Nano* **8**, 3715 (2014).

- [226] J. M. Alaboson, C. H. Sham, S. Kewalramani, J. D. Emery, J. E. Johns, A. Deshpande, T. Chien, M. J. Bedzyk, J. W. Elam, M. J. Pellin, and M. C. Hersam, Templating Sub-10 Nm Atomic Layer Deposited Oxide Nanostructures on Graphene Via One-Dimensional Organic Self-Assembled Monolayers, *Nano Lett* **13**, 5763 (2013).
- [227] J. Hass, F. Varchon, J. E. Millan-Otoya, M. Sprinkle, N. Sharma, W. A. de Heer, C. Berger, P. N. First, L. Magaud, and E. H. Conrad, Why Multilayer Graphene on 4h-Sic(0001) Behaves Like a Single Sheet of Graphene, *Phys Rev Lett* **100**, 125504 (2008).
- [228] H. Liu, A. T. Neal, Z. Zhu, Z. Luo, X. Xu, D. Tomanek, and P. D. Ye, Phosphorene: An Unexplored 2d Semiconductor with a High Hole Mobility, *ACS Nano* **8**, 4033 (2014).

Appendix A: XPS-XSW at Diamond I09

A.1: Data collection and Analysis

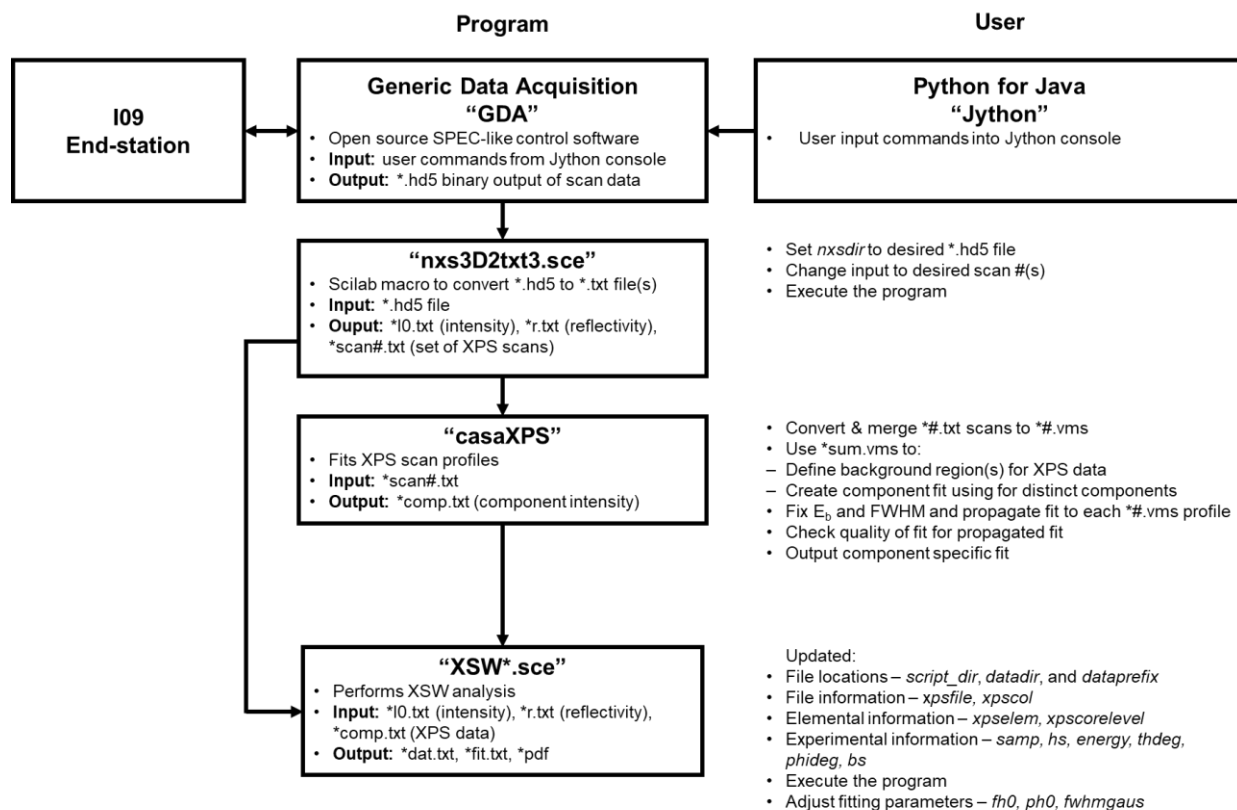


Figure A.1: Flowchart describing the procedure to collect and analyze data at I09.

A.2: Performance Issues in Photoelectron Yields

Describe the particularities of the Scienta XPS hardware used. Namely Model No. , CCD detector type, cone angle acceptance, mode of collection, etc.

XSW excited XPS data showed definite differences with photoemission angle that were not accounted for using the quadrupole approximation for the photoelectron yield. Table A.1 shows the angularly resolved Ag 3d_{5/2} scans, which reveals the fitted coherent fraction values are

correlated well to total the total integrated intensities of the XSW excited XPS scans at each takeoff angle. The coherent fractions achieve unphysically high ($f_{300^\circ\text{C}} > 1.0$) coherent fractions for most takeoff angles ($8.5^\circ - 27.8^\circ$) accompanied by a reduction in quality of the XSW yield fits (Figure A.2). For low takeoff angle (5.3°), coherent fraction was physical ($f_{300^\circ\text{C}} < 1.0$) and the fitted yield matched the experimental data, while the higher takeoff angle scans (8.5° and 15°) show a reduction in fit quality, most evident near the most intense (red arrows) and least intense (green arrow) intensities. This reduced quality can be attributed to an increase in the integrated Ag $3d_{5/2}$ scans in the region identified by the red arrow, which achieves a Y_{max} of 2.2, 2.8, and 3.1, for the 5.3° , 8.5° and 15° scans, respectively. Therefore, the unphysically high ($f_{300^\circ\text{C}} > 1.0$) coherent fractions measured are the result of XPS signal enhancement of high XPS counts/s scans. This effect is most pronounced for the Ag $3d_{5/2}$ scans and not observed for B 1s (020) and (022) off-specular scans, where the B 1s count/s are significantly reduced.

Additionally, notable shifts in the measured XPS kinetic energy and FWHM of all XPS peaks occurred while scanning over the Bragg condition (Figure A.3). The binding energy of Ag $3d_{5/2}$ inversely correlates to reflectivity, suggesting. No correlation with takeoff angular can be established (Figure A.3), therefore this phenomenon is independent of the effects observed in Figure A.2. Ultimately, these values could not be held fixed as is customary in XSW fitting procedures. The kinetic energies of the peaks were held at constant relative position and the FWHM were held at a constant multiplicative factor, leaving a single kinetic energy and FWHM to vary during peak fitting procedure.

Table A.1: Coherent fractions ($f_{300^\circ\text{C}}$), maximum normalized yields (Y_{max}), and corresponding maximum intensity (I_{max}) of Ag $3d_{5/2}$ photoelectron yields from the 300°C sample. θ is the angle between the ejected photoelectron and the sample surface plane.

θ ($^\circ$)	5.3	8.5	11.8	15.0	18.2	21.4	24.7	27.8
-----------------------	-----	-----	------	------	------	------	------	------

$f_{300^\circ\text{C}}$	0.86	1.06	1.17	1.24	1.23	1.20	1.09	1.06
Y_{max}	2.2	2.8	2.9	3.1	3.0	3.0	2.7	2.7
I_{max} (a.u.)	0.0013	0.028	0.13	0.36	0.44	0.66	1	0.83

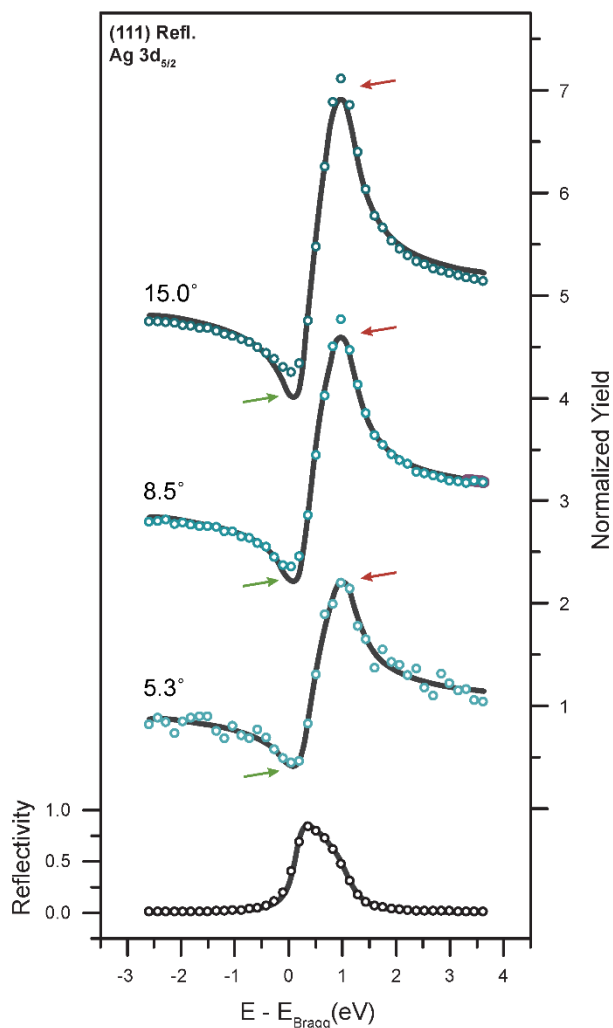


Figure A.2: X-ray standing wave (XSW) characterization of silver at the borophene/Ag(111) interface. Data (circles) and eq. 5.1 model fits (black lines) for incident X-ray energy dependence of the X-ray reflectivity and normalized Ag $3d_{5/2}$ photoelectron yields of 300 °C sample probed at $\alpha = 5.3^\circ, 8.5^\circ, 15.0^\circ$. XSW results show gradual increase in coherent fraction f_θ , yielding near-unity coherent fractions $f_{5.3^\circ} = 0.86(3)$, $f_{8.5^\circ} = 1.05(3)$, and $f_{15.0^\circ} = 1.17(3)$. θ is the angle between the ejected photoelectron and the sample surface plane.

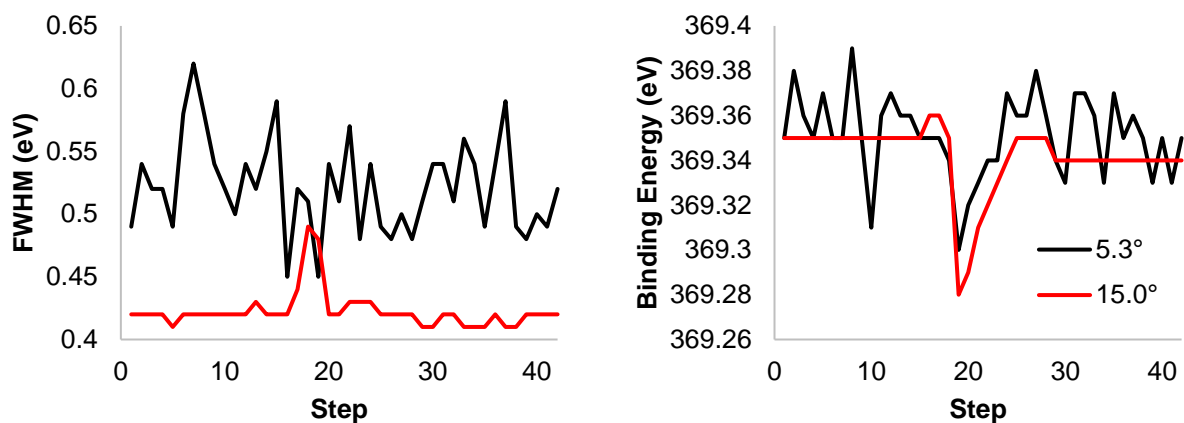


Figure A.3: X-ray photoelectron spectroscopy fitting parameters of Ag 3d spectra during X-ray standing wave characterization of the 300 °C sample probed at $\alpha = 5.3^\circ$ and 15.0° .

Appendix B: Data sets

B.1: GIXD Data for “6×2” EG/Ge(110)

Table B.1: Measured $|F_{h_s k_s}|^2$ for Ge(110) “6×2” reconstruction.

h_s	k_s	$ F_{h_s k_s} ^2$	Error								
0	1	2.23E+03	2.E+02	-2	7	1.55E+03	2.E+02	-4	-7	0.00E+00	3.E+02
0	2	1.79E+03	1.E+02	-2	0	1.66E+03	2.E+02	-5	0	0.00E+00	2.E+02
0	3	0.00E+00	4.E+01	-2	-1	5.08E+03	4.E+02	-5	1	2.30E+02	4.E+01
0	4	0.00E+00	9.E+02	-2	-2	4.63E+03	6.E+02	-5	2	6.19E+02	5.E+01
0	5	2.92E+02	5.E+01	-2	-3	0.00E+00	6.E+02	-5	3	0.00E+00	1.E+02
0	6	3.49E+02	1.E+02	-2	-4	3.91E+03	3.E+02	-5	4	3.49E+02	1.E+02
0	7	2.52E+04	2.E+03	-2	-5	0.00E+00	9.E+01	-5	5	1.22E+03	1.E+02
0	-1	0.00E+00	2.E+02	-2	-6	0.00E+00	1.E+02	-5	6	0.00E+00	6.E+02
0	-2	1.13E+03	9.E+01	-2	-7	1.66E+03	1.E+02	-5	7	0.00E+00	3.E+03
0	-3	0.00E+00	9.E+01	-3	0	4.63E+03	6.E+02	-5	0	0.00E+00	2.E+02
0	-4	0.00E+00	9.E+02	-3	1	2.37E+03	2.E+02	-5	-1	3.66E+03	3.E+02
0	-5	2.38E+02	4.E+01	-3	2	1.55E+03	1.E+02	-5	-3	4.58E+02	4.E+01
0	-6	3.49E+02	1.E+02	-3	3	8.13E+02	7.E+01	-5	-4	3.98E+03	3.E+02
0	-7	2.28E+04	2.E+03	-3	4	5.53E+02	8.E+01	-5	-5	9.75E+02	8.E+01
-1	0	2.16E+03	2.E+02	-3	5	0.00E+00	4.E+01	-5	-6	8.15E+02	8.E+01
-1	1	1.71E+03	1.E+02	-3	7	0.00E+00	3.E+03	-5	-7	0.00E+00	2.E+02
-1	3	1.68E+03	1.E+02	-3	0	4.63E+03	6.E+02	-6	1	1.30E+03	1.E+02
-1	4	3.97E+03	3.E+02	-3	-1	3.85E+02	3.E+01	-6	2	0.00E+00	2.E+02
-1	5	0.00E+00	2.E+02	-3	-2	1.12E+03	9.E+01	-6	3	0.00E+00	1.E+02
-1	6	9.93E+02	1.E+02	-3	-3	6.61E+02	5.E+01	-6	4	1.08E+04	9.E+02
-1	7	2.01E+03	2.E+02	-3	-4	1.29E+03	1.E+02	-6	5	0.00E+00	3.E+02
-1	0	2.16E+03	2.E+02	-3	-5	2.86E+03	2.E+02	-6	6	0.00E+00	2.E+02
-1	-1	0.00E+00	7.E+01	-3	-7	0.00E+00	2.E+02	-6	7	0.00E+00	4.E+03
-1	-2	2.71E+03	2.E+02	-4	0	1.67E+02	3.E+01	-6	-1	4.70E+03	4.E+02
-1	-3	9.26E+02	7.E+01	-4	1	1.12E+03	9.E+01	-6	-2	3.50E+02	5.E+01
-1	-4	0.00E+00	4.E+02	-4	2	0.00E+00	4.E+02	-6	-3	0.00E+00	7.E+01
-1	-5	0.00E+00	2.E+02	-4	3	4.71E+02	7.E+01	-6	-4	3.18E+03	3.E+02
-1	-6	4.71E+02	7.E+01	-4	4	0.00E+00	7.E+01	-6	-5	4.37E+02	6.E+01
-1	-7	2.13E+03	2.E+02	-4	5	0.00E+00	8.E+01	-6	-6	4.20E+02	1.E+02
-2	0	1.66E+03	2.E+02	-4	6	0.00E+00	4.E+02	-6	-7	3.37E+03	3.E+02
-2	1	1.61E+03	1.E+02	-4	7	0.00E+00	9.E+02	-7	0	2.07E+03	2.E+02
-2	2	1.49E+03	1.E+02	-4	0	1.67E+02	3.E+01	-7	1	0.00E+00	2.E+02
-2	3	3.48E+02	5.E+01	-4	-1	7.91E+02	6.E+01	-7	3	3.84E+03	3.E+02
-2	5	1.37E+04	1.E+03	-4	-2	0.00E+00	6.E+01	-7	4	0.00E+00	4.E+02
-2	6	2.32E+03	2.E+02	-4	-3	1.69E+03	1.E+02	-7	5	0.00E+00	7.E+01
				-4	-5	1.41E+03	1.E+02	-7	6	0.00E+00	5.E+02
				-4	-6	5.37E+02	8.E+01	-7	0	2.07E+03	2.E+02

-7	-1	8.33E+03	7.E+02	-8	-5	0.00E+00	6.E+01	-10	2	0.00E+00	4.E+02
-7	-2	0.00E+00	1.E+02	-8	-6	0.00E+00	2.E+03	-10	3	0.00E+00	2.E+02
-7	-3	0.00E+00	2.E+02	-8	-7	0.00E+00	2.E+02	-10	4	0.00E+00	3.E+02
-7	-4	1.04E+04	1.E+03	-9	0	4.20E+02	1.E+02	-10	-1	3.08E+03	2.E+02
-7	-5	4.75E+02	5.E+01	-9	1	2.31E+03	2.E+02	-10	-2	5.48E+02	8.E+01
-7	-6	0.00E+00	2.E+02	-9	2	0.00E+00	4.E+02	-10	-3	0.00E+00	6.E+02
-7	-7	0.00E+00	3.E+02	-9	3	0.00E+00	1.E+03	-10	-5	7.21E+02	8.E+01
-8	0	1.81E+03	2.E+02	-9	4	0.00E+00	2.E+02	-10	-6	0.00E+00	1.E+03
-8	1	0.00E+00	8.E+01	-9	5	0.00E+00	6.E+01	-10	-7	0.00E+00	1.E+02
-8	2	0.00E+00	1.E+02	-9	0	4.20E+02	1.E+02	-11	1	0.00E+00	7.E+01
-8	3	1.90E+03	2.E+02	-9	-1	5.32E+02	6.E+01	-11	2	0.00E+00	7.E+02
-8	5	0.00E+00	1.E+02	-9	-2	3.88E+02	6.E+01	-11	3	0.00E+00	5.E+02
-8	0	1.81E+03	2.E+02	-9	-3	3.78E+02	6.E+01	-11	-1	1.32E+04	1.E+03
-8	-1	9.23E+02	7.E+01	-9	-4	0.00E+00	1.E+03	-11	-2	0.00E+00	Inf
-8	-2	1.04E+04	1.E+03	-9	-5	0.00E+00	3.E+01	-11	-3	2.51E+03	2.E+02
-8	-3	0.00E+00	2.E+02	-9	-7	0.00E+00	1.E+02				
-8	-4	0.00E+00	5.E+01	-10	1	2.14E+03	2.E+02				